Continuum Models of Deformation Mechanisms in Nanocrystalline Metals

by

Antoine Jérusalem

Submitted to the Department of Aeronautics and Astronautics
in partial fulfillment of the requirements for the degree of
Doctor of Philosophy in Aeronautics and Astronautics
at the
MASSACHUSETTS INSTITUTE OF TECHNOLOGY
May 2007 [June 2007]

Author .....
Department of Aeronautics and Astronautics
May 25, 2007

Certified by .....
Raúl Radovitzky
Associate Professor of Aeronautics and Astronautics
Thesis Supervisor

Committee Member .....
Jaime Peraire
Professor of Aeronautics and Astronautics

Committee Member .....
Christopher Schuh
Associate Professor of Materials Science and Engineering

Committee Member .....
Subra Suresh
Professor of Materials Science and Engineering

Accepted by .....
Jaime Peraire
Professor of Aeronautics and Astronautics
Chair, Committee on Graduate Students

Continuum Models of Deformation Mechanisms in Nanocrystalline Metals

by

Antoine Jérusalem

Submitted to the Department of Aeronautics and Astronautics
on May 25, 2007, in partial fulfillment of the
requirements for the degree of
Doctor of Philosophy in Aeronautics and Astronautics

Abstract

Nanocrystalline metals are polycrystalline metals with grain sizes in the nanometer range. They have attracted significant interest in recent years due to their unique mechanical and electrical properties. The main objective of this thesis is to develop continuum-scale descriptions of nanoscale deformation and failure mechanisms in nanocrystalline metals. The research has focused on three specific aspects: the influence of grain boundary mechanisms on the grain-size dependence of the yield stress, the influence of grain boundary friction on the response to shock loading and the increased ductility accompanied by increased strength observed in ultrafine crystals with embedded growth nanotwins.

A phenomenological model considering grain boundary sliding and accommodation as uncoupled dissipative deformation mechanisms is proposed to describe the constitutive behavior of grain boundaries. In agreement with atomistic models and experiments, tensile test simulations using the numerical model predict the inverse Hall-Petch effect, *i.e.* a dependence of the yield stress on the inverse square root of the grain size with a negative slope. In addition, the model suggests that the observed discrepancy between atomistic and experimental results may be partially related to rate dependence effects.

Recent atomistic simulation results suggest that high states of compression inhibit grain boundary sliding, which causes a reactivation of intragrain dislocation activity, leading to much higher material strength. We extend the continuum model to account for these frictional effects inhibiting deformation at the grain boundary. The extended model captures the salient features of the shock response of nanocrystalline copper observed in atomistic simulations, including the shock propagation and jump conditions, as well as the peak and trailing values of the deviatoric stress profile.

One of the limitations of nanocrystals is their low ductility. It has been shown recently that the high strength of nanocrystals without a compromise in ductility can be achieved by growing ultrafine crystals with embedded nano-twins. Twin boundaries provide equivalent barriers to dislocation motion as grain boundaries do in nanocrystals, but without their associated low ductility. A model for describing the strength-

ening and toughening role of nanotwins is developed and calibrated to experiments. The model captures the dependence of the stress-strain response on twin density including the onset of fracture observed in experiments.

Part of the legacy of this thesis work is a computational framework for large-scale simulation of the continuum-level response of nanocrystalline metals. This parallel computing framework was developed in order to address the necessity of describing the full three-dimensional response of large number of grains subject to a wide range of loading conditions.

Thesis Supervisor: Raúl Radovitzky
Associate Professor of Aeronautics and Astronautics

Committee Member: Jaime Peraire
Professor of Aeronautics and Astronautics

Committee Member: Christopher Schuh
Associate Professor of Materials Science and Engineering

Committee Member: Subra Suresh
Professor of Materials Science and Engineering

Acknowledgments

My first thanks naturally go to my advisor and mentor, Prof. Raúl Radovitzky, without whom none of this would have been possible. His dedication to guiding me and advising me throughout my education at MIT constitutes the foundation of this achievement.

I am also thankful for the support of the DoE through the Caltech ASC Center for Simulation of Dynamic Response of Materials under contract 82-1052904.

I would also like to thank my thesis committee: Prof. Jaime Peraire, Prof. Christopher Schuh and Prof. Subra Suresh, as well as Prof. Mark Spearing as a reader, for their their precious help and recommendations.

I would like to thank more than ever my family on the other side of the Atlantic Ocean, my parents and sisters particularly, for always being there when I needed them, despite the distance.

Last but not least, my life would not be the same without all my friends, either back on the old continent or on this side of the Atlantic. I would like to thank all of them for standing by me during all these years and for the new life ahead of me.

Contents

1 Introduction **23**

2 Continuum modeling framework for nanocrystals **35**

2.1 Continuum formulation 37

2.1.1 Governing equations 37

2.1.2 Kinematic assumptions 40

2.1.3 Variational constitutive framework 41

2.2 Finite-element discretization 45

3 Grain size dependence of the yield stress in nanocrystalline metals **49**

3.1 Simulation setup 49

3.2 Model calibration 51

3.3 Grain size dependence 54

3.4 Summary 59

4 Continuum modeling of shock response in nanocrystals **61**

4.1 Grain boundary friction model 63

4.2 Model for the grain bulk response under shock loading 64

4.2.1 Equation of state 64

4.2.2 Intragrain plasticity 66

4.3 Simulation setup 68

4.3.1 Artificial viscosity 69

4.3.2 Calibration of model parameters 70

4.4 Influence of friction on the shock response of nanocrystals 78
4.5 Conclusion 84

5 Continuum model of ultrafine polycrystals with embedded growth nano-twins 85

5.1 Constitutive model for single crystals with embedded twins 90
5.2 Fracture initiation criterion 98
5.3 Numerical simulations 99
5.3.1 Simulation setup 100
5.3.2 Plane strain simulations 101
5.3.3 Full three-dimensional simulations 103
5.4 Discussion 103

6 Conclusion 107

A Entropy considerations in the propagation of shocks in nanocrystals 111

A.1 Constitutive law 111
A.2 Evaluation of the material constants 113
A.3 Evaluation of the internal variables, stress and strain tensors 116
A.4 Evaluation of the entropy terms in the global equation 117

List of Figures

1-1 TEM image of electrodeposited nanocrystalline Ni with an average grain size of $\sim 30nm$ 24

1-2 Chokshi's experimental observation of the reverse Hall-Petch effect on Cu and Pd 25

1-3 Molecular statics simulations by Schiøtz *et al.* (1998) showing the reverse Hall-Petch Effect 27

1-4 Molecular dynamics simulations by Schiøtz *et al.* (2003) showing the crossover from the direct to the reverse Hall-Petch Effect 27

1-5 Snapshot of MD simulation of shock propagation of a $\sim 50GPa$ pressure wave after $30ps$ in Cu nanocrystal with grain size of $20nm$ . . . 28

1-6 TEM image of electrodeposited nanocrystalline Cu with an average twin spacing of $\sim 15nm$ 30

1-7 Comparison of strength and ductility of coarse (grain size $> 100\mu m$), nanocrystalline (grain size $\sim 30nm$) and nano-twinned (twin spacing $\sim 15nm$) grains from the corresponding strain-stress curves 31

2-1 Schematic of geometric model of nanocrystals as a continuum with surfaces of discontinuity at grain boundaries 38

2-2 Schematic of grain boundary element. Two tetrahedra belonging to two adjacent crystals separated by an interface element at the grain boundary: $S+$ and $S-$ are respectively the facets corresponding to the tetrahedra on the positive and negative side as defined by the positive surface normal $\mathbf{N}$ and S is the midsurface 46

3-1 Idealized polycrystal grain configurations used in calculations. Designation and number of grains 50

3-2 Calibration of grain boundary model parameters against atomistic results from for grain size $d \approx 6.6nm$ and strain-rate $5 \times 10^8 s^{-1}$ 53

3-3 Calibration of grain boundary model parameters against experimental results from for grain size $d \approx 25nm$ 54

3-4 Tensile dynamic simulations of a 20nm plate for d=10, 6.67, 5 and 4nm 56

3-5 Tensile static simulations of a 100nm plate for d=33, 25 and 20nm . . 57

3-6 Hall-Petch plot of our two sets of simulations and of the corresponding atomistic and experimental results 58

4-1 Flow stress versus grain size as predicted by Bringa *et al.*'s model with MD results 62

4-2 Strength asymmetry on a cubic $4nm$ grain size specimen in Lund *et al.*'s simulations 63

4-3 6x4x4 mesh used in the shock simulations; the heavy lines denote the grain boundaries between the tetrakaidecahedra 69

4-4 Shock pressure distribution after 10ps of simulation for two different values of $C_0 = 3910m/s$ and $C_0 = 4841m/s$; comparison with atomistic simulation 71

4-5 Comparison of Von Mises stress distribution after $10ps$ between continuum model and atomistic simulations 72

4-6 Shock simulations for longer time (60ps) than MD simulations (10ps) showing decay of Von Mises stress toward uniform value consistent with atomistic description 74

4-7 Mesh convergence study showing shock pressure distribution at 10ps for three different mesh sizes 76

4-8 Mesh convergence study showing Von Mises stress distribution at 10ps for three different mesh sizes 77

4-9 Von Mises stress for a shocked 6x4x4 model of nanocrystalline copper after $10ps$ with $U_p = 1000m/s$; plots of simulations are shown for a longitudinal slice in the middle of the rod with and without grain boundary sliding and with/without friction in the grain boundary (GB) sliding case 79

4-10 Shock pressure distribution after $10ps$; plots of simulations are shown for a longitudinal line in the middle of the rod with and without grain boundary sliding and with/without friction in the GB sliding case . . 80

4-11 Von Mises stress distribution after $10ps$; plots of simulations are shown for a longitudinal line in the middle of the rod with and without grain boundary sliding and with/without friction in the GB sliding case . . 81

4-12 Temperature distribution after $10ps$; plots of simulations are shown for a longitudinal line in the middle of the rod with and without grain boundary sliding and with/without friction in the GB sliding case . . 82

4-13 Velocity distribution after $10ps$; plots of simulations are shown for a longitudinal line in the middle of the rod with and without grain boundary sliding and with/without friction in the GB sliding case . . 83

5-1 Grain boundary and twin boundaries in nano-twinned ultrafine polycrystalline Cu 86

5-2 Absorption, desorption and direct transmission of a dislocation at twin boundaries as described by Zhu *et al.* 88

5-3 Stress-strain curves for different strain rates for ultrafine, coarse nano-twinned, medium nano-twinned and fine nano-twinned polycrystalline Cu from Dao *et al.* 89

5-4 Dao *et al.*'s 2D model of twinned polycrystal; the twinned slip system is considered as the soft shear mode and the two others are labeled as hard shear mode 96

5-5 Fracture criterion for twinned polycrystal; each twin boundary allows a maximum slip of $\delta_{\max}$ of slip, leading to a maximum shear of $\gamma_{\max} = n\delta_{\max}$ where n is the number of twin boundaries per unit length 98

5-6 Simulated stress-strain curves for $d_{\text{twin}} = 100nm$, $35nm$ and $15nm$ and strain rates $6 \times 10^{-3}s^{-1}$, $6 \times 10^{-2}s^{-1}$ and $6 \times 10^{-1}s^{-1}$; the symbol "X" indicates the initiation of failure according to the adopted fracture criterion 99

5-7 Model meshes used for the simulations of nano-twinned ultrafine polycrystals; the dark shadows denote the grain boundaries 100

5-8 Lu *et al.*'s experimental tensile tests for different twin spacings $d_{\text{twin}} = 100nm$, $35nm$ and $15nm$ and the corresponding plane strain simulations. The simulations are stopped when the fracture initiation criterion is met . 102

5-9 Lu *et al.*'s experimental tensile tests for different twin spacings $d_{\text{twin}} = 100nm$, $35nm$ and $15nm$ and the corresponding 3D simulations. The simulations are stopped when the fracture initiation criterion is met 104

List of Tables

3.1 Simulation and Model parameters after calibration for Cu grain boundaries 55

4.1 Model parameters for Cu bulk grain 75

4.2 Model parameters for Cu grain boundaries 75

5.1 Model parameters for Cu 97

Nomenclature

List of symbols	
$a^{\alpha\beta}$	Interaction matrix coefficients
a_i	Interaction coefficients
A	Total grain boundary free energy density
A_b	Opening grain boundary free energy density
A_s	Sliding grain boundary free energy density
$\mathbf{a}_\alpha$	Covariant basis vector in the grain boundary element referential
b	Burgers vector
B_0	Region occupied by the body in the initial configuration
B_0^g	Region occupied by grain g in the initial configuration
$\mathbf{b}$	Body forces
$\bar{\mathcal{B}}_t$	Intermediate configuration
c_1	First artificial viscosity parameter
c_L	Second artificial viscosity parameter
C_p	Specific volume at constant pressure
C_v	Specific volume at constant volume
C_0	Offset of the Hugoniot
C_{11}, C_{12}, C_{44}	Elastic constants
$\mathbf{C}$	Right Cauchy-Green deformation tensor

continued on next page

continued from previous page	
$\bar{\mathbf{C}}^e$	Right Cauchy-Green deformation tensor in the intermediate configuration
d	Grain size in Chapter 3
d_{grain}	Grain size in Chapter 5
d_{th}	Minimum twin spacing under which no pile up occurs
d_{twin}	Twin spacing
D	Grain boundary rate-potential functional per unit volume
D^{eff}	Grain boundary effective rate-potential functional per unit volume
D_{gb}^{eff}	Grain boundary effective rate-potential functional per unit surface
E	Internal energy
E^B	Bulk Young's modulus
E_H	Internal energy behind the shock front
$\mathbf{E}$	Lagrangian strain tensor
$\bar{\mathbf{E}}^e$	Lagrangian strain tensor in the intermediate configuration
f_{TBAZ}	Volume fraction of the TBAZ
$\mathbf{f}$	Internal grain boundary force
$\mathbf{F}$	Deformation gradient tensor
$\mathbf{F}^e$	Elastic deformation gradient tensor
$\mathbf{F}_H$	Deformation gradient tensor behind the shock front
$\mathbf{F}^p$	Plastic deformation gradient tensor
$\mathbf{F}_0$	Deformation gradient tensor at the initial state
g_0^{hard}	Hard mode critical resolved shear stress
g_0^{soft}	Soft mode critical resolved shear stress
g_{th}	Critical resolved shear stress at d_{th}
g^α	Critical resolved shear stress on slip system α
h	Grain boundary width
h_{elt}	Element size

continued on next page

continued from previous page	
$h^{\alpha\alpha}$	Hardening diagonal modulus of slip system α
$\mathbf{I}$	Unit tensor
J	Jacobian
J_H	Jacobian behind the shock front
$\dot{K}$	Kinetic power
$\mathbf{K}$	Internal grain boundary stiffness matrix
l	Distance between two forests of dislocations
$\bar{\mathbf{L}}^p$	Plastic velocity gradient
m	Grain boundary strain rate sensitivity exponent
m_{TBAZ}	Strain rate sensitivity exponent for the TBAZ
m_{XTL}	Strain rate sensitivity exponent for crystal interior
m^α	Strain rate sensitivity exponent on slip system α
$\bar{\mathbf{m}}_\alpha$	Slip plane normal on slip system α
$\mathbf{M}$	Plastic flow tensor
n	Grain boundary plastic hardening exponent
n^B	Grain bulk plastic hardening exponent
n^α	Density of obstacles in slip system α
N_a	Shape function associated to node a
$\mathbf{n}$	Grain boundary normal in the deformed configuration
$\mathbf{N}$	Grain boundary normal in the initial configuration
P	Pressure
P^D	Total deformation power
P_H	Hugoniot pressure
$\mathbf{P}$	First Piola-Kirchoff stress tensor
$\bar{\mathbf{P}}$	First Piola-Kirchoff stress tensor in the intermediate configuration
$\mathbf{q}$	Grain boundary internal variables vector
	continued on next page

continued from previous page	
$\bar{\mathbf{Q}}$	Internal variables vector in the intermediate configuration
r	Numerical coefficient modulating the strength of obstacles
s	Slope of the Hugoniot
s^α	Strength of the obstacle in slip plane α given by a pair of forest dislocations
s_α	Local coordinate along the grain boundary element covariant basis vector $\mathbf{a}_\alpha$
$\mathbf{s}$	Deviatoric component of the grain boundary thermodynamic force associated to $\boldsymbol{\epsilon}$
$\mathbf{s}^c$	Deviatoric component of the grain boundary backstress tensor
$\bar{\mathbf{s}}_\alpha$	Slip direction on slip system α
$\mathbf{S}$	Second Piola-Kirchoff stress tensor
$\bar{\mathbf{S}}$	Second Piola-Kirchoff stress tensor in the intermediate configuration
t	Time
T	Temperature
T_m	Melting temperature
T_{m_0}	Melting temperature at ambient temperature
$T_{m,p}$	Slope of the melting temperature curve
$\mathbf{t}$	Grain boundary traction
U_p	Material velocity
U_s	Shock velocity
V	Specific volume
V_H	Specific volume behind the shock front
V_0	Specific volume at the initial state
$\dot{W}$	Total power of the external loads
$\dot{W}_{gb}$	Deformation power associated with the grain boundary
$\mathbf{x}_a$	Coordinates of node a
$\mathbf{x}_a^+$	Coordinates for node a on the top surface of the grain boundary
$\mathbf{x}_a^-$	Coordinates for node a on the bottom surface of the grain boundary

continued on next page

continued from previous page	
$\tilde{\mathbf{x}}_a$	Coordinates for node a on the mean surface of the grain boundary
Y	Grain boundary thermodynamic force associated to $\bar{\epsilon}^p$
β_{TQ}	Taylor-Quinney coefficient
$\delta_{\max}$	Maximum slip per unit length
Δt	Time step
ΔT_{EOS}	Increment of temperature due to the EOS during Δt
$\Delta T_{\text{plastic}}$	Increment of temperature due to plastic dissipation during Δt
Δu	Velocity jump across the element
$\boldsymbol{\delta}$	Displacement jump at the grain boundary
$\boldsymbol{\delta}^e$	Elastic component of the displacement jump at the grain boundary
$\boldsymbol{\delta}_n$	Normal component of the displacement jump at the grain boundary
$\boldsymbol{\delta}^p$	Plastic component of the displacement jump at the grain boundary
$\boldsymbol{\delta}_s$	Sliding component of the displacement jump at the grain boundary
$\bar{\epsilon}_p^B$	Grain bulk effective plastic grain
ϵ_0^B	Grain bulk reference plastic strain
$\dot{\epsilon}_0^B$	Grain bulk reference plastic strain rate
$\bar{\epsilon}^p$	Grain boundary effective plastic grain
ϵ_0	Grain boundary reference plastic strain
$\dot{\epsilon}_0$	Grain boundary reference plastic strain rate
$\boldsymbol{\epsilon}$	Strain at the grain boundary
$\boldsymbol{\epsilon}^e$	Elastic component of the grain boundary strain
$\boldsymbol{\epsilon}_n$	Normal component of the grain boundary strain
$\boldsymbol{\epsilon}^p$	Plastic component of the grain boundary strain
$\boldsymbol{\epsilon}_s$	Sliding component of the grain boundary strain
η	Artificial viscosity
η_T	Thermal softening exponent
	continued on next page

continued from previous page	
γ	Grüneisen parameter
γ_a	Accumulated sum of slips
γ_H	Grüneisen parameter behind the shock front
$\gamma_{\max}$	Maximum shear strain
γ_{sat}	Saturation shear slip
$\dot{\gamma}_0$	Reference shear strain rate
γ^α	Shear strain on slip system α
γ_c^α	Characteristic shear strain on slip system α
μ	Grain boundary frictional coefficient in Chapter 4
μ	Shear modulus in Chapter 5
ν^B	Bulk Poisson's ratio
ν_α	Hardening exponent in slip system α
ρ	Density
ρ_H	Density behind the shock front
ρ_{sat}	Saturation dislocation density
ρ_0	Density in the initial configuration
ρ_0^B	Bulk density in the initial configuration
ρ^α	Dislocation density in slip system α
σ_n	Grain boundary normal stress
σ_y	Grain boundary yield stress corresponding to stored hardening mechanisms
σ_0	Grain boundary initial yield stress
$\tilde{\sigma}_0$	Grain boundary rate-independent yield stress function
σ_0^B	Grain bulk initial yield stress
$\boldsymbol{\sigma}$	Grain boundary thermodynamic force associated to $\boldsymbol{\epsilon}$
$\boldsymbol{\sigma}^c$	Grain boundary backstress tensor
$\bar{\boldsymbol{\Sigma}}$	Stress measure conjugate to $\bar{\mathbf{L}}^p$ in the intermediate configuration
	continued on next page

continued from previous page	
τ^α	Resolved shear stress on slip system α
τ_c^α	Characteristic resolved shear stress on slip system α
τ_0^α	Critical resolved shear stress for slip system α
$\boldsymbol{\varphi}$	Deformation mapping
$\boldsymbol{\varphi}^+$	Deformation mapping for the top surface of the grain boundary
$\boldsymbol{\varphi}^-$	Deformation mapping for the bottom surface of the grain boundary
$\tilde{\boldsymbol{\varphi}}$	Mean deformation mapping of the grain boundary
Ψ^*	Grain boundary pseudo-potential of dissipation
Ψ_B^*	Grain bulk pseudo-potential of dissipation
∇_0	Gradient operator with respect to the initial configuration
∂B_0	External boundary of the aggregate polycrystal in the initial configuration
∂B_0^{ext}	External exposed boundary of grain g in the initial configuration
∂B_0^g	Boundary of grain g in the initial configuration
∂B_0^{gb}	Grain boundary surface in the initial configuration

Chapter 1

Introduction

Because of their potential for achieving higher material strength [1, 2, 3, 4, 5, 6], nanocrystalline metals, *i.e.* metals with a polycrystalline structure and grain sizes in the nanometer range, have recently elicited significant interest. Figure 1-1 shows the Transmission Electron Microscopy (TEM) image of an electrodeposited Ni nanocrystal with an average grain size of $\sim 30nm$ [1]. Efforts to characterize and understand the mechanical behavior of these materials have unveiled some unique features of deformation that are not commonly observed in polycrystals. It appears that grain boundary deformation mechanisms in metals structured at the nanometer scale are responsible for this departure from the mechanical behavior of conventional polycrystalline materials. It is therefore important and opportune to devise theories describing the mechanical behavior of nanocrystals.

One of the peculiar behaviors of the mechanical response of nanocrystal is the dependence of strength on grain size. Conventional microcrystalline polycrystals have long been known to exhibit an increase of the yield stress with a decrease of the grain size. This behavior has been observed to agree with the Hall-Petch [7, 8] relation:

$$\sigma_y = \sigma_0 + kd^{-\frac{1}{2}} \tag{1.1}$$

where k is a positive multiplicative constant and σ_0 is the lattice friction stress.

Based on this observation, microstructure refinement has been exploited as a

Figure 1-1: TEM image of electrodeposited nanocrystalline Ni with an average grain size of $\sim 30nm$ [1]

means of producing materials with increased strength. A long standing goal in Materials Sciences has been to determine the limits of the Hall-Petch relation. Starting with the pioneering—albeit controversial—experiments of Chokshi *et al.* [9], there has been experimental evidence that the yield stress decreases when the grain size is reduced beyond a given grain size [10, 11, 12], see Figure 1-2. More curiously, their observations of the dependence of the yield stress on grain size also appeared to follow an inverse square root relation, Equation (1.1), but with a negative coefficient k. There has since been significant efforts to confirm and explain this inverse—sometimes also referred to as reverse—Hall-Petch effect. However, the experimental evidence is not conclusive and this aspect of the response of nanocrystals is still subject of considerable debate [13].

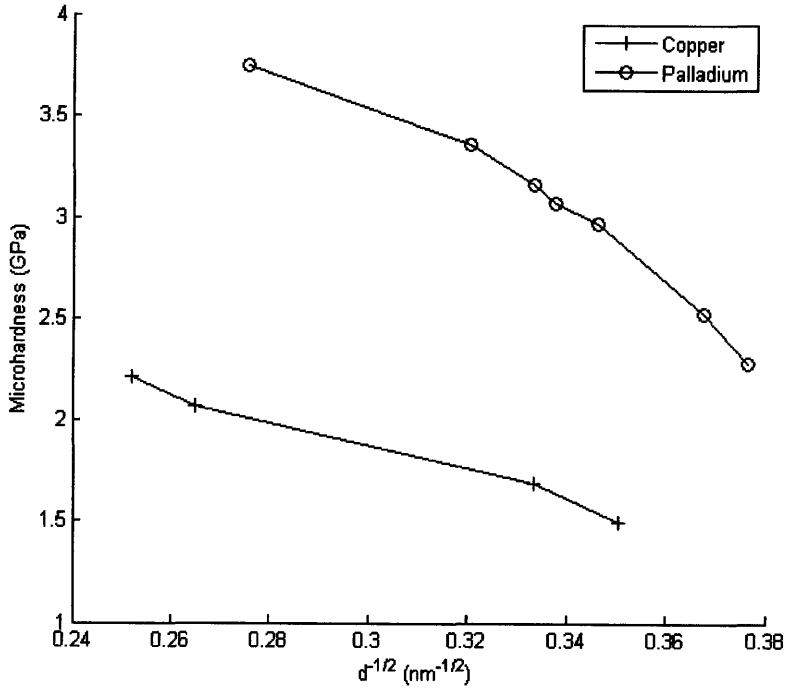

Figure 1-2: Chokshi's experimental observation of the reverse Hall-Petch effect on Cu and Pd [9] (microhardness from [10])

It is generally accepted that the direct Hall-Petch (HP) effect results from a hardening mechanism associated with the pile-up of lattice dislocations at the grain

boundaries. Nevertheless, as the grain size further decreases, the increase of the yield strength with microstructure refinement has been observed to level off at grain sizes of the order of 10 to 50 nm, switching to a decrease of strength with further reduction of grain size. Summarizing the experimental and theoretical findings, there is a growing consensus that the apparent anomalous dependence of yield stress on grain size can be rationalized by the activation of deformation mechanisms taking place at the grain boundary which compete with crystal plasticity and become the dominant operative dissipative deformation mechanisms when grain sizes are sufficiently small, leaving no room for dislocation activity inside the grains. Different grain boundary deformation mechanisms explaining this change of behavior have been proposed. Chokshi *et al.* initially suggested that Coble creep at room temperature was perhaps the mechanism explaining their experimental results [9]. Atomistic simulations of tensile tests on nanocrystalline metals have nevertheless shown a reverse Hall-Petch effect in the absence of thermally activated processes [14], see Figure 1-3. By contrast to the mechanism suggested by Chokshi, this and other atomistic simulation studies [15, 14, 16, 17, 18] have shown that the main deformation mechanism taking place at grain boundaries consists of localized sliding accompanied by some accommodation mechanism that maintains the intergrain compatibility, *e.g.* at triple points. However, there is still dissent on the nature of this accommodation process [14, 19]. Recent large-scale atomistic simulations have been able to show the crossover from the direct to the inverse grain-size dependence of material strength [20], see Figure 1-4. Experimental studies have also provided evidence of this peculiar behavior [21, 2, 11, 1].

A second important aspect of the response of nanocrystals of focus in this thesis is the observed glass-like behavior of grain boundaries. Recent studies [22] have shown an asymmetry in the compressive versus tensile stress-strain response of nanocrystalline nickel. This is consistent with the work of Wolf *et al.* reporting an amorphous state at grain boundaries [19] which suggests a frictional intergranular behavior characteristic of metallic glasses. Friction takes a new dimension in the shock response of nanocrystals. Molecular Dynamics (MD) simulations have suggested that the grain

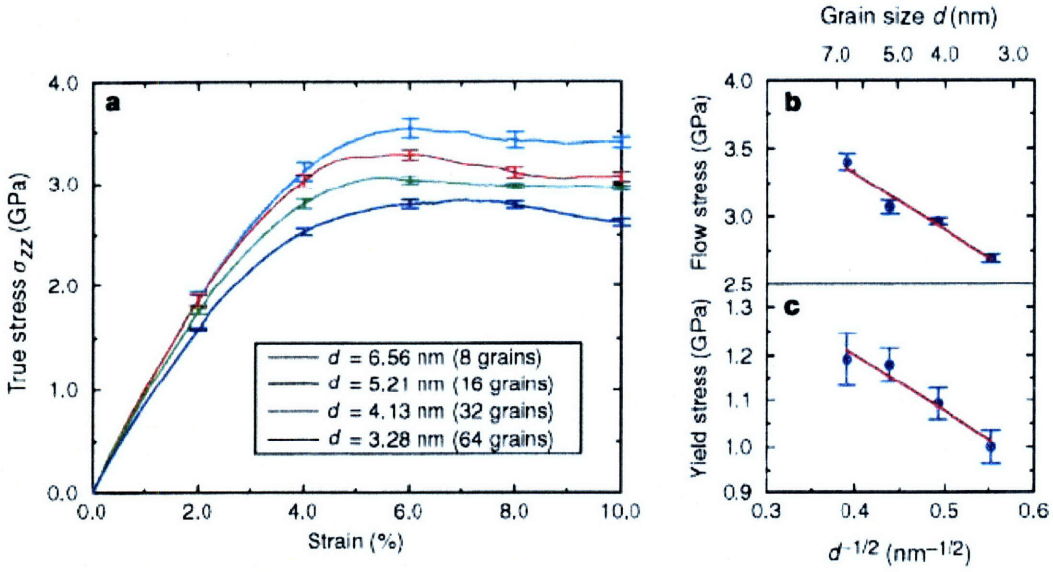

Figure 1-3: Molecular statics simulations by Schiøtz *et al.* (1998) [14] showing the reverse Hall-Petch Effect

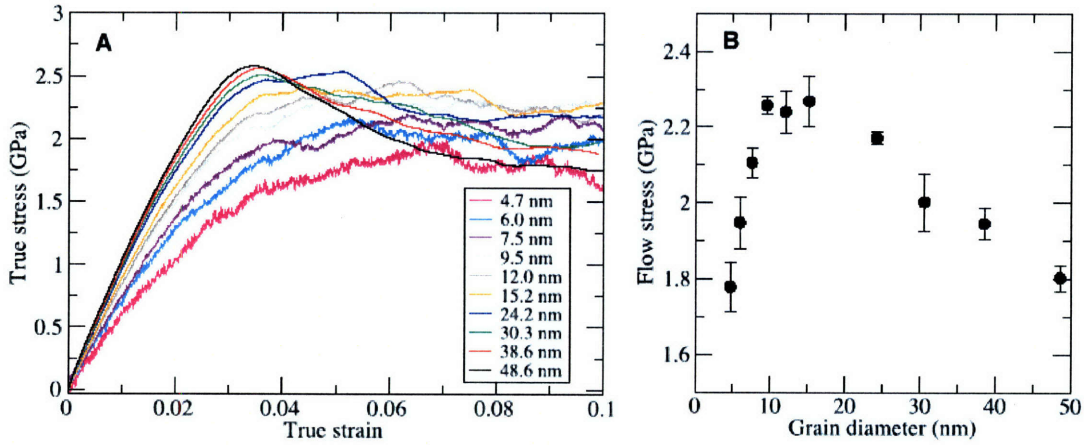

Figure 1-4: Molecular dynamics simulations by Schiøtz *et al.* (2003) [20] showing the crossover from the direct to the reverse Hall-Petch Effect

boundary glassy behavior leads to the inhibition of the sliding under strong state of compression, which forces the reactivation of intragrain dislocation as the main deformation process [23]. Figure 1-5 shows a snapshot of Bringa *et al.*'s MD simulation of shock propagation of a $\sim 50GPa$ pressure wave after $30ps$ in Cu nanocrystal with grain size of $20nm$. The shock front as well as the significant dislocation activity are clearly apparent. This reorganization of the deformation processes leads to a shift of the direct/inverse HP effect transition to higher strength and smaller grain size [23].

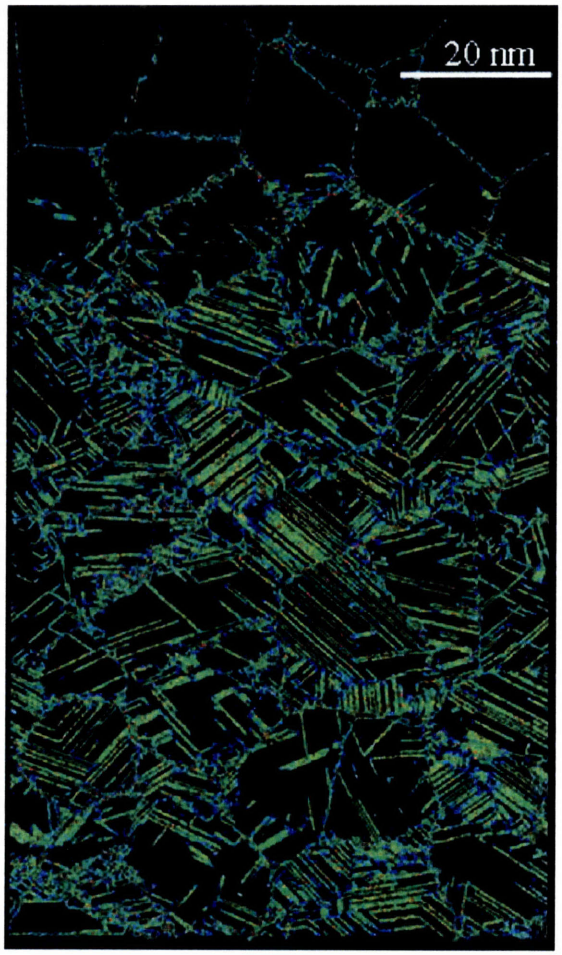

Figure 1-5: Snapshot of MD simulation of shock propagation of a $\sim 50GPa$ pressure wave after $30ps$ in Cu nanocrystal with grain size of $20nm$ [23]

Although it has been shown that nanocrystals with high ductility can be made under very careful processing conditions [24], it is generally observed that nanocrystals possess very low ductility [25, 26, 27]. A significant improvement in ductility

without compromising the strength observed in nanocrystals can be achieved by creating a microstructure of ultrafine crystals ($\sim 500nm$) with artificially grown nano-twins [26, 27, 28, 29, 30]. Figure 1-6 shows the TEM image of an electrodeposited nanocrystalline Cu with an average twin spacing of $\sim 15nm$ [28]. Figure 1-7 shows the comparison between stress-strain curves of coarse-grained (grain size $> 100\mu m$), nanocrystalline (grain size $\sim 30nm$) and nano-twinned (twin spacing $\sim 15nm$) Cu [26]. The gain of ductility and strength of nano-twinned Cu with respect to nanocrystalline and coarse-grained Cu is clearly illustrated. The work in these references shows that twin boundaries play the same role of a highly coherent grain boundary in inhibiting dislocation transmission. However, their complex and gradual loss of coherence during deformation delays to higher strains failure normally observed in disordered grain boundaries [30].

A summary of efforts to model the mechanical response of nanocrystalline metals has been recently presented in the review article by Meyers *et al.* [13]. This thesis endeavors to contribute to these efforts by devising continuum scale descriptions of the peculiar deformation and failure mechanisms in nanocrystalline metals which have not been accounted for in the past.

The first objective has been the development of a general continuum framework for describing grain boundary mechanics of deformation in nanocrystals. A literature review shows a limited number of contributions to the continuum description of nanocrystal response which are restricted to two-dimensional analysis or columnar microstructures [31, 32, 25, 33, 34, 35, 36], see Chapter 2 for more details. The model proposed in this thesis consists of a finite element formulation of the continuum three-dimensional problem with a special consideration of the boundaries between grains. Following what has been observed experimentally, grain boundaries are considered as having a small but finite size. Interface elements inspired by well-established descriptions of fracture and crack propagation [37] are formulated to account for the special kinematics of grain boundaries (i.e., to describe grain boundary sliding and other accommodation mechanisms). The amount of grain boundary sliding and accommodation is determined by a phenomenological model formulated within the

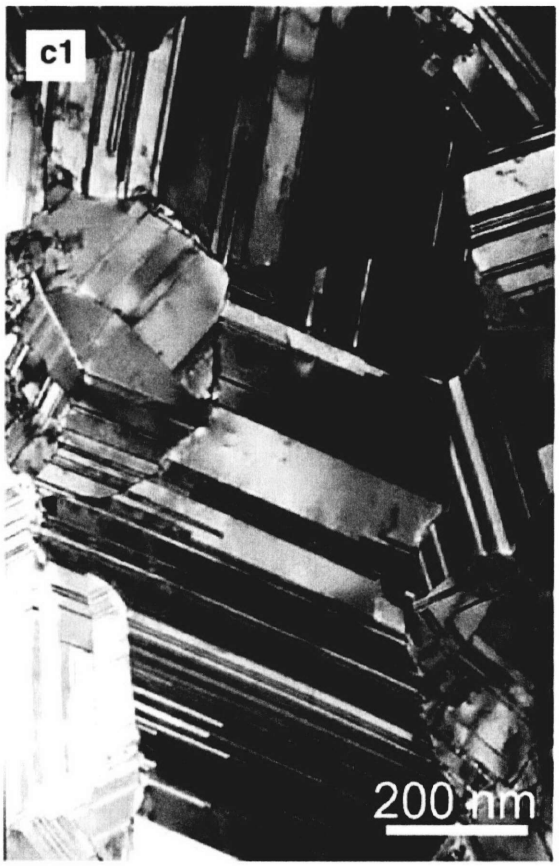

Figure 1-6: TEM image of electrodeposited nanocrystalline Cu with an average twin spacing of $\sim 15nm$ [28]

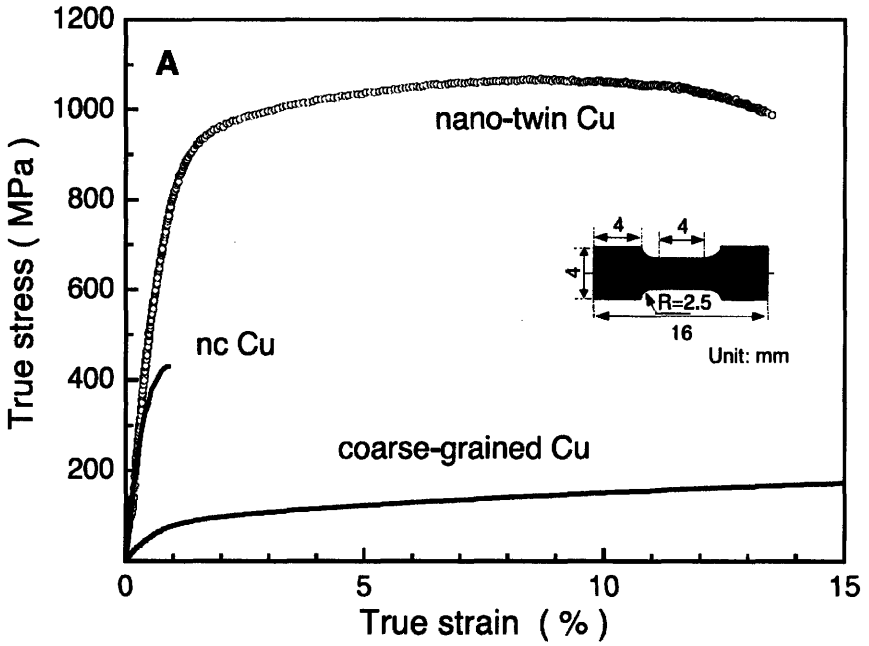

Figure 1-7: Comparison of strength and ductility of coarse (grain size $> 100\mu m$), nanocrystalline (grain size $\sim 30nm$) and nano-twinned (twin spacing $\sim 15nm$) grains from the corresponding strain-stress curves [26]

framework of variational constitutive updates [38, 39]. The model essentially considers the grain boundary as a slip plane in a similar manner to crystal plasticity models, but without a preferred slip direction. The opening mode is modeled with a similar plasticity formulation. In addition, a parallel implementation of this model is developed, enabling large-scale simulation of three-dimensional boundary value problems. In Chapter 2, the proposed three-dimensional continuum model of the deformation of nanocrystalline materials is described in details including the continuum framework, the constitutive models and the numerical approach.

In Chapter 3, the calibration of the model parameters against the atomistic and experimental results in [14, 17, 40, 41] is presented. Subsequently, the calibrated model is used to conduct numerical simulations of the tensile response of nanocrystalline copper under a wide range of grain sizes and strain rates. The ability to use rather large computational meshes enables the investigation of grain-size dependence of the nanocrystal effective response.

To this end, simulations of tensile tests are conducted on $100nm$ and $20nm$ sized nanocrystalline copper specimens of grain sizes ranging from $33.33nm$ to $3.33nm$. The numerical results are compared to both experimental [40, 41] and atomistic results [14, 17]. In particular, vastly different strain rate conditions similar to published experimental and atomistic results are simulated in an attempt to ascertain if the significantly different yield strengths predicted by those two approaches may be partially due to rate dependence effects. It bears emphasis that this ability to simulate wide ranges of loading rates is easily accessible to continuum models. The capability of the continuum model to describe the reverse Hall-Petch effect and, thus, confirm experimental and theoretical findings, as well as the overall effectiveness and versatility of the proposed continuum approach as an alternate tool to describe the behavior of nanocrystals is also discussed and summarized.

In Chapter 4, the model is extended and used to explore the response of nanocrystalline metals to shock loading. The shock of nanocrystals has been studied by Bringa *et al.* [23] using MD calculations. They highlighted the role of friction in the grain boundary under high pressure and its implications on the intragrain dislocation activity. The extensions involve the modification of the grain boundary sliding and accommodation model to account for the pressure-dependent frictional resistance of the grain boundary, the implementation of a high-rate equation of state (EOS), shock-capturing scheme to describe the volumetric response of the grain interiors under shock loading and a plasticity model to describe their deviatoric response. After calibration, the influence of the frictional mechanism is then studied and compared to Bringa *et al.*'s results [23]. It should finally be noted that, except for Wei *et al.*'s models [31, 32], there has not been significant efforts to model the frictional behaviors of grain boundaries. Both references either decided to neglect this effect or concluded that there is a small contribution of friction under slow-rate conditions as opposed to other mechanisms (*e.g.* cavitation of grain boundaries). These works nevertheless did not tackle the relative importance of this phenomenon under extremely high pressure.

Chapter 5 is devoted to the development, calibration and testing of a model of ultrafine crystals with embedded growth twins. The model represents an extension

of the two-dimensional work of Dao *et al.* [29] to three dimensions. The approach is based on a crystal plasticity model for the bulk where slip, hardening and rate dependence are modified to account for the presence of twin boundaries which act as dislocation barriers. In addition, a failure criterion similar to the one developed by Dao *et al.* [29] is conceived, which consists of a limited value of slip of the twin planes. This extension enables the consideration of out-of-plane slip, cross slip/hardening and grain rotation. The results are compared with the two-dimensional model of Dao *et al.* and with the experiments of Lu *et al.* [29, 27], and the model is finally used for studying the three-dimensional aspects of dependence of the stress-strain response of ultrafine copper on twin density.

The main conclusion of this thesis is that the continuum approach provides a plausible modeling approach for describing the unique nanoscale mechanisms of deformation and failure in nanocrystals as well as in nano-twinned ultrafine crystals. The large-scale parallel computational framework proposed here provides a good complement to experiments and to atomistic simulations.

Chapter 2

Continuum modeling framework for nanocrystals

To a large extent, the mechanical behavior of nanocrystals has been modeled using large scale atomistic simulation. Whereas this approach has been very successful in unveiling the basic deformation mechanisms taking place in nanocrystals, the need to represent and account for the dynamics of each individual atom poses severe restrictions on the number of grains and/or the extent of the nanocrystalline sample sizes that can be simulated. For instance, only recently has it been possible to simulate grain and sample sizes that capture the transition from the inverse to the direct Hall-Petch effect [20]. In addition, the time scales available to molecular dynamics simulation are also severely constrained by the need to track the dynamics of individual atoms. A common approach to circumvent this limitation is to impose extremely large deformation rates in the simulations ($10^8 s^{-1}$ and higher are not uncommon), which allows them to reach significant values of strain in very short—picoscale—times. However, these strain rate levels are not realistic except when studying the material response to shock loading. Another alternative is to use Molecular Statics models but in this case thermally activated processes are neglected.

There is then opportunity to explore the continuum framework for modeling the basic deformation mechanisms of nanocrystalline metals. Among the continuum approaches that have been proposed for modeling the response of nanocrystals, two

basic strategies can be identified. In the first approach, separate models are used to describe the mechanisms that are specific to the grain bulk and the grain boundary, and the effective response of the aggregate is obtained by recourse to homogenization [42, 33, 43, 44]. This type of model has been used to study the competitive mechanisms of deformation for a wide range of grain sizes and to identify the optimum grain size for a maximum strength.

The second approach is based on an explicit discretization of the microstructure using the Finite Element Method (FEM). Two different variants of this approach have been proposed. The first one considers the grain boundary and its affected zone ("grain boundary affected zone" or GBAZ) explicitly as a continuum with a finite thickness and different properties from the bulk [25, 33, 34, 32]. The second variant uses interface elements in the finite element mesh for the description of the grain boundaries [31, 36]. It should be emphasized that these modeling efforts were limited to two-dimensional analysis or three-dimensional analysis of two-dimensional (or columnar) microstructures and focused on the ability of the continuum approach to describe grain size dependence [31, 32, 36], strain localization [34, 36] and failure [31, 32].

The general continuum modeling approach adopted in this thesis falls within the category just described. The model consists of a finite element formulation of the continuum three dimensional problem describing the polycrystal grains explicitly and where grain boundaries are treated as discontinuity surfaces embedded in the continuum. Interface elements inspired in well-established descriptions of fracture and crack propagation are formulated to account for the special kinematics of grain boundaries, i.e., to describe grain boundary sliding as well as other accommodation mechanisms. Finally, a phenomenological model formulated within the framework of variational constitutive updates is proposed to describe the operative grain boundary deformation mechanisms of sliding and opening accommodation.

2.1 Continuum formulation

2.1.1 Governing equations

We assume from the outset that the kinematics of the deformation mechanisms taking place at grain boundaries may be described as surfaces of discontinuity embedded in an otherwise continuous medium. Toward this end, we adopt the continuum framework described in [37], which we briefly summarize in this section. The undeformed polycrystal lies in the region of space occupied by the set $B_0 = \bigcup_g B_0^g \subset \mathbb{R}^3$, where B_0^g is the region occupied by grain g, and undergoes a motion $\boldsymbol{\varphi} : B_0 \times [0,t] \rightarrow \mathbb{R}^3$, where $[0,t]$ is the time interval considered. In the continuous regions of the polycrystal, i.e. the grain interiors, local information about the material deformation is conveyed by the deformation gradients $\mathbf{F}$, whereas the local stress state is described by the first Piola-Kirchhoff stress tensor $\mathbf{P}$, [45]. Figure 2-1 shows a representative intergrain boundary surface ∂B_0^{gb} whose unit normal is $\mathbf{N}$. Considering a grain in isolation, the power expended by the boundary tractions $\mathbf{t}$, which includes both the external as well as the intergranular tractions, is given by the expression:

$$\int_{\partial B_0^g} \mathbf{t} \cdot \dot{\boldsymbol{\varphi}} dS_0 \tag{2.1}$$

where ∂B_0^g includes the externally exposed ∂B_0^{ext} (if any) as well as the intergrain ∂B_0^{gb} portions of the grain boundary, i.e. $\partial B_0^g = \partial B_0^{ext} \cup \partial B_0^{gb}$. The total power of the surface tractions is:

$$\sum_g \int_{\partial B_0^g} \mathbf{t} \cdot \dot{\boldsymbol{\varphi}} dS_0 = \int_{\partial B_0} \mathbf{t} \cdot \dot{\boldsymbol{\varphi}} dS_0 + \underbrace{\sum_{gb\pm} \int_{\partial B_0^{gb\pm}} \mathbf{t} \cdot \dot{\boldsymbol{\varphi}} dS_0}_{\dot{W}_{gb}} \tag{2.2}$$

where $\partial B_0 = \bigcup_g \partial B_0^{ext}$ is the external boundary of the aggregate polycrystal, $\dot{W}_{gb}$ represents the deformation power associated with the grain boundary and the $\pm$ sign indicates that the surface integral is to be computed on both sides of the intergrain boundaries.

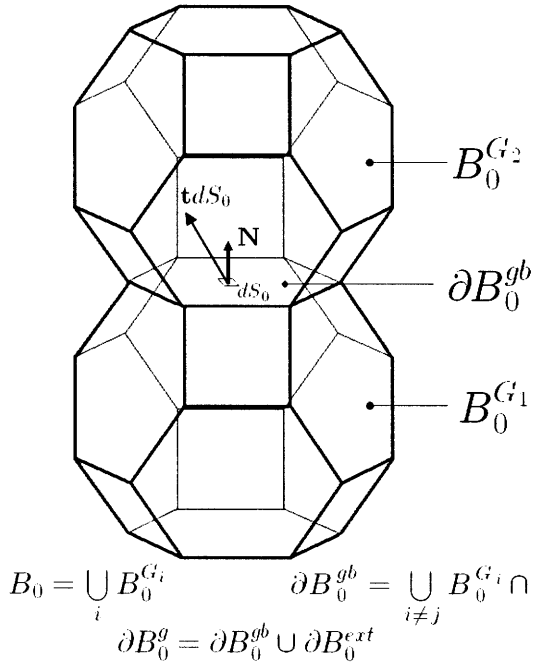

Figure 2-1: Schematic of geometric model of nanocrystals as a continuum with surfaces of discontinuity at grain boundaries

Inspired by atomistic simulations showing that grain boundary sliding and other accommodation mechanisms become operative in the deformation of nanocrystals [15, 14, 16, 17, 18], here and subsequently we allow for discontinuous displacements across the grain boundaries. Equation (2.2) then shows that the resulting finite displacement jumps $\boldsymbol{\delta} = [\![\boldsymbol{\varphi}]\!] = \boldsymbol{\varphi}^+ - \boldsymbol{\varphi}^-$ at the grain boundary constitute the appropriate deformation measure that is work-conjugate to the intergrain boundary tractions. In addition, balance of linear momentum requires $\mathbf{P} \cdot \mathbf{N} = \mathbf{t}$ on ∂B_0^g and the tractions to be continuous across the intergrain boundaries, i.e. $[\![\mathbf{t}]\!] = [\![\mathbf{P} \cdot \mathbf{N}]\!] = \mathbf{0}$. The total power of the external loads including the body forces $\rho_0 \mathbf{b}$ is therefore:

$$\begin{aligned} \dot{W} &= \int_{B_0} \rho_0 \mathbf{b} \cdot \dot{\boldsymbol{\varphi}} dV_0 + \int_{\partial B_0} \mathbf{t} \cdot \dot{\boldsymbol{\varphi}} dS_0 + \sum_{gb} \int_{\partial B_0^{gb}} \mathbf{t} \cdot [\![\dot{\boldsymbol{\varphi}}]\!] dS_0 \\ &= \int_{B_0} (\rho_0 \mathbf{b} + \nabla_0 \cdot \mathbf{P}) \cdot \dot{\boldsymbol{\varphi}} dV_0 + \int_{B_0} \mathbf{P} \cdot \dot{\mathbf{F}} dV_0 + \sum_{gb} \int_{\partial B_0^{gb}} \mathbf{t} \cdot [\![\dot{\boldsymbol{\varphi}}]\!] dS_0 \end{aligned} \tag{2.3}$$

The deformation power is the portion of the external power not consumed in increas-

ing the kinetic energy $K = \sum_g \int_{B_0^g} \frac{1}{2}\rho_0 |\dot{\boldsymbol{\varphi}}|^2 dV_0$:

$$P^D = \dot{W} - \dot{K} = \int_{B_0} \mathbf{P} \cdot \dot{\mathbf{F}} dV_0 + \underbrace{\sum_{gb} \int_{\partial B_0^{gb}} \mathbf{t} \cdot [\![\dot{\boldsymbol{\varphi}}]\!] dS_0}_{\dot{W}_{gb}} \tag{2.4}$$

where linear momentum balance $\nabla_0 \cdot \mathbf{P} - \rho_0(\ddot{\boldsymbol{\varphi}} - \mathbf{b}) = 0$ inside the grains B_0^g has been imposed. It becomes clear from Equation (2.4) that in this polycrystal modeling framework, the deformation power encompasses the contributions of the internal stresses inside each grain, as in conventional continuous solids, as well as those of the intergranular tractions which are work-conjugate to the displacement jumps describing the deformation mechanisms at the intergrain boundaries.

Taking as a starting point the work conjugacy relations suggested by the deformation power identity, Equation (2.4), we develop a constitutive framework for the mechanical behavior of nanocrystalline materials including grain boundary deformation mechanisms.

Atomistic simulation studies have shown that dislocation-mediated plastic deformation inside the grains in nanocrystalline materials is ostensibly impeded [17, 20]. Consequently and in order to reveal the independent role played by grain boundary deformation mechanisms, we will assume that the grain interiors can only undergo a reversible, i.e. elastic, lattice distortion and rotation. The competition between intra-grain crystal plasticity and grain boundary deformation has been discussed in [43, 31, 36]. Under moderate loading condition, the distortion of the lattice is then expected to be small and a linear relation between the Lagrangian strain tensor $\mathbf{E} = (\mathbf{C} - \mathbf{I})/2$ and the second Piola-Kirchhoff $\mathbf{S} = \mathbf{F}^{-1}\mathbf{P}$ can be assumed, see Chapter 3. In these expressions, $\mathbf{C} = \mathbf{F}^T\mathbf{F}$ is the right Cauchy-Green deformation tensor and $\mathbf{I}$ is the unit tensor. In the case of intense shock loading consideration, the elastic response requires additional considerations, see Chapter 4.

As suggested by Equation (2.4), the displacement jumps across the grain boundary $\boldsymbol{\delta}$ are taken as the kinematic variable or deformation measure, whereas the grain boundary traction vector $\mathbf{t}$ is taken as the corresponding work-conjugate stress mea-

sure. It should be noted that $\boldsymbol{\delta}$ vanishes for a rigid body motion, as should be the case for an appropriate deformation measure.

2.1.2 Kinematic assumptions

For the purpose of tracking geometric information of the deformed grain boundary surface, we conventionally define the mean deformation mapping [37]:

$$\tilde{\boldsymbol{\varphi}} = \frac{1}{2}\left(\boldsymbol{\varphi}^{+} + \boldsymbol{\varphi}^{-}\right) \tag{2.5}$$

from which the original deformation mapping on both sides of the grain boundary can be recovered as:

$$\boldsymbol{\varphi}^{\pm} = \tilde{\boldsymbol{\varphi}} \pm \frac{1}{2}\left(\boldsymbol{\varphi}^{+} - \boldsymbol{\varphi}^{-}\right) = \tilde{\boldsymbol{\varphi}} \pm \frac{1}{2}\boldsymbol{\delta} \tag{2.6}$$

Thus, the deformed grain boundary is defined as $S \equiv \tilde{\boldsymbol{\varphi}}(S_0)$. Given a parametrization $\tilde{\boldsymbol{\varphi}} = \tilde{\boldsymbol{\varphi}}(s_\alpha), \alpha = 1, 2$ of S, as subsequently provided by the finite element discretization of the grain boundaries, the deformed surface normal $\mathbf{n}$ may be obtained directly from the covariant basis vectors $\mathbf{a}_\alpha = \tilde{\boldsymbol{\varphi}}_{,\alpha}$ as:

$$\mathbf{n} = \frac{\mathbf{a}_1 \times \mathbf{a}_2}{\|\mathbf{a}_1 \times \mathbf{a}_2\|} \tag{2.7}$$

The displacement jumps may then be decomposed into an opening separation vector and a grain boundary sliding vector as follows:

$$\boldsymbol{\delta}_n = (\boldsymbol{\delta} \cdot \mathbf{n})\,\mathbf{n} = (\mathbf{n} \otimes \mathbf{n}) \cdot \boldsymbol{\delta} \tag{2.8}$$

$$\boldsymbol{\delta}_s = \boldsymbol{\delta} - \boldsymbol{\delta}_n = (\mathbf{I} - \mathbf{n} \otimes \mathbf{n}) \cdot \boldsymbol{\delta} \tag{2.9}$$

In addition, the mean deformation of the grain boundary surface may be measured by the material gradient of the mean deformation mapping $\nabla_{S_0}\tilde{\boldsymbol{\varphi}}$. It is worth noting that the mean deformation of the grain boundary surface $\nabla_{S_0}\tilde{\boldsymbol{\varphi}}$ describes in-plane stretching and shearing deformation of the grain boundary in the absence of relative grain sliding or opening. In particular, the surface deformation gradient conveys

information about the normal, Equation (2.7), and the surface deformation as measured by the surface Cauchy-Green deformation tensor $\mathbf{C}_{S_0} = (\nabla_{S_0}\tilde{\boldsymbol{\varphi}})^T \nabla_{S_0}\tilde{\boldsymbol{\varphi}}$. This information would be required in models accounting for the influence of grain boundary misorientation or preferred sliding directions. However, due to the absence of supporting experimental evidence such additional complexities will be ignored.

These kinematic assumptions lead to a constant state of deformation across the thickness h of the grain boundary which can be expressed in the local orthonormal reference frame $(\mathbf{n}_1, \mathbf{n}_2, \mathbf{n}_3) = (\frac{\mathbf{a}_1}{|\mathbf{a}_1|}, \frac{\mathbf{n}\times\mathbf{a}_1}{|\mathbf{n}\times\mathbf{a}_1|}, \mathbf{n})$ as :

$$\boldsymbol{\epsilon} = \underbrace{\frac{\boldsymbol{\delta}_n \cdot \mathbf{n}_3}{h}\, \mathbf{n}_3 \otimes \mathbf{n}_3}_{\boldsymbol{\epsilon}_n} + \underbrace{\frac{\boldsymbol{\delta}_s \cdot \mathbf{n}_1}{h}\, \frac{1}{2}\left(\mathbf{n}_1 \otimes \mathbf{n}_3 + \mathbf{n}_3 \otimes \mathbf{n}_1\right) + \frac{\boldsymbol{\delta}_s \cdot \mathbf{n}_2}{h}\, \frac{1}{2}\left(\mathbf{n}_2 \otimes \mathbf{n}_3 + \mathbf{n}_3 \otimes \mathbf{n}_2\right)}_{\boldsymbol{\epsilon}_s} \tag{2.10}$$

It should be noted that h introduces a characteristic length scale in the model. The above expression also shows that the strain tensor additively decomposes in a sliding part $\boldsymbol{\epsilon}_s$ and a normal opening part $\boldsymbol{\epsilon}_n$.

2.1.3 Variational constitutive framework

For the purpose of formulating constitutive models of grain boundary response and their corresponding algorithmic updates, we adopt the variational framework proposed in [38, 39]. It was shown in [38] that an incremental, pseudo-elastic strain energy density can be derived for a rather general class of elastic and inelastic materials, leading to algorithmic updates possessing a potential structure. An important advantage of this approach is that it naturally furnishes solutions of the incremental boundary value problem as the result of a variational statement. This approach was extended in [39], where, in addition, variational updates are presented for specific material models, including finite-deformation isotropic plasticity and single-crystal plasticity. More recently, the same framework has been used for developing models of non-cohesive granular media [46], porous plasticity [47], nonlinear viscoelasticity [48] and thermomechanics [49].

An internal variable formalism [50, 51] is adopted to describe inelastic processes

and a decoupled response in the opening and sliding components is postulated, *i.e.* that opening deformations do not cause sliding tractions, and vice versa. The free energy density may thus be additively decomposed into a sliding part A_s and an opening part A_n:

$$A(\boldsymbol{\epsilon}_s, \boldsymbol{\epsilon}_n, \mathbf{q}) = A_s(\boldsymbol{\epsilon}_s, \mathbf{q}) + A_n(\boldsymbol{\epsilon}_n, \mathbf{q}) \tag{2.11}$$

where $\mathbf{q} \in \mathbb{R}^n$ denotes a suitable set of internal variables. In the following, for simplicity of notation, we will drop the subscripts s and n, and treat both parts (sliding and opening) in an identical way.

We will consider that the material in the grain boundary undergoes an elasto-visco-plastic behavior. We will further assume that the strain additively decomposes in an elastic and a plastic part:

$$\boldsymbol{\epsilon} = \boldsymbol{\epsilon}^e + \boldsymbol{\epsilon}^p \tag{2.12}$$

which, given the linearity of relation (2.10), amounts to an additive decomposition of the displacement jump $\boldsymbol{\delta} = \boldsymbol{\delta}^e + \boldsymbol{\delta}^p$. We also define the equivalent plastic strain $\bar{\epsilon}^p$, linked to the tensorial plastic strain through the flow rule:

$$\dot{\boldsymbol{\epsilon}}^p = \dot{\bar{\epsilon}}^p \mathbf{M} \tag{2.13}$$

where $\mathbf{M}$ is a symmetric tensor verifying the following set of conditions (J_2 plasticity):

$$\begin{cases} \mathrm{tr}[\mathbf{M}] = 0 \\ \mathbf{M} \cdot \mathbf{M} = \frac{3}{2} \end{cases} \tag{2.14}$$

and otherwise undefined at this point. The set of internal variables is then $\mathbf{q} = \{\boldsymbol{\epsilon}^p, \bar{\epsilon}^p\}$. It will be determined by the variational principle described below. It will be assumed that the elastic response of the grain boundary is not affected by irreversible processes, as it is usually done for the elastic response of the crystal, and, thus, we can write

$$A(\boldsymbol{\epsilon}, \boldsymbol{\epsilon}^p, \bar{\epsilon}^p) = W^e(\boldsymbol{\epsilon} - \boldsymbol{\epsilon}^p) + W^p(\boldsymbol{\epsilon}^p, \bar{\epsilon}^p) \tag{2.15}$$

Taking into account the flow rule, the thermodynamic forces associated to $\boldsymbol{\epsilon}$ and $\bar{\epsilon}^p$

are respectively given by:

$$\boldsymbol{\sigma} = \frac{\partial A}{\partial \boldsymbol{\epsilon}} = \frac{\partial W^e}{\partial \boldsymbol{\epsilon}^e} \tag{2.16}$$

$$Y = -\frac{\partial A}{\partial \bar{\epsilon}^p} = (\boldsymbol{\sigma} - \boldsymbol{\sigma}^c) \cdot \mathbf{M} - \sigma_y \tag{2.17}$$

where $\boldsymbol{\sigma}^c = \partial_{\boldsymbol{\epsilon}^p} W^p(\boldsymbol{\epsilon}^p, \bar{\epsilon}^p)$ is the backstress tensor and $\sigma_y = \partial_{\bar{\epsilon}^p} W^p(\boldsymbol{\epsilon}^p, \bar{\epsilon}^p)$ is the yield stress corresponding to stored hardening mechanisms (by contrast to dissipative mechanisms). Finally, kinetic relations between Y and $\dot{\bar{\epsilon}}^p$ are given by a convex dissipation pseudo-potential Ψ^* (convexity ensures positive dissipation):

$$Y = \frac{\partial \Psi^*}{\partial \dot{\bar{\epsilon}}^p}(\dot{\bar{\epsilon}}^p; \bar{\epsilon}^p) \tag{2.18}$$

If we define the following functional [39]:

$$D = \dot{A} + \Psi^* = \boldsymbol{\sigma} \cdot \dot{\boldsymbol{\epsilon}} - Y\dot{\bar{\epsilon}}^p + \Psi^*(\dot{\bar{\epsilon}}^p; \bar{\epsilon}^p) \tag{2.19}$$

the constitutive relations are equivalent to the variational principle

$$D^{\text{eff}}(\dot{\boldsymbol{\epsilon}}; \boldsymbol{\epsilon}, \mathbf{q}) = \inf_{\dot{\bar{\epsilon}}^p, \mathbf{M}} D(\dot{\boldsymbol{\epsilon}}, \dot{\bar{\epsilon}}^p, \mathbf{M}; \boldsymbol{\epsilon}, \mathbf{q}) \tag{2.20}$$

Minimization of D with respect to $\mathbf{M}$ corresponds to the principle of maximum plastic dissipation, and yields, using Lagrange multipliers to enforce conditions (2.14):

$$\mathbf{M} = \sqrt{\frac{3}{2}} \frac{\mathbf{s} - \mathbf{s}^c}{\|\mathbf{s} - \mathbf{s}^c\|} \quad \text{where } \mathbf{s} = \text{dev}[\boldsymbol{\sigma}] \text{ and } \mathbf{s}^c = \text{dev}[\boldsymbol{\sigma}^c] \tag{2.21}$$

while the minimization with respect to $\dot{\bar{\epsilon}}^p$ yields the kinetic relations (2.18). An additional advantage of the variational formulation is that D^{eff} provides a rate-potential for the stress:

$$\boldsymbol{\sigma} = \frac{\partial D^{\text{eff}}}{\partial \dot{\boldsymbol{\epsilon}}}(\dot{\boldsymbol{\epsilon}}; \boldsymbol{\epsilon}, \mathbf{q}) \tag{2.22}$$

An incremental solution procedure that retains the variational properties is adopted to integrate the constitutive update following [39].

We consider here that grain boundary sliding occurs exclusively by dissipative hardening micromechanisms. This implies that

$$W^p(\boldsymbol{\epsilon}^p, \bar{\epsilon}_p) \equiv 0 \tag{2.23}$$

In the specific model used in calculations, the following dissipation pseudo-potential is adopted:

$$\begin{cases} \Psi^*(\dot{\bar{\epsilon}}_p, \bar{\epsilon}_p) = \tilde{\sigma}_0(\bar{\epsilon}_p)\dot{\epsilon}_0 \frac{1}{m+1}\left(1 + \frac{\dot{\bar{\epsilon}}_p}{\dot{\epsilon}_0}\right)^{m+1} \\ \tilde{\sigma}_0(\bar{\epsilon}_p) = \sigma_0\left(1 + \frac{\bar{\epsilon}_p}{\epsilon_0}\right)^n \end{cases} \tag{2.24}$$

where ϵ_0, $\dot{\epsilon}_0$, σ_0, m and n are model parameters. This expression leads to a power-law rate dependence and isotropic hardening model.

By combining Equations (2.17), (2.21), (2.23) and (2.24), we finally obtain:

$$Y = \sqrt{\frac{3}{2}(\mathbf{s} - \mathbf{s}^c).(\mathbf{s} - \mathbf{s}^c)} = \tilde{\sigma}_0(\bar{\epsilon}_p)\left(1 + \frac{\dot{\bar{\epsilon}}_p}{\dot{\epsilon}_0}\right)^m \tag{2.25}$$

With this constitutive framework in hand, the deformation power at the grain boundary (2.4) can be reformulated as

$$\dot{W}_{gb} = \sum_{gb} \int_{\partial B_0^{gb}} D_{gb}^{\text{eff}}(\dot{\boldsymbol{\delta}}; \boldsymbol{\delta}, \mathbf{q}) dS_0 \tag{2.26}$$

in terms of the effective rate potential D_{gb}^{eff} obtained by integrating (2.20) over the interface thickness using (2.10):

$$D_{gb}^{\text{eff}}(\dot{\boldsymbol{\delta}}; \boldsymbol{\delta}, \mathbf{q}) = \int_{-h/2}^{h/2} D^{\text{eff}}(\dot{\boldsymbol{\epsilon}}; \boldsymbol{\epsilon}, \mathbf{q}) d\zeta = h D^{\text{eff}}(\dot{\boldsymbol{\epsilon}}; \boldsymbol{\epsilon}, \mathbf{q}) \tag{2.27}$$

Using Equation (2.10), Equation (2.26) can then be simplified to:

$$\dot{W}_{gb} = \sum_{gb} \int_{\partial B_0^{gb}} \frac{\partial D_{gb}^{\text{eff}}(\dot{\boldsymbol{\delta}}; \boldsymbol{\delta}, \mathbf{q})}{\partial \dot{\boldsymbol{\delta}}} \dot{\boldsymbol{\delta}} dS_0 = \sum_{gb} \int_{\partial B_0^{gb}} h \frac{\partial D^{\text{eff}}(\dot{\boldsymbol{\epsilon}}; \boldsymbol{\epsilon}, \mathbf{q})}{\partial \dot{\boldsymbol{\delta}}} [\![\dot{\boldsymbol{\varphi}}]\!] dS_0 \tag{2.28}$$

Comparing this equation with (2.4) and using (2.22), the tractions are then given

by:

$$\mathbf{t} = h\frac{\partial D_{gb}^{\text{eff}}}{\partial \dot{\boldsymbol{\delta}}}(\dot{\boldsymbol{\epsilon}}; \boldsymbol{\epsilon}, \mathbf{q}) = h\boldsymbol{\sigma} \cdot \frac{\partial \boldsymbol{\epsilon}}{\partial \boldsymbol{\delta}} \tag{2.29}$$

which can be simplified, using (2.10), to

$$\mathbf{t} = \begin{pmatrix} \sigma_{13} \\ \sigma_{23} \\ \sigma_{33} \end{pmatrix} \tag{2.30}$$

where the vector components are expressed in the local reference frame.

2.2 Finite-element discretization

The continuum problem with embedded discontinuity surfaces representing the grain boundaries described above is approximated numerically using a conventional finite-element discretization for the grain interiors and a discretization of the grain boundary deformation power based on grain boundary interface elements. The geometric description of the interface elements follows [37]. In calculations, we use 10-node tetrahedral elements for the continuum which naturally suggests grain boundary elements as schematically shown in Figure 2-2. The interface element consists of two 6-node triangular surface elements lying on the positive S^+ and negative S^- sides of the grain boundary and offset along the normal by a distance equal to the grain boundary thickness h in the reference configuration. Therefore, the total number of nodes of the interface element is 12. The nodes are numbered from 1 to 6 and identified with $+$ $(-)$ if they lie on S^+ (S^-). The mean deformation mapping of the grain boundary $\tilde{\boldsymbol{\varphi}}$ (2.5) is discretized using the standard shape functions for a six-node triangular element $N_a(\xi_1, \xi_2), a = 1, \ldots, 6$ and the mean nodal coordinates $\tilde{\mathbf{x}}_a = \frac{1}{2}(\mathbf{x}_a^+ + \mathbf{x}_a^-)$, where $\mathbf{x}_a^{\pm}$ are the deformed nodal coordinates, as follows:

$$\tilde{\boldsymbol{\varphi}}_h(\boldsymbol{\xi}) = \sum_{a=1}^{6} N_a(\boldsymbol{\xi})\tilde{\mathbf{x}}_a \tag{2.31}$$

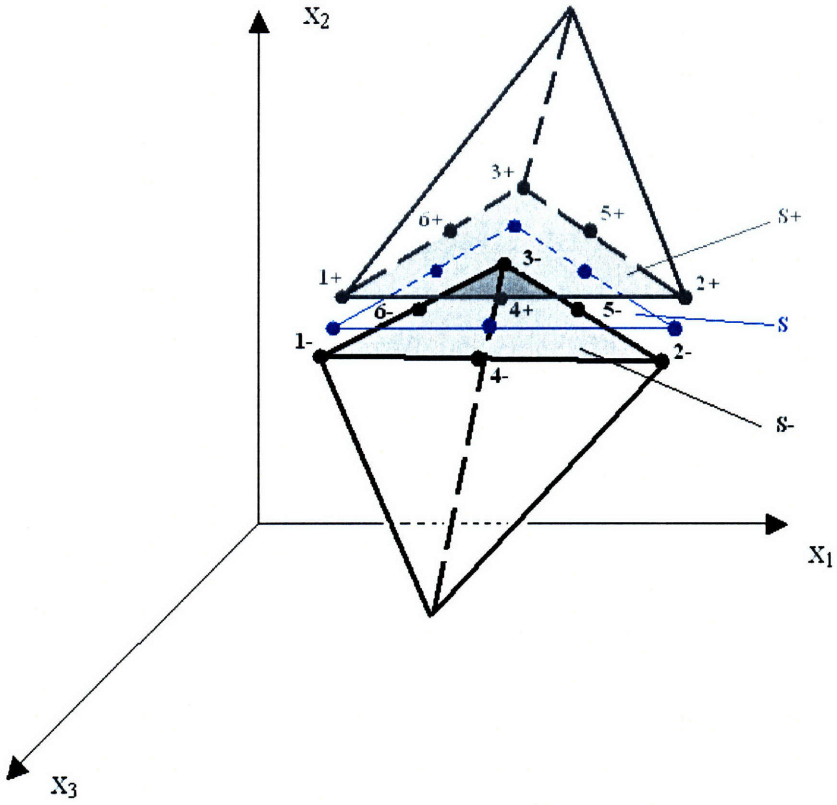

Figure 2-2: Schematic of grain boundary element. Two tetrahedra belonging to two adjacent crystals separated by an interface element at the grain boundary: $S+$ and $S-$ are respectively the facets corresponding to the tetrahedra on the positive and negative side as defined by the positive surface normal $\mathbf{N}$ and S is the midsurface

The isoparametric finite element interpolation of the middle surface of the interface element provides a parametric description of the element geometry in the deformed configuration from which all the geometric and kinematic quantities in Section 2.1.2 can be conveniently obtained, including the deformed unit surface normal (2.7) which is computed using the covariant basis vectors:

$$\mathbf{a}_\alpha(\boldsymbol{\xi}) = \tilde{\boldsymbol{\varphi}}_{h,\alpha}(\boldsymbol{\xi}) = \sum_{a=1}^{6} N_{a,\alpha}(\boldsymbol{\xi})\tilde{\mathbf{x}}_a \tag{2.32}$$

and the interpolation of the displacement jumps:

$$\boldsymbol{\delta}(\boldsymbol{\xi}) = [\![\boldsymbol{\varphi}_h]\!](\boldsymbol{\xi}) = \sum_{a=1}^{6} N_a(\boldsymbol{\xi})[\![\mathbf{x}_a]\!], \quad [\![\mathbf{x}_a]\!] = \mathbf{x}_a^+ - \mathbf{x}_a^- \tag{2.33}$$

An application of the discretized values of the kinematic variables to the effective grain boundary deformation power (2.26) leads to the expression of the internal grain boundary forces contributed by each grain boundary element:

$$f_{ia}^{\pm} = \mp \int_{S_0} t_i N_a dS_0 \tag{2.34}$$

with $\mathbf{t}$ given by (2.30), where S_0 is the reference configuration of the grain boundary element and N_a, the conventional shape functions corresponding to quadratic isoparametric triangular elements as shown in Figure 2-2. In these expressions, thus, the node identifier a ranges from 1 to 6 and the $+(-)$ sign applies to the nodes on the positive (negative) side of the grain boundary element as informed by the positive surface normal resulting from the finite element parametrization. The stiffness matrix

$$K_{iakb}^{\pm\pm} = \frac{\partial f_{ia}^{\pm}}{\partial x_{kb}^{\pm}} = \mp \int_{S_0} \frac{\partial t_i}{\partial x_{kb}^{\pm}} N_a dS_0 \tag{2.35}$$

is required in static calculations and can be obtained after a straightforward derivation

resulting in

$$\begin{aligned} K_{iakb}^{\pm\pm} = &\mp \pm \int_{S_0} \frac{n_{ji}}{2h} \frac{\partial \sigma_{j3}}{\partial \epsilon_{rl}} (\delta_{r3} n_{lk} + \delta_{l3} n_{rk}) N_b N_a dS_0 \\ &\mp \int_{S_0} \frac{n_{ji}}{4h} \frac{\partial \sigma_{j3}}{\partial \epsilon_{rl}} \delta_s \left(\delta_{r3} \frac{\partial n_{ls}}{\partial \bar{x}_{kb}} + \delta_{l3} \frac{\partial n_{rs}}{\partial \bar{x}_{kb}} \right) N_a dS_0 \\ &\mp \int_{S_0} \frac{\sigma_{j3}}{2} \frac{\partial n_{ji}}{\partial \bar{x}_{kb}} N_a dS_0 \end{aligned} \tag{2.36}$$

where

$$\frac{\partial n_{ls}}{\partial \bar{x}_{kb}} = \lambda_{skb} \delta_{l3} + \mu_{skb} \delta_{l1} + \nu_{skb} \delta_{l2} \tag{2.37}$$

and

$$\begin{cases} \lambda_{ikb} = \frac{e_{krs}}{|\mathbf{a}_1 \times \mathbf{a}_2|} (a_{2r} N_{b,1} - a_{1r} N_{b,2}) (\delta_{is} - n_{3i} n_{3s}) \\ \mu_{ikb} = \frac{N_{b,1}}{|\mathbf{a}_1|} \left(\delta_{ik} - \frac{a_{1i} a_{1k}}{|\mathbf{a}_1|^2} \right) \\ \nu_{ikb} = e_{ijl} (\lambda_{jkb} n_{1l} - \mu_{jkb} n_{3l}) \end{cases} \tag{2.38}$$

In these expressions, a_{ij} and n_{ij} correspond to the j^{th} component in the global referential of respectively $\mathbf{a}_i$ and $\mathbf{n}_i$, and δ_{ij} and e_{ijk} are respectively the Kronecker and the permutation symbols.

The preceding formulation of the grain boundary model was implemented as an addition to a research code for doing finite element analysis of material deformation for both implicit and explicit calculations. This implementation includes the ability of running the code in parallel, which allows large-scale computations as used in Chapters 4 and 5.

Chapter 3

Grain size dependence of the yield stress in nanocrystalline metals

In this chapter, the model presented in Chapter 2 is first calibrated to atomistic simulations and experimental tensile tests on nanocrystalline copper for a given grain size [14, 40]. The calibrated model is then used to evaluate the grain size and rate dependence of the yield stress. The results are compared with static experiments and atomistic simulations.

3.1 Simulation setup

The simulation domain consists of finite elements meshes of idealized polycrystalline samples in which individual grains are discretized and accounted for explicitly. The geometry of each grain corresponds to the tetrakaidecahedron which is the Wigner-Seitz cell corresponding to the b.c.c. lattice. This idealized grain morphology facilitates the automatic generation of conforming computational meshes of idealized polycrystalline samples with an arbitrary number of grains in three dimensions, and leads to nanostructures consisting of equiaxed grains. Each grain is discretized using 192 10-node tetrahedral finite elements in a manner that leaves the overall polycrystal mesh conforming at the grain boundaries. The idealized grain configurations are shown in Figure 3-1 with their corresponding designations.

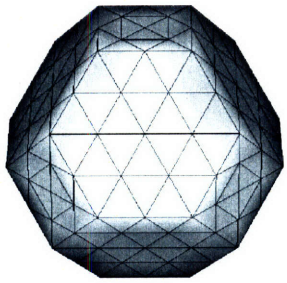

(a) **finite element mesh of a single grain**

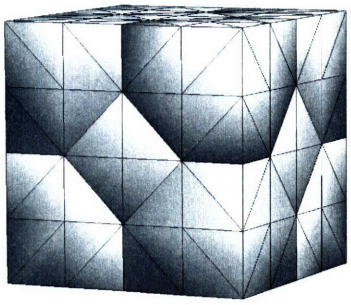

(b) **1x1x1: 9 grains**

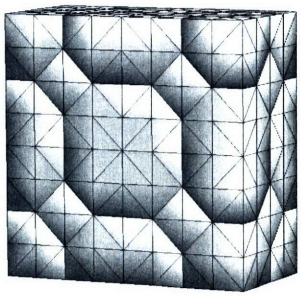

(c) **2x2x1: 22 grains**

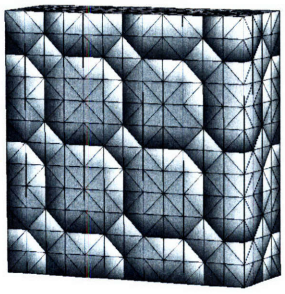

(d) **3x3x1: 41 grains**

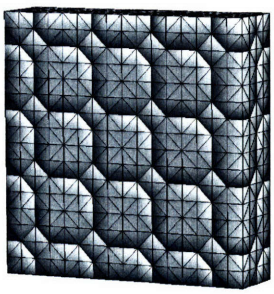

(e) **4x4x1: 66 grains**

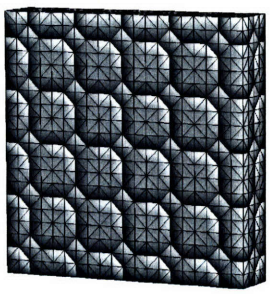

(f) **5x5x1: 97 grains**

Figure 3-1: Idealized polycrystal grain configurations used in calculations. Designation and number of grains

The notation "1x1x1" designates the microstructure with the fewest number of grains. This structure is a unit cell consisting of a full tetrakaidecahedron padded with eight grain eighths completing the regular cubic geometry. Similarly, the notation "1xnxn" designates a microstructure consisting of n^2 unit cells. This results in $n^2 + 2 \times (n+1)^2$ total number of grains including partial grains on the boundary.

Other approaches based on 3D Voronoï diagrams leading to more general microstructures is commonly used in MD descriptions or when non-conforming meshes are used [52]. However, the grain boundary modeling approach proposed in this work demands the conformity of the mesh across grain boundaries such that interface element can be properly defined, which requires the generation of a general unstructured mesh. Despite the obvious limitations of our approach (*e.g.* preventing the consideration of a grain size distribution), the lack of an automated procedure to generate 3D Voronoï microstructures and the need to obtain a large number of computational meshes, suggested that the idealized microstructures adopted here are reasonable for studies of grain size dependencies.

In light of the availability of experimental characterizations and atomistic descriptions of the grain size dependence of strength on nanocrystalline copper [14, 17, 10, 53, 54, 20, 43], we have focused our attention on this metal.

Our ability to conduct simulations of rather large problem sizes avoids the need of using periodic boundary conditions which limits the analysis to a representative volume element. Displacement-controlled tensile test conditions are simulated by constraining the mesh nodes at the bottom face of the specimen, whereas specified displacements are applied to the nodes at the top of the specimen.

3.2 Model calibration

As mentioned in Chapter 2, plastic deformation inside the grains can be neglected under moderate loading conditions. Furthermore, it is found that the elastic anisotropy of the grains does not significantly affect the macroscopic yield behavior of the nanocrystalline sample, thus the grain interiors are assumed to follow an isotropic

large deformation neohookean elastic law with Young's modulus $E = 108 \times 10^9 Pa$ and Poisson's ratio $\nu = 0.3$. The properties of the grain boundary model are calibrated against experimental and atomistic results as described below. One of the main issues that needs to be confronted towards this end is the significant discrepancies in yield stress values between experiments and atomistic models [14, 17, 10, 53, 54, 20, 43]. These discrepancies have been attributed to the idealized polycrystalline configurations of the simulated samples including the lack of porosity and other defects, as well as to the unrealistic physics involved which either considers extremely high strain-rates (Molecular Dynamics) or outright ignores thermally activated processes (Molecular Statics). It should be noted that Molecular Dynamics simulations under extreme rates ($5 \times 10^8 s^{-1}$) and Molecular Statics simulations are in relative good agreement in general (cf. for example [17] and [53]).

In this work, we attempt to fit representative atomistic and experimental results with a single set of constitutive parameters. The elastic properties for bulk polycrystalline copper were adopted for the grain boundary model and the yield, hardening and rate dependence parameters were adjusted until good agreement with both the atomistic and the experiment stress-strain reference curves was found.

The stress-strain curve corresponding to atomistic simulation of Schiøtz *et al.* [14, 17] of nanocrystalline copper with $6.56nm$ mean grain size is used as a reference for model calibration at high strain rates, as shown in Figure 3-2. A tensile test simulation on a cubic-shape sample of $20nm$ per side with 91 grains and grain size $d = 6.67nm$ (3x3x3) was conducted at the same strain rate of $5 \times 10^8 s^{-1}$ used in [17, 20]. The comparison between the two stress-strain curves is shown in Figure 3-2.

The calibration of the quasi-static response of the model was extracted from the experimental results of Sanders *et al.* [40, 41, 55]. These experiments consist of quasi-static tensile tests on nanocrystalline copper specimens obtained by inert-gas condensation and warm compaction. The experimental stress-strain curve corresponding to grain size $d = 26nm$ [40] was used for calibration. The simulation was conducted using 66 grains of size $d = 25nm$ (4x4x1 designation) and under quasi-static conditions. Figure 3-3 shows the comparison between the stress-strain curve obtained

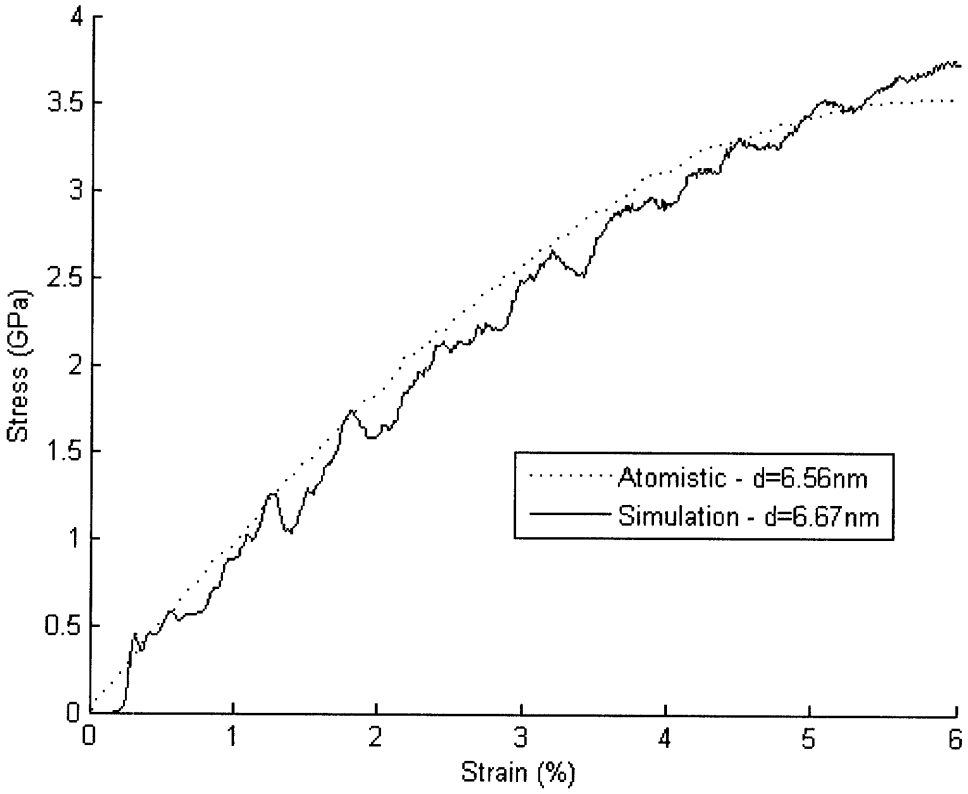

Figure 3-2: Calibration of grain boundary model parameters against atomistic results from [17] for grain size $d \approx 6.6nm$ and strain-rate $5 \times 10^8 s^{-1}$

numerically and the experiment.

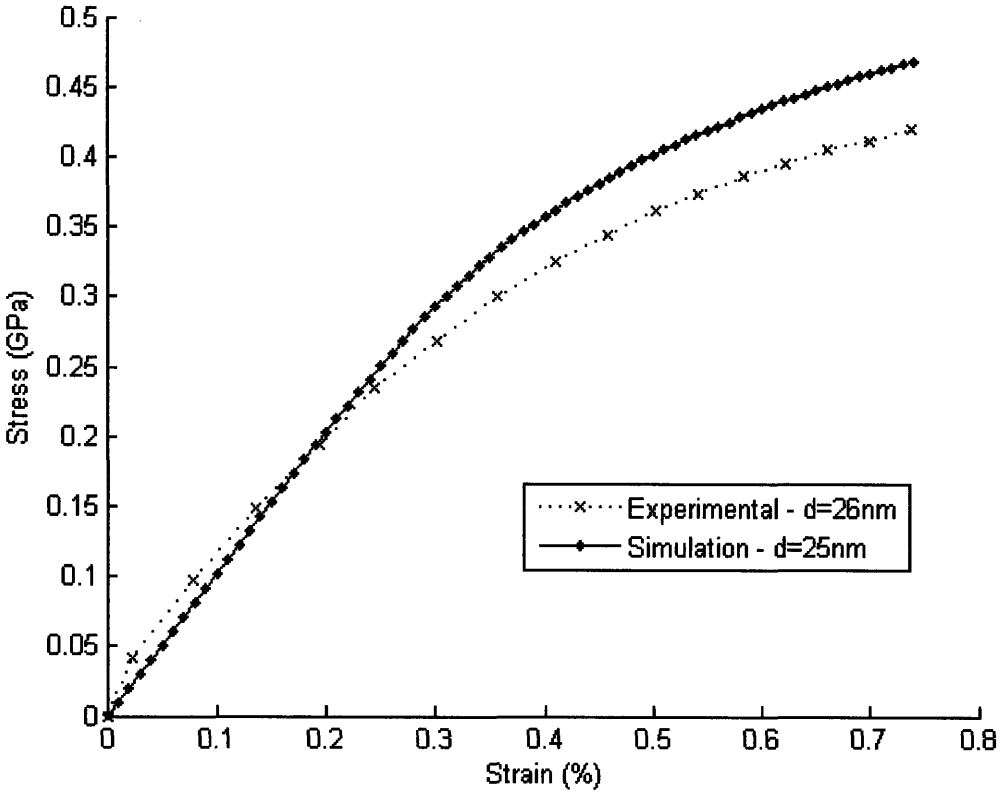

Figure 3-3: Calibration of grain boundary model parameters against experimental results from [40] for grain size $d \approx 25nm$

The final set of model constitutive parameters calibrated to both reference curves is presented in Table 3.1. Considering that a single set of model parameters is used in both simulations, the agreement with the experiment and the atomistic simulation is found to be reasonable.

3.3 Grain size dependence

The calibrated model was then used to investigate the dependence of the stress-strain response on the grain size. In order to compare with the size dependence results obtained from atomistic models in [14], a set of tensile test simulations was conducted keeping the sample size fixed at $20nm$ and systematically increasing the number of

Table 3.1: Simulation and Model parameters after calibration for Cu grain boundaries

Young's modulus (Pa)	108.0e+09
Poisson's ratio	0.33 / 0 (sliding / opening)
σ_0 (Pa)	200.0e+06
ϵ_0	1.0e-04
$\dot{\epsilon_0}$ (s^{-1})	1.0
1/n	10
1/m	10 (rate dependent)
h (nm)	1

grains from 22 (2x2x1 designation) to 97 (5x5x1 designation). This corresponds to grain sizes in the range $10nm$-$4nm$. In all the simulations, the grain boundary thickness was kept at $h = 1nm$.

The resulting stress-strain curves are shown in Figure 3-4. Owing to the extremely high strain-rate ($5 \times 10^8 s^{-1}$) used in these simulations, significant dynamic oscillations are observed in the stress-strain curves. This makes it difficult to identify a well-defined yield stress. For comparison purposes, we conventionally extract points on the stress-strain curves that would elastically unload to 2% permanent deformation. Similar approaches for identifying yield points in nanocrystalline metals have been adopted in [56, 57]. The extracted conventional values of "yield" stress are plotted on a Hall-Petch plot (σ_y vs $d^{-1/2}$) and compared with the atomistic results in Figure 3-6.

A similar approach has been followed for comparing model predictions of the size dependence of the yield stress under quasi-static loading with the experimental results in [40, 41]. In this case, the sample size was $100nm$ and three different simulations with grain sizes $d = 20nm$, $d = 25nm$ and $d = 33.3nm$, corresponding to designations 5x5x1, 4x4x1 and 3x3x1 respectively, were conducted. The same grain boundary thickness $h = 1nm$ as in the high strain-rate simulations was adopted. The resulting stress-strain curves are shown in Figure 3-5. It can be observed in this figure that the same softening tendency with the reduction of the grain size is obtained. Under quasi-static conditions, the stress-strain curves do not exhibit oscillations and a con-

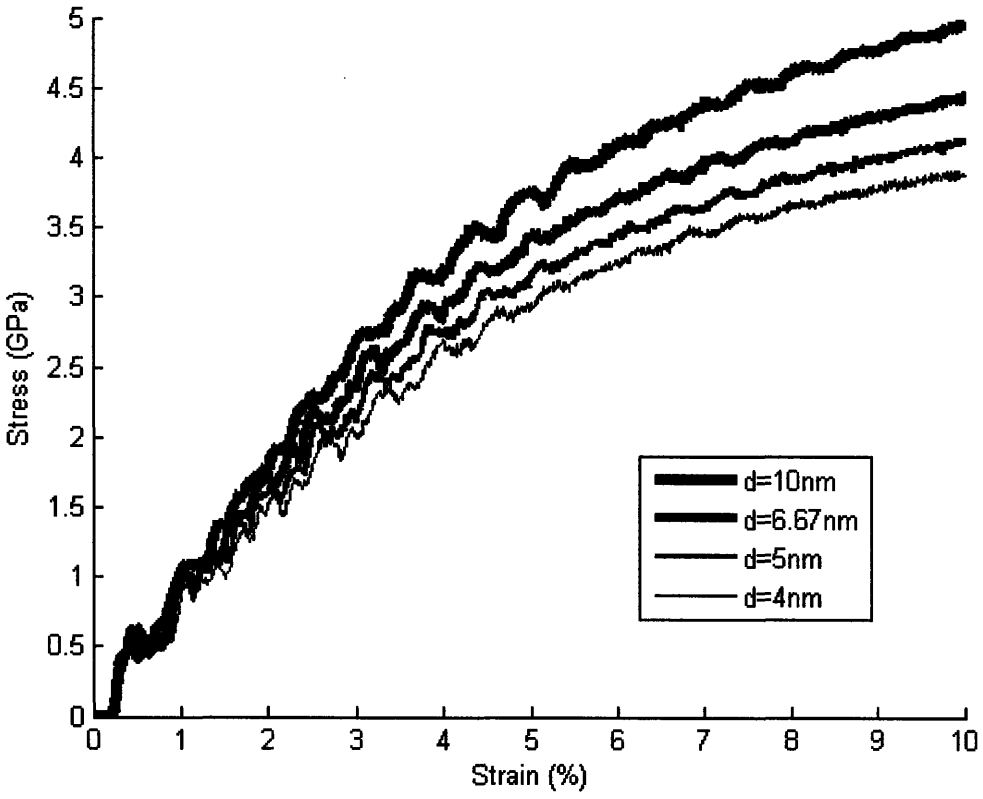

Figure 3-4: Tensile dynamic simulations of a 20nm plate for d=10, 6.67, 5 and 4nm

ventional yield stress at a 0.2% offset permanent strain may be defined. The extracted yield stress values as well as the experimental results reproduced from [40, 41] were added to the Hall-Petch plot in Figure 3-6, showing a reasonable agreement between simulations and experiments. This suggests that the vast discrepancy in the yield stress of nanocrystalline metals between experiments and atomistic simulations may be at least partially explained by rate dependence effects. However, it should also be emphasized that the proposed model overplays the role of rate dependence, as other potentially important sources of discrepancy owing to the idealizations of atomistic models are ignored.

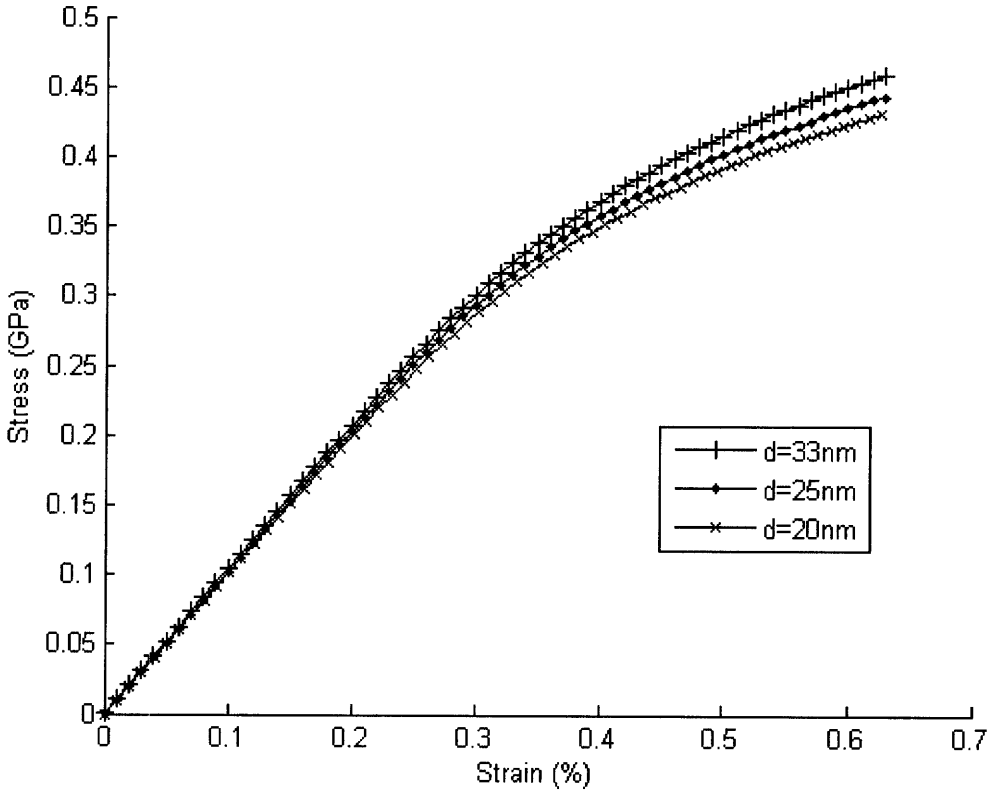

Figure 3-5: Tensile static simulations of a 100nm plate for d=33, 25 and 20nm

The previous simulations exercise the developed model under a wide range of grain sizes and for loading rates in the MD and the experimental range. In both cases, the model predicts a decrease of the yield stress with grain size, due to the

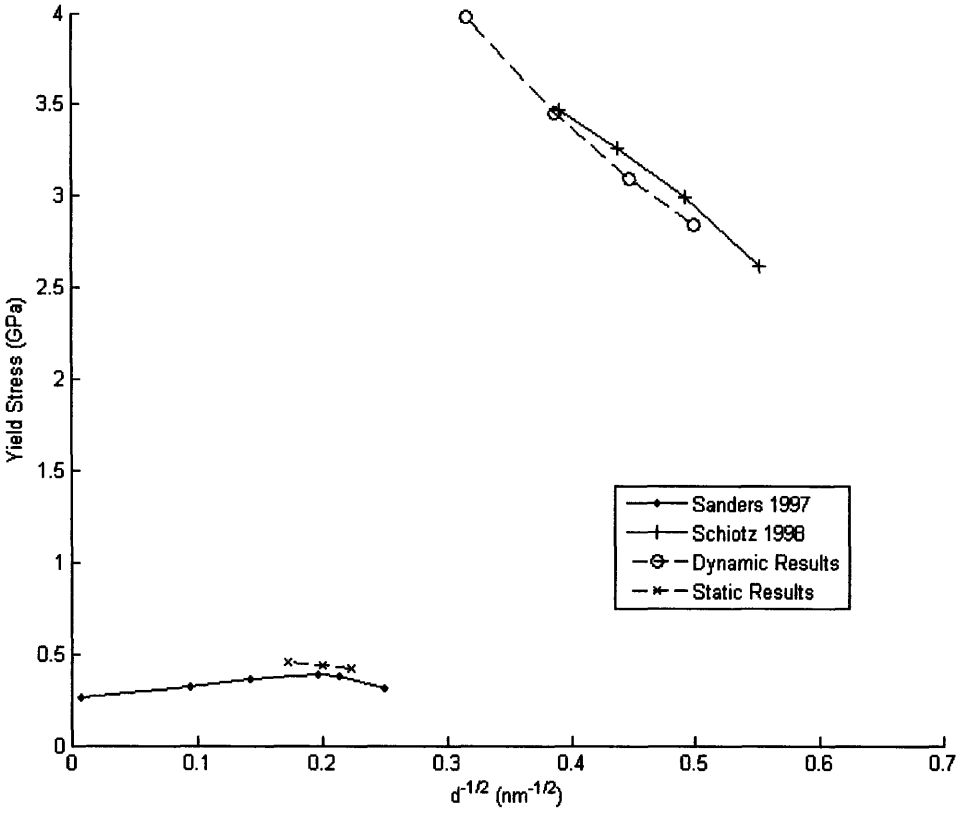

Figure 3-6: Hall-Petch plot of our two sets of simulations and of the corresponding atomistic and experimental results[41, 14]

increased presence of grain boundaries, in agreement with atomistic and experimental descriptions. In addition, the dependence of the yield stress on the grain size follows a reverse Hall-Petch relation with a similar slope k obtained by atomistic simulation, see Equation (1.1).

3.4 Summary

The proposed phenomenological model describes the onset of yield in the deformation of nanocrystals. Given that the grains are assumed elastic, all the plastic deformation can only be attributed to intercrystalline grain boundary mediated deformations. These mechanisms appear to provide an adequate continuum description of experimental observations and atomistic predictions. Our continuum model is consistent with the hypothesis that grain boundary kinematic mechanisms of sliding and accommodation are responsible for the softening of nanocrystals with decreasing grain sizes.

The continuum model also predicts a decrease of the yield stress with the grain sizes. Furthermore, the dependence of the yield stress on the grain size is found to follow the reverse Hall-Petch effect, which is consistent with atomistic characterizations [14] and experiments [40].

A single set of model parameters is able to fit both the high strain-rate and quasi-static response. This suggests that the significant discrepancy between the experimentally observed strength of nanocrystalline copper and atomistic model predictions may be partially due to loading-rate effects.

It is also important to highlight that the continuum modeling approach does not suffer from the time step limitations which mire MD and, thus, enables the consideration of a vast range of loading rates including static loads. The continuum modeling approach proposed here can be taken as a basis for the development of multiscale models of grain boundary mechanisms of deformation and failure based on atomistic characterizations of grain boundary properties and their dependence on microstructural parameters (*e.g.* grain boundary misorientation).

Chapter 4

Continuum modeling of shock response in nanocrystals

This chapter is devoted to the modeling of the shock response in nanocrystals. To this end, atomistic simulations of shocks in metal are used as a reference for the identification and characterization of the competitive grain bulk and grain boundary deformation mechanisms under such conditions.

The response of nanocrystalline metals to intense compressive loads such as produced by shock loadings has thus far only been investigated via atomistic simulations and very few experimental efforts [23, 58]. The main finding has been an unprecedented compressive strength (up to $15GPa$), which has been rationalized by the suppression of grain boundary dissipation mechanisms under strong state of compression, leading to a decrease of grain boundary sliding and an increase of intragrain dislocation activity. These observations suggest frictional mechanisms at the grain boundary in which the sliding is strongly affected by the state of compression whereas the intragrain dislocation nucleation barrier is not as severely affected by the pressure. Intragrain dislocation emission then becomes the only way of accommodating the deformation.

Other conclusions of the work in [23] include a shift of the threshold between direct and inverse Hall-Petch effect to a smaller grain size and higher strengths which is also supported by a simple qualitative model, see Figure 4-1.

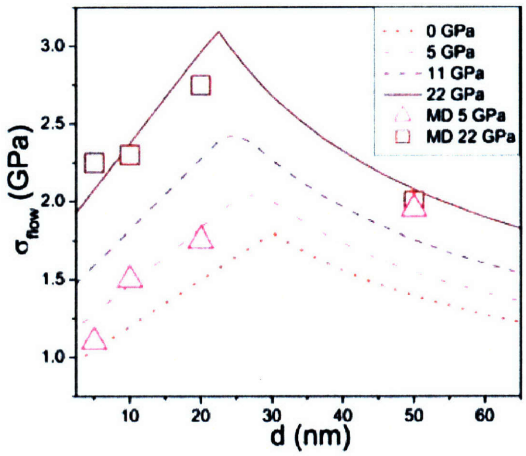

Figure 4-1: Flow stress versus grain size as predicted by Bringa *et al.*'s model and MD results [23]

The frictional behavior of grain boundaries has also been observed in recent work by Schuh and coworkers [59, 22] who used Molecular Statics simulations to show an asymmetry between the compression and tension strength of nanocrystalline nickel (cf. Figure 4-2). This asymmetry has been partially explained by the observation that the grain boundary in nanocrystals tends to have a glass-like behavior but exhibiting shear bands confined to very small scales ($\sim 1nm$) [19, 22]. In [23, 22], a Mohr-Coulomb friction model was suggested as a means to describe the behavior of the grain boundary under compression.

These deformation features specific to the nanoscale are very strongly dependent on the grain size. At the micron and larger scales, the deformation is purely symmetric and the deformation is driven entirely by intragrain plasticity. Between approximatively $1\mu m$ and $10nm$, the tension-compression asymmetry appears and increases [19, 22]. Finally, below $10nm$, the asymmetry decreases and the deformation is mainly due to grain boundary deformation. Ultimately, for ultra-small grains, the nanocrystalline asymmetry is thought to be equivalent to the one observed in amorphous metal.

In this thesis, we endeavor to extend the continuum modeling framework for nanocrystalline metals to the range of shock loading response. The extensions in-

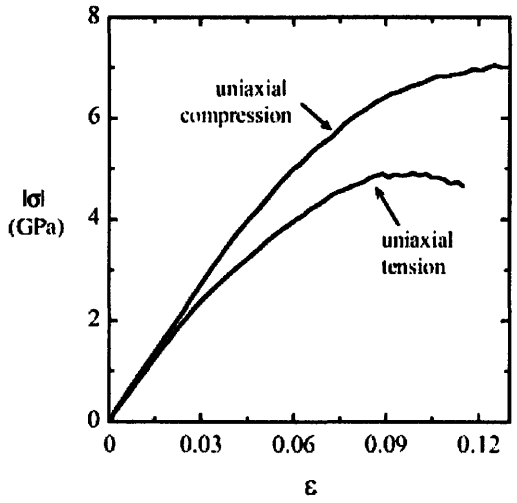

Figure 4-2: Strength asymmetry on a cubic Ni $4nm$ grain size specimen in Lund *et al.*'s simulations [22]

volve the modification of the grain boundary sliding and accommodation model to account for the pressure-dependent frictional resistance of the grain boundary, the implementation of a high-rate equation of state (EOS), shock-capturing scheme to describe the volumetric response of the grain interiors under shock loading and a plasticity model to describe their deviatoric response. The model parameters are calibrated to fit the elastic and plastic waves obtained by atomistic simulation in [23]. The calibrated model is then used to investigate the influence of grain boundary friction.

4.1 Grain boundary friction model

In order to account for the frictional response of grain boundaries to sliding under compressive loading suggested by atomistic simulations, we modify the sliding resistance of the grain boundary model in Equations (2.24) and (2.25) with a pressure-dependent frictional term [31]:

$$\tilde{\sigma}_0(\bar{\epsilon}_p) = \sigma_0 \left(1 + \frac{\bar{\epsilon}_p}{\epsilon_0}\right)^n + \mu \ \mathbf{Max}(0, -\sigma_n) \tag{4.1}$$

where μ is the friction coefficient and σ_n, the normal component of the stress at the grain boundary. In the rate-independent limit with no hardening, Equation (2.25) becomes in the case of compression: $Y = \sigma_0 - \mu\sigma_n$, which is consistent with the model proposed in [22] but applied at the level of the grain boundary instead of the effective response.

Previous studies on metallic glasses by Lund and Schuh [60, 61, 62] have shown that a Mohr-Coulomb model with a friction coefficient of $\mu = 0.12$ provides a good fit of the asymmetric yield surfaces of metallic glasses. In our model, we adopt this value ($\mu = 0.12$) for the friction coefficient of the grain boundary based on the expectation that nanocrystals will tend toward the response of a metallic glass in the amorphous limit.

Except for the modification of the grain boundary resistance sliding, Equation (4.1), the grain boundary model of Chapter 2 is used.

4.2 Model for the grain bulk response under shock loading

4.2.1 Equation of state

Shock Hugoniot

The shock response of many metallic materials is well described by the Hugoniot relation between the shock velocity U_s and the material velocity U_p of the simple form [63, 64, 65]:

$$U_s = C_0 + sU_p \tag{4.2}$$

In this expression, C_0 and s are material parameters which can be obtained from experiments. Values of these parameters for many metals have been published [63, 64, 65].

By considering conservation of mass and momentum in a control volume at the shock front, and Equation (4.2), the final pressure can be calculated explicitly as a

function of the Jacobian behind the shock front J_H and the reference density ahead of the shock ρ_0 [63, 64, 65]:

$$P_H = \frac{\rho_0 C_0^2 (1 - J_H)}{[1 - s(1 - J_H)]^2} \tag{4.3}$$

where J_H is related to the density ρ_H, the specific volume V_H or the deformation tensor $\mathbf{F}_H$, defined behind the shock front, by:

$$J_H = \frac{\rho_0}{\rho_H} = \frac{V_H}{V_0} = det(\mathbf{F}_H) \tag{4.4}$$

The relation (4.3), also called the "shock Hugoniot", relates any final state of density to its corresponding pressure. The deformation path taken by the material between the initial state (P_0, V_0) and the final state (P_H, V_H) is then defined by a straight line in the (P, V) plot: the Rayleigh line [64].

Mie-Grüneisen EOS

The shock response of material deformation can also be described theoretically—as opposed to the empirical Hugoniot approach—by recourse to the Mie-Grüneisen EOS. This relation can be derived from quantum statistical mechanics of a large system of coupled harmonic oscillators as well as from purely thermodynamic considerations [66]. It relates the jump of pressure P to the jump of internal energy E with respect to the Hugoniot final state [64]:

$$P - P_H = \frac{\gamma}{V}(E - E_H) \tag{4.5}$$

where V is the specific volume and where γ, defined as the Grüneisen constant, verifies [64]:

$$\frac{\gamma}{V} = \frac{\gamma_0}{V_0} = cte \tag{4.6}$$

where γ_0 is the Grüneisen constant at the initial state.

Temperature rise

The temperature rise behind the shock follows from the energy equation [64]:

$$C_v \left(\frac{dT}{dV}\right)_H + \rho_0 \gamma_0 T C_v = \frac{1}{2\rho_0} \left(\frac{dP}{dV}\right)_H (1 - J) + \frac{P + P_0}{2} \tag{4.7}$$

where use has been made of the Mie-Grüneisen EOS and the Hugoniot relation, and where C_v is the heat capacity at zero pressure. $\left(\frac{dP}{dV}\right)_H$ follows from Equation (4.3) as:

$$\left(\frac{dP}{dV}\right)_H = -\rho_0^2 C_0^2 \frac{1 + s(1 - J_H)}{(1 - s(1 - J_H))^3} \tag{4.8}$$

Temperature changes due to plastic deformation will be considered in Section 4.2.2.

By direct integration of T, the temperature rise ΔT_{EOS} during a time step Δt can be calculated numerically for a given Jacobian increment $\Delta J = \Delta V / V_0$.

Pressure approximation

We have seen that the correct description of a shock from an initial state to a final state should follow the Rayleigh line [63, 64, 65]. Because of the local nature of the finite element approach—where an element at the shock front cannot "know" P_H in advance—the following approximation is then usually done to just follow the Hugoniot. One of the implications of this is a smoothing of the shock front but without affecting the jump condition.

4.2.2 Intragrain plasticity

Plastic deformation inside the grain is described by an isotropic model of large deformation plasticity based on the variational framework in [39]. More detailed descriptions accounting for the anisotropic plastic response based on crystal plasticity models are possible [67]. However, due to the lack of model parameters, such as slip plane resistance, hardening and rate dependence, under shock conditions, these effects are ignored as a first approximation.

A pseudo-potential of dissipation [39, 48] of the form:

$$\Psi_B^* = \sigma_0^B \frac{\dot{\epsilon}_0^B}{1+1/m^B} \left(1 + \frac{\dot{\bar{\epsilon}}_p}{\dot{\epsilon}_0^B}\right)^{1+1/m^B} - \sigma_0^B \dot{\epsilon}_p^B \tag{4.9}$$

is adopted from which the isotropic rate and temperature dependent hardening law

$$\sigma_y^B = \sigma_0^B \left(1 + \frac{\bar{\epsilon}_p^B}{\epsilon_0^B}\right)^{1/n^B} \left(1 + \frac{\dot{\bar{\epsilon}}_p^B}{\dot{\epsilon}_0^B}\right)^{1/m^B} \left(1 - \frac{T}{T_m}\right)^{\eta_T} \tag{4.10}$$

follows, where σ_y^B, ϵ_p^B and T are respectively the yield stress, the equivalent plastic strain and the temperature, and where ϵ_0^B, n^B, $\dot{\epsilon}_0^B$, m^B, T_m and η_T are model parameters representing respectively the reference plastic strain, the hardening exponent, the reference plastic strain rate, the rate dependence exponent, the melting temperature and the thermal softening exponent. In these expressions, the superscript "B" refers to grain bulk values as opposed to the grain boundary parameters.

In this model, we consider the influence of temperature on the yield stress—cf. Equation (4.10)—as well as the heating produced by plastic deformation. This plastic dissipation contributes to the increase of temperature given by the EOS ΔT_{EOS} by:

$$\Delta T_{\text{plastic}} = \frac{\beta_{TQ} \Psi_B^* \Delta t}{\rho_0 C_p} \tag{4.11}$$

where β_{TQ}, Δt and C_p are the Taylor-Quinney coefficient, the time step increment and the heat capacity at constant pressure. The final increase of temperature is then calculated by summing the two contributions.

In order to account for the influence of the high pressure loads produced by the shock on temperatures, a linear dependence is assumed [68]:

$$T_m = T_{m_0} + T_{m,p} P \tag{4.12}$$

where T_{m_0} is the melting temperature at ambient pressure and where $T_{m,p}$ is the slope of the melting curve, assumed constant [68].

The present model ignores the contributions of entropy changes in the plastic response of the grains. It is known that the isentropic assumption is reasonable for material subjected to mild loading conditions [69, 70]. Appendix A provides an analysis based on the work of Clifton justifying this assumption for the range of shock pressure considered in this thesis [69].

4.3 Simulation setup

The computational framework for modeling the response of nanocrystalline metals described above is employed for investigating the influence of grain boundary friction on copper nanocrystalline deformation under shock loading conditions. To this end, we model a 120nm×80nm×80nm nanocrystalline copper sample with 20nm grain size (same as in [23]) subjected to shock loading conditions. These are applied as displacement boundary conditions representing a piston velocity $U_p = 1000m/s$.

Idealized grain morphologies resulting from the three dimensional packing of Wigner-Seitz cells corresponding to body centered cubic lattices are adopted for simplicity as building blocks of nanocrystalline samples. 6×4×4=96 of these macrocells result in a microstructure consisting of 271 equiaxed grains or portions of grain. Each full grain is discretized using 1,536 second-order tetrahedral finite elements in a manner that leaves the overall polycrystal mesh conforming at the grain boundaries—note that this is eight times more tetrahedra per grain than was used in Chapter 3. Subsequently, interface elements are added at the boundaries between grains, taking advantage of the conformity of the existing mesh. The simulations are done with a total of 294,912 bulk elements and 26,624 interface elements and run on 24 processors. Figure 4-3 shows the grain structure and finite element mesh.

The denomination of "shock pressure" for the axial stress will be used following Bringa *et al.* [23], referring to "pressure" for the third of the trace of the stress tensor.

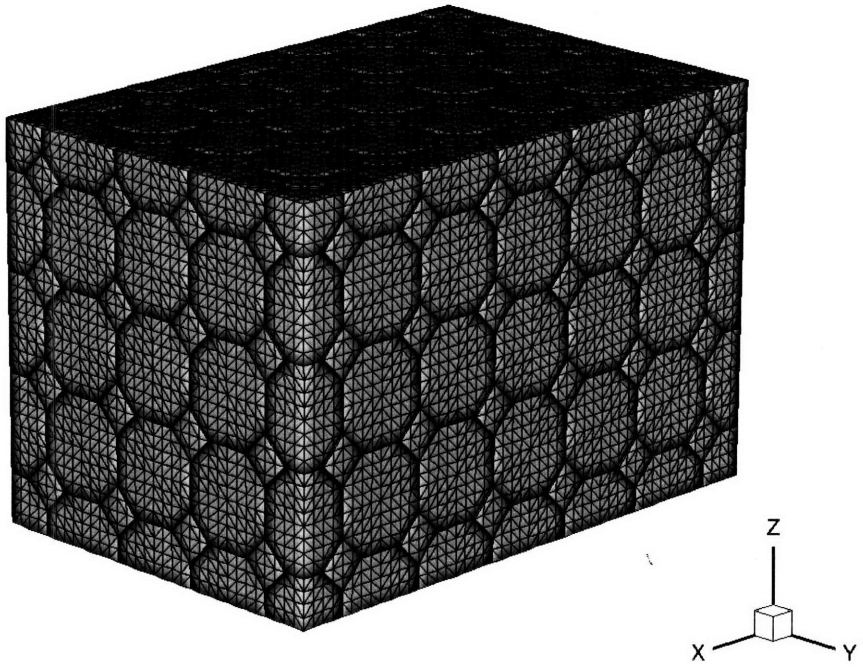

Figure 4-3: 6x4x4 mesh used in the shock simulations; the heavy lines denote the grain boundaries between the tetrakaidecahedra

4.3.1 Artificial viscosity

Originally proposed by Von Neumann and Richtmyer [71], the artificial viscosity aims at spreading the shock front over several elements in order to enable the simulations of strong shocks of thickness smaller than the mesh size. The viscosity introduced in the calculations vanishes when the mesh size decreases and conserves the fundamental features of the shock, such as the shock speed or the jump conditions, while avoiding the high frequency spurious mode otherwise observed.

Based on Von Neumann and Richtmyer's work [71], Lew *et al.* [72] proposed a specific deviatoric Lagrangian artificial viscosity scheme for unstructured mesh and high-order elements. This scheme allows the consideration of large plastic deformation as it is observed in the case of shock loading conditions, and, by spreading the shock over 4 to 6 elements, avoids unwanted oscillations while providing stable solutions for mesh size larger than the shock width [72].

We adopt here this scheme, in which the corresponding artificial viscosity is defined

as follows [72]:

$$\eta = \begin{cases} \max(0, -\frac{3}{4} h_{\text{elt}} \rho (c_1 \Delta u - c_L a), & \Delta u < 0; \\ 0, & \Delta u \geq 0. \end{cases} \tag{4.13}$$

where h_{elt}, Δu and a are respectively the element size, the velocity jump across the element and the sound speed of the material, and where c_1 and c_L are two model parameters. Note that the mass density ρ for a given Jacobian J and an initial density ρ_0 is simply equal to $\frac{\rho_0}{J}$. c_1 and c_L are chosen such that an adequate balance between a minimum diffusion of the shock wave and a maximum attenuation of the oscillations is reached.

4.3.2 Calibration of model parameters

The calibration of the grain bulk model parameters was done by considering the shock response of a homogeneous material sample. To this end, the mesh configuration in Figure 4-3 was used to conduct shock simulations under the conditions in [23].

The parameters for the Mie-Grüneisen/Hugoniot EOS were taken directly from published properties for bulk polycrystalline copper [65]:

$$\begin{cases} C_0 = 3910 m/s \\ s = 1.51 \\ \gamma_0 = 1.96 \end{cases} \tag{4.14}$$

The volumetric response, represented by the longitudinal pressure profile, predicted by our model after $10ps$ of simulation and the corresponding MD prediction are shown on Figure 4-4.

It can be seen in this figure that the MD simulation predicts a shock propagation speed that is faster than the prediction of the continuum model. The shock propagation speed can be matched to the atomistic model by increasing C_0 to a value of $C_0 = 4841 m/s$, see Figure 4-4. However, that necessarily affects the value of the pressure behind the shock as the pressure is directly proportional to the shock

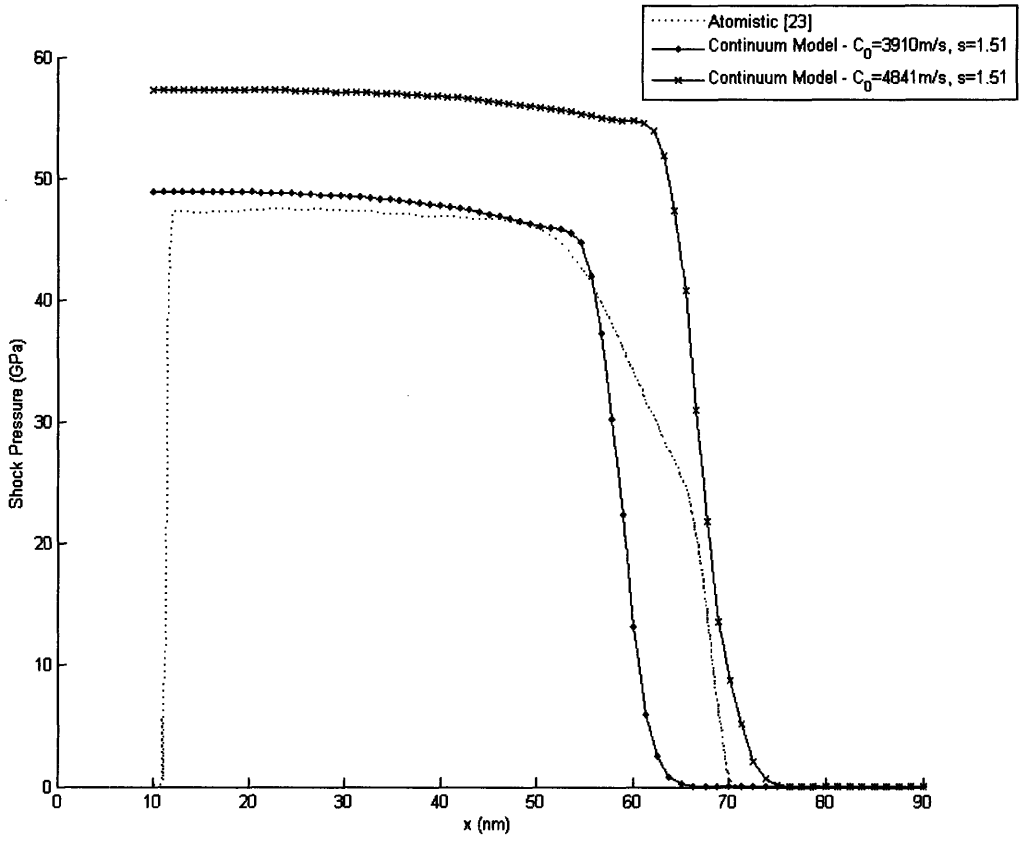

Figure 4-4: Shock pressure distribution after 10ps of simulation for two different values of $C_0 = 3910m/s$ and $C_0 = 4841m/s$; comparison with atomistic simulation [23]

speed for a given piston velocity: $P_H = \rho_0 U_s U_p$. This observation that the Mie-Grüneisen/Hugoniot EOS can either match the speed of propagation of the shock or the pressure behind the shock is indicative of a deficiency of the model to describe shock response in nanocrystals. A more accurate description may require the consideration of higher order terms in the expansion of the pressure.

The remaining deviatoric parameters were then adjusted until a good agreement with the deviatoric response predicted using MD and represented by the longitudinal profile of the Von Mises stress after $10ps$ was obtained, see Figure 4-5.

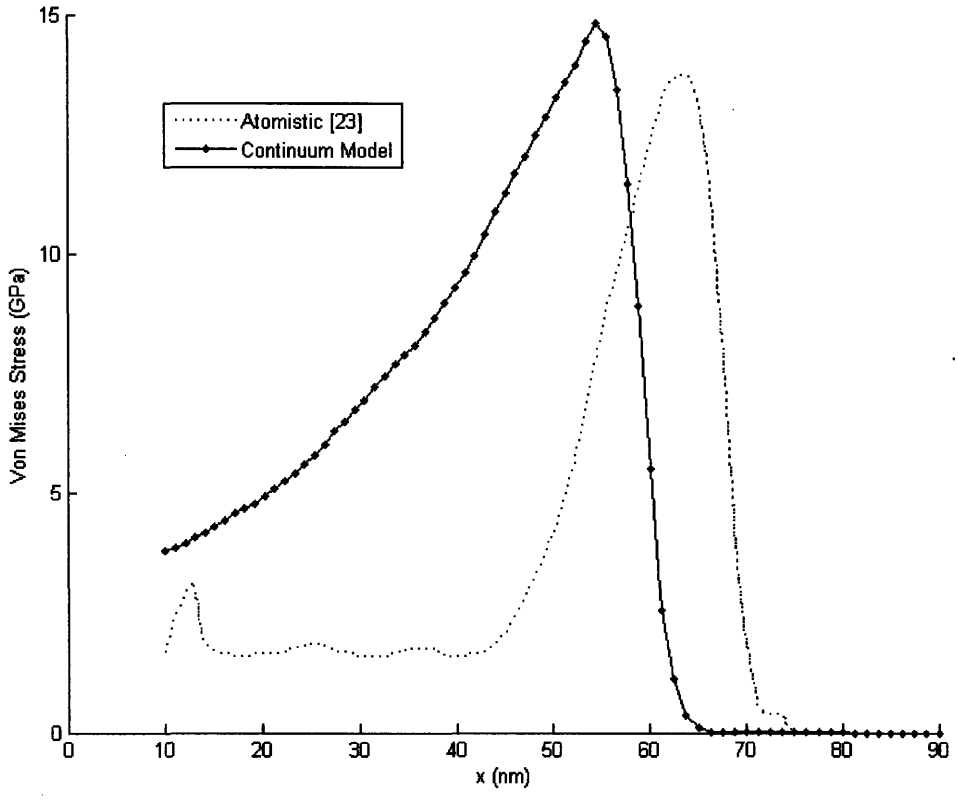

Figure 4-5: Comparison of Von Mises stress distribution after $10ps$ between continuum model and atomistic simulations [23]

The deviatoric response is characterized by a sudden rise of the Von Mises Stress due to the sudden increase of deformation rate at the shock front. A rapid decay, with an accompanying increase of plastic deformation, is then observed, followed finally

by a plateau, which characterizes the flow stress of the shocked material [23]. In the continuum model, the peak is controlled by the initial yield stress and the rate dependence parameters. The decay is controlled by the rate dependence parameters and the tail is controlled mainly by the initial yield stress and the hardening parameters.

It is expected that the constant value of the Von Mises stress at the tail of the shock correspond to the total shock temperature dependent value of the yield stress for an amount of hardening corresponding to the total plastic strain accumulated across the shock front. Based on the experimental observations which show a limited or negligible amount of strain hardening in nanocrystals [29], the strain hardening in the model is suppressed by choosing $1/n^B = 10,000$.

The atomistic Von Mises stress profile shows a very rapid relaxation of the Von Mises stress behind the front shock thus suggesting an unusually high rate dependence. In the continuum model, it is found that even adopting an extremely high rate dependence by choosing very low values of the rate dependence exponent is not sufficient to obtain such rapid decay in the Von Mises stress. This may be due to inadequacy of the rate dependence law or to some artifact in the MD simulations. Due to the larger width of the Von Mises profile obtained with the continuum model, a longer simulation is required to capture the remnant value of the deviatoric stress at the tail of the shock, see Figure 4-6.

Finally, the artificial viscosity parameters were fitted in order to minimize the oscillations while retaining the sharpest jump possible. The values of the parameters for the grain interior are given in Table 4.1.

The grain boundary parameters adopted in Chapter 3 with a value of the friction coefficient $\mu = 0.12$ are used in calculations, see Table 4.2.

In order to understand the accuracy of the continuum model, a mesh convergence analysis consisting of simulations with increasingly refined meshes was conducted. Three cases were considered: 192, 1,536 and 12,288 elements per grains, corresponding to a total number of elements of 36,864, 294,912 and 2,359,296, respectively. Figures 4-7 and 4-8 show the shock pressure and Von Mises stress profiles for the three cases as well as the theoretical shock position after $10ps$ calculated from Equation (4.2).

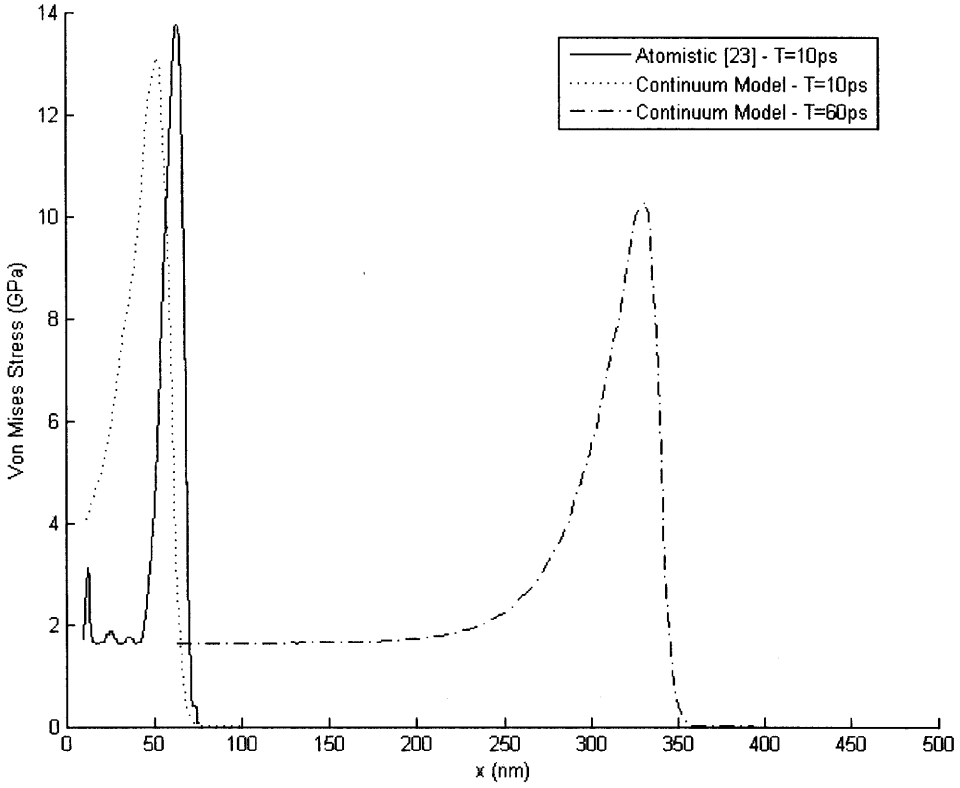

Figure 4-6: Shock simulations for longer time (60ps) than MD simulations (10ps) showing decay of Von Mises stress toward uniform value consistent with atomistic description

Table 4.1: Model parameters for Cu bulk grain

ρ_0^B	$8960 kg/m^3$
E^B	$124 \times 10^9 Pa$
ν^B	0.34
σ_0^B	$1.335 \times 10^9 Pa$
ϵ_0^B	1.
$\dot{\epsilon}_0^B$	$2.4 \times 10^9 s^{-1}$
$1/m^B$	1.
$1/n^B$	10000.
η_T	1.
T_0, ambient temperature	$298K$
T_{m_0}, melting temperature at ambient temperature	$1356K$
$T_{m,p}$, melting curve slope	$40K/GPa$
C_0, offset of the Hugoniot	$3910.0 m/s$
s, slope of the Hugoniot	1.51
γ_0, Grüneisen coefficient at T=0K	1.96
C_v, specific heat at constant volume	$385.0 J/(kgK)$
c_1, first artificial viscosity parameter	25
c_L, second artificial viscosity parameter	0.4

Table 4.2: Model parameters for Cu grain boundaries

Young's modulus	$108.0 \times 10^9 Pa$
Poisson's ratio	0.33 / 0 (sliding / opening)
σ_0	$200.0 \times 10^6 Pa$
ϵ_0	1.0×10^{-4}
$\dot{\epsilon}_0$	$1.0 s^{-1}$
$1/n$	10
$1/m$	10
h	$1nm$
μ	0.12

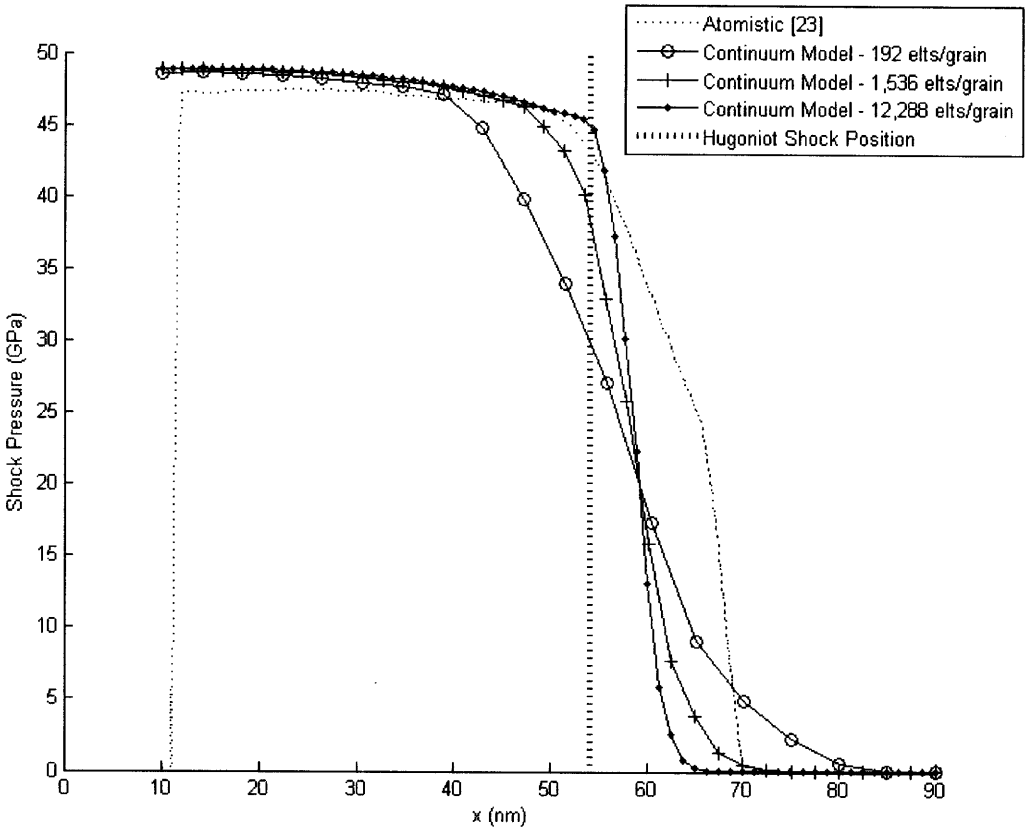

Figure 4-7: Mesh convergence study showing shock pressure distribution at 10ps for three different mesh sizes

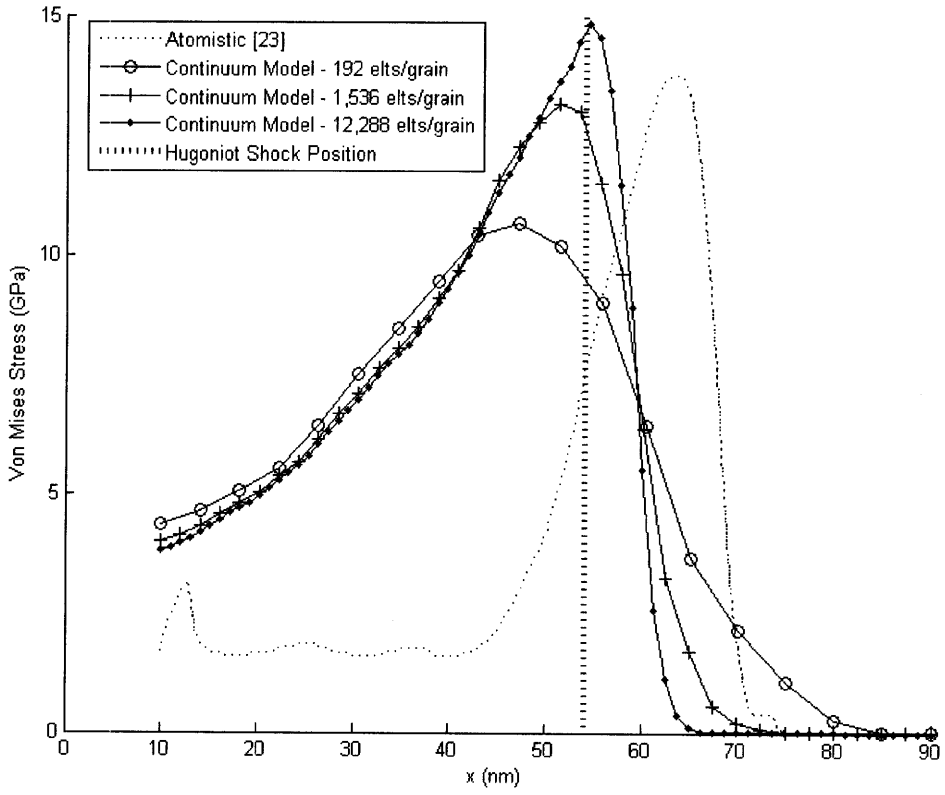

Figure 4-8: Mesh convergence study showing Von Mises stress distribution at 10ps for three different mesh sizes

In both cases, the decrease of the mesh size leads to a convergence of the shock front towards one unique sharp front. The corresponding slopes become increasingly more abrupt but the position of the shock front is conserved, independently of the mesh size. The final shock pressure is also unaffected by the mesh size as the superimposition of the tails for all meshes indicates but the Von Mises peak is subject to a sufficient refinement in order to be representative of its converged value. The observed behavior indicates a good convergence of the scheme and the intermediate mesh is chosen as a good balance between precision and calculation time.

4.4 Influence of friction on the shock response of nanocrystals

In order to study the influence of friction on the behavior of shocked nanocrystalline copper, two additional simulations incorporating the grain boundary model with and without friction were conducted.

Figure 4-9 shows a snapshot of the spatial distribution of the Von Mises stress consisting of a longitudinal slice taken in the middle of the rod for the three cases: no grain boundary sliding, grain boundary sliding without friction ($\mu = 0$) and grain boundary sliding with friction ($\mu = 0.12$). Additionally, Figures 4-10 to 4-13 show the corresponding one-dimensional longitudinal profile—taken as a line in the middle of the rod—as well as the ones for pressure, temperature and velocity distributions.

For all three simulations, the shock jump conditions including the shock propagation speed and the pressure jump were matched with good accuracy, see Figure 4-10. In particular, the shock speed and the maximum shock pressure obtained are approximatively $7nm/ps$ and $47GPa$, respectively, which are in good agreement with the atomistic simulations in [23].

In the absence of grain boundary sliding, a uniform drop of the Von Mises stress is observed behind the shock front which results from the plastic relaxation of the grains, see Figure 4-11. As discussed earlier, the drop that follows is not as strong

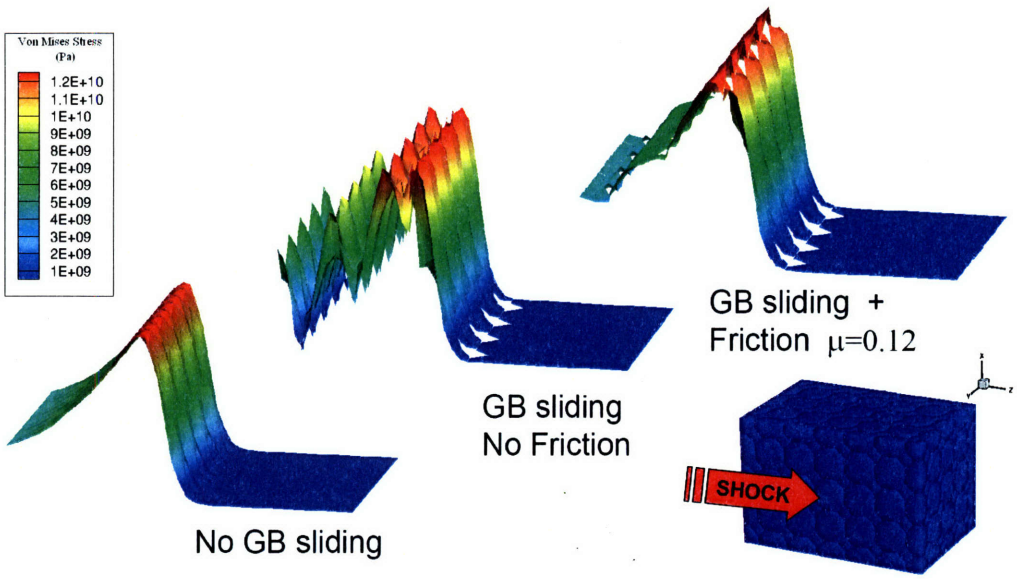

Figure 4-9: Von Mises stress for a shocked 6x4x4 model of nanocrystalline copper after $10ps$ with $U_p = 1000m/s$; plots of simulations are shown for a longitudinal slice in the middle of the rod with and without grain boundary sliding and with/without friction in the grain boundary (GB) sliding case

as in [23] and the average Von Mises stress level remains relatively high behind the front. In the second case where grain boundary sliding without friction is allowed, the overall deviatoric stress level exhibits sudden drops at the grain boundaries due to the dissipation provided by the sliding deformations. Due to the unimpeded relaxation of the grain boundaries, plasticity inside the grains occurs in much smaller amounts, which is manifested by large oscillations in the Von Mises stress profile with a spatial frequency equal to the grain size. The peak observed near the grain centers are due to wave reflections at the grain boundaries. The Von Mises stress can drop below the yield value inside the grains at the tail of the shock, thus showing the additional relaxation provided by the grain boundaries. In the third case where friction is considered, an intermediate situation is observed. Sliding dissipation is partially inhibited due to the high level of compression at the grain boundary leading to a somewhat larger stress level and a smoother distribution.

The increase in temperature observed for the case without friction is caused by the increase of plastic work due to the oscillations of the Von Mises stress, see Figure

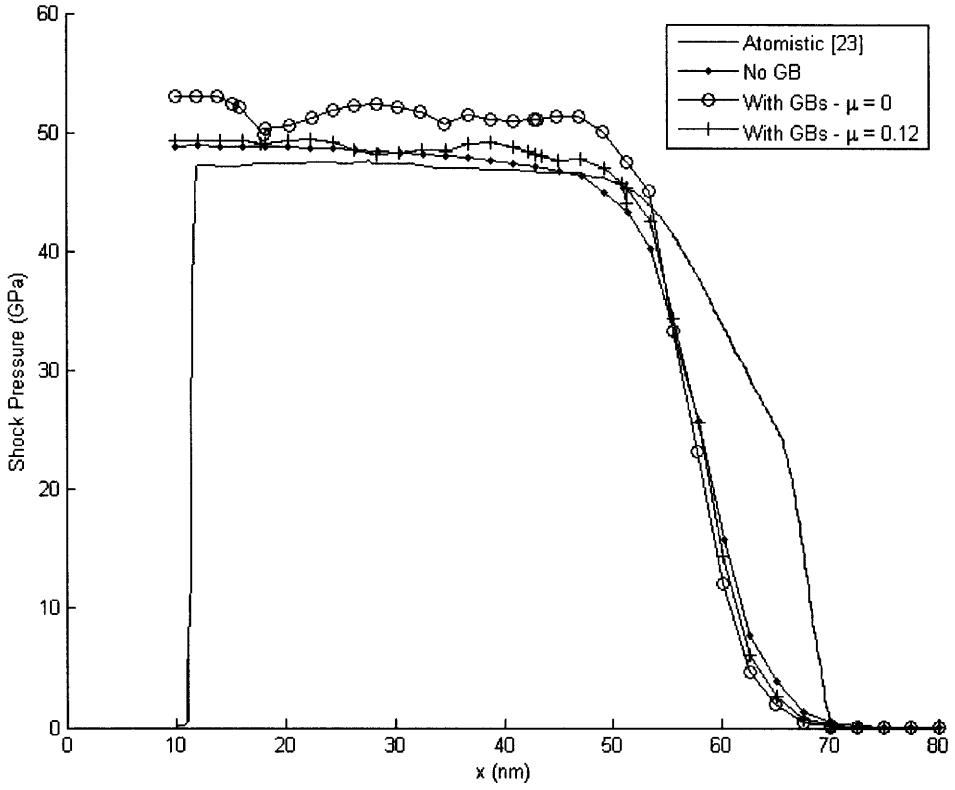

Figure 4-10: Shock pressure distribution after $10ps$; plots of simulations are shown for a longitudinal line in the middle of the rod with and without grain boundary sliding and with/without friction in the GB sliding case

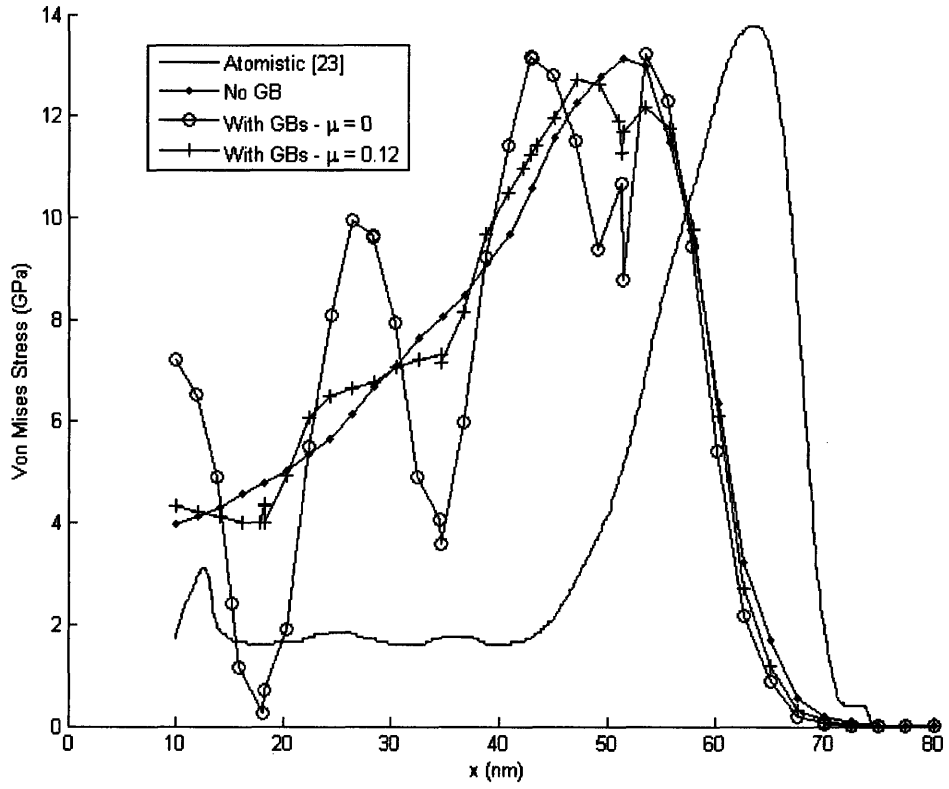

Figure 4-11: Von Mises stress distribution after $10ps$; plots of simulations are shown for a longitudinal line in the middle of the rod with and without grain boundary sliding and with/without friction in the GB sliding case

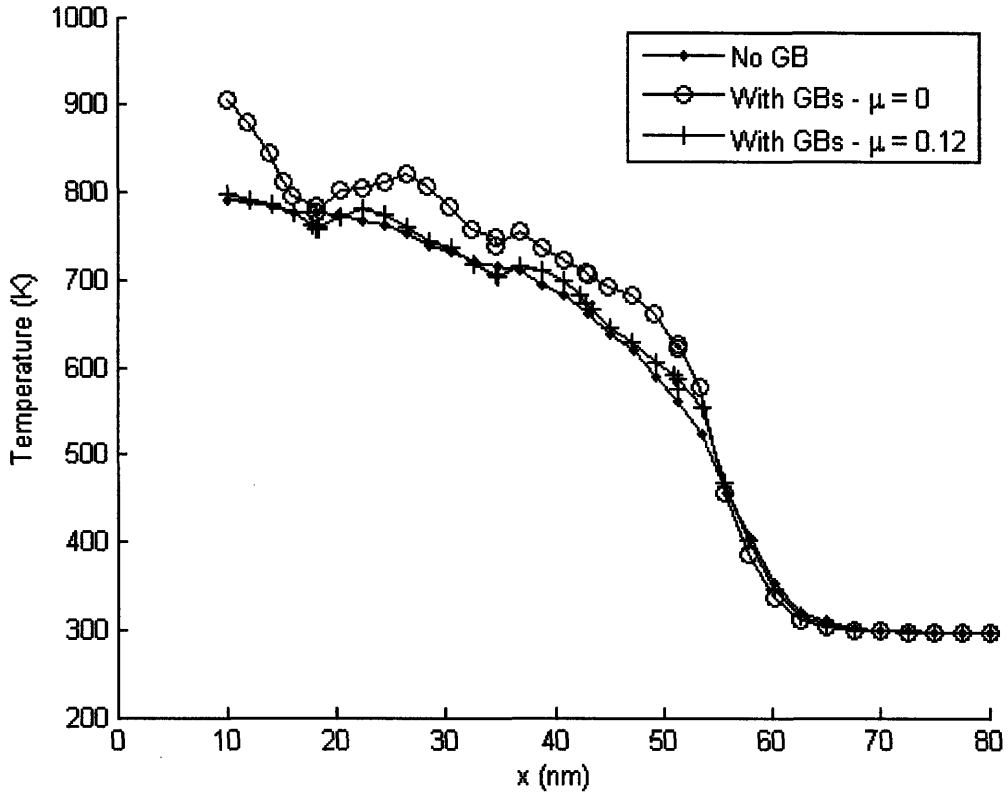

Figure 4-12: Temperature distribution after $10ps$; plots of simulations are shown for a longitudinal line in the middle of the rod with and without grain boundary sliding and with/without friction in the GB sliding case

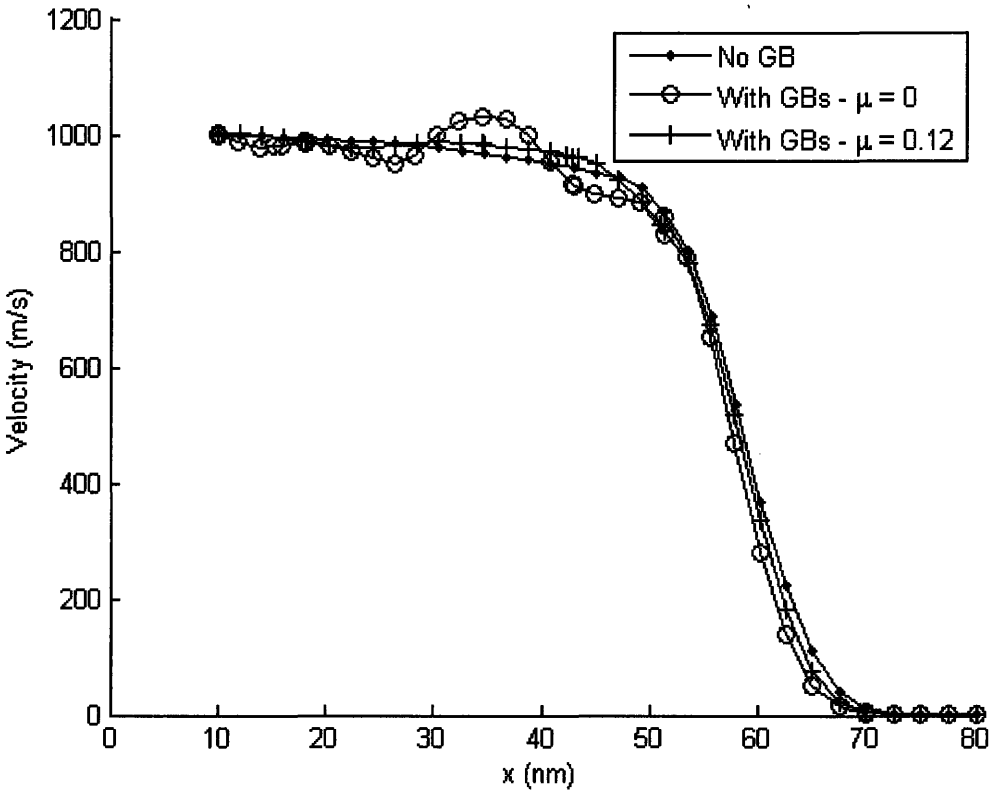

Figure 4-13: Velocity distribution after $10ps$; plots of simulations are shown for a longitudinal line in the middle of the rod with and without grain boundary sliding and with/without friction in the GB sliding case

4-12. In the case where the friction is considered, the temperature profile is ostensibly unchanged with respect to the homogeneous material, which is probably due to the neglect of the frictional heating at the grain boundary in the model.

Finally, Figure 4-13 shows the profile of material velocity obtained in the three simulations. These plots confirm the grain-scale oscillations in the shock response in the case where grain boundary sliding is unimpeded, which is maximum immediately behind the shock front and is attenuated toward the tail. The temperature and velocity profiles were not compared because the atomistic results were not provided in [23].

4.5 Conclusion

A model attempting to capture the shock response of nanocrystals by extending the model presented in Chapter 2 was developed, tested and used to investigate the influence of the frictional behavior of the grain boundary. It is found that the model parameters can be adjusted to describe the basic features of the shock response of nanocrystals obtained with atomistic simulations, including the shock speed and the shock pressure, with reasonable accuracy. However, more accurate descriptions may require an improved EOS. The parameters of the Mie-Grüneisen/Hugoniot EOS can be adjusted to obtain the shock speed or the pressure, but not both. It can finally be concluded that, under shock loading conditions, the continuum model for grain boundary requires the addition of frictional mechanisms at the grain boundary in order to avoid the non-physical oscillations otherwise observed.

Chapter 5

Continuum model of ultrafine polycrystals with embedded growth nano-twins

This chapter is devoted to the development of a continuum model of the deformation and failure response of ultrafine polycrystals embedded with growth nano-twins. As discussed in the introduction of this thesis, this type of material has elicited significant interest because they exhibit yield stresses comparable with nanocrystals without compromising the ductility.

Nanocrystalline metals resulting from normal processing conditions usually have high-angle grain boundaries. The low coherence and high energy of high-angle grain boundaries result in residual microstrains in the sample [24] and a glass-like behavior of the grain boundary [19], which is responsible for the low ductility of nanocrystals. By taking extreme care in the processing conditions so as to minimize microstrains and obtain samples with predominant low-angle boundaries, Lu *et al.* have shown that the ductility of nanocrystals can be significantly improved [24].

It is consequently of interest to design polycrystalline materials where the dislocation blocking activity of the nanocrystalline grain boundaries could be conserved while avoiding the low ductility associated to high-angle grain boundaries. Recent work based on the artificial growth of structured twins—a special kind of intragrain

coherent boundaries—in ultrafine polycrystalline grains ($d \sim 500nm$), has resulted in promising steps in this direction [26, 27, 28, 29, 73]. Figure 5-1 shows an ultrafine polycrystal with embedded growth twins. The top picture represents two twinned grains separated by a grain boundary, and the bottom picture shows the very high coherence of the twins. At such grain size, grain boundary deformation mechanisms are still not predominant and most of the deformation is due to intragrain dislocation mediated plasticity. Twin boundaries act as barriers to dislocation motion, thus providing a strengthening mechanism similar to grain boundary. However, their highly coherent structure avoids the loss of ductility characteristic of nanocrystals where the strengthening mechanism is provided by the grain boundaries.

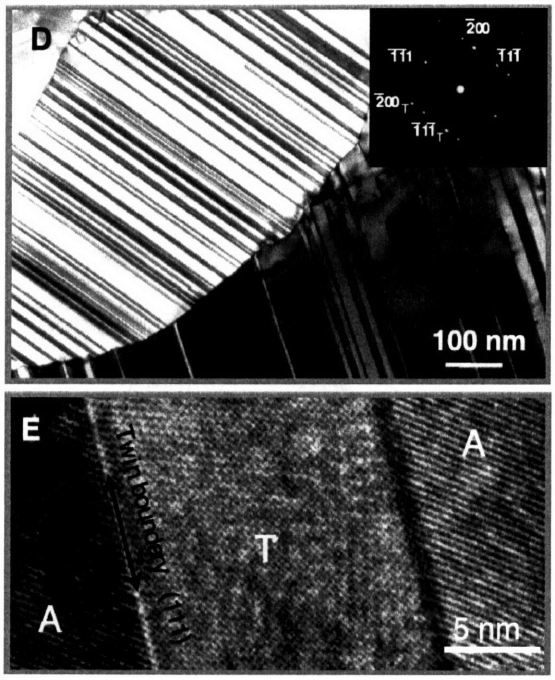

Figure 5-1: Grain boundary and twin boundaries in nano-twinned ultrafine polycrystalline Cu [26]

Frøseth and coworkers have studied the creation and evolution of growth and deformation twins for Ni, Al and Cu using atomistic models [74, 75, 76, 77]. These references suggest that the role of potential competitive mechanisms leading to the emission of partial dislocations, full dislocations or twins are still subject to debate.

For Al, there is evidence of twin migration as the preferred deformation mechanism when the twins are initially present as in the case of growth twins, whereas for Ni or Cu, extended partial dislocation nucleation appears as the predominant deformation mechanism. This is explained by the much lower energy barrier in Al (as opposed to similar energy barriers in the case of Ni and Cu) for twin migration compared to dislocation emission and twin nucleation [76, 77]. Other work by Zhu *et al.* emphasized the hardening effect due to the gradual loss of coherence of twin boundaries during pile-ups [30]. At the onset of plastic deformation, the undeformed twin boundary seems to favor absorption of external dislocations in the twin itself, followed eventually by a gradual loss of coherence and the accumulation of interfacial dislocations. This unbalance leads to an increase of both desorption and direct transfer between the two sides of the twin until a steady state is reached [30], see Figure 5-2. Even though these two mechanisms are not necessarily mutually exclusive, it is clear that further work is required to be able to assess their relative importance. Here, we adopt a phenomenological approach similar to the one proposed by Dao *et al.* [29] aimed at describing the strengthening dislocation pile-up mechanisms of twin boundaries, neglecting the mechanism of twin boundary migration.

Important aspects of deformation and failure response of ultrafine crystals with embedded nano-twins have been studied by Dao, Lu, Shen *et al.* [27, 28, 29, 73]. In these studies, they investigated the dependence of strength, ductility and strain-rate sensitivity on twin density. Among the main findings, strain-rate sensitivity, strength and ductility have been found to increase with decreasing twin spacing, as shown in Figure 5-3.

Based on the observed experimental behavior, Dao *et al.* developed a two-dimensional computational model of nano-twinned ultrafine polycrystalline copper aimed at capturing the macroscopic response [29]. In this approach, a crystal plasticity model for the bulk is used, in which slip, hardening and rate dependence are modified to account for the presence of twin boundaries which act as dislocation barriers. In addition, a fracture initiation criterion based on a maximum slip per unit twin was proposed. The model captures the strengthening and ductility increase observed with

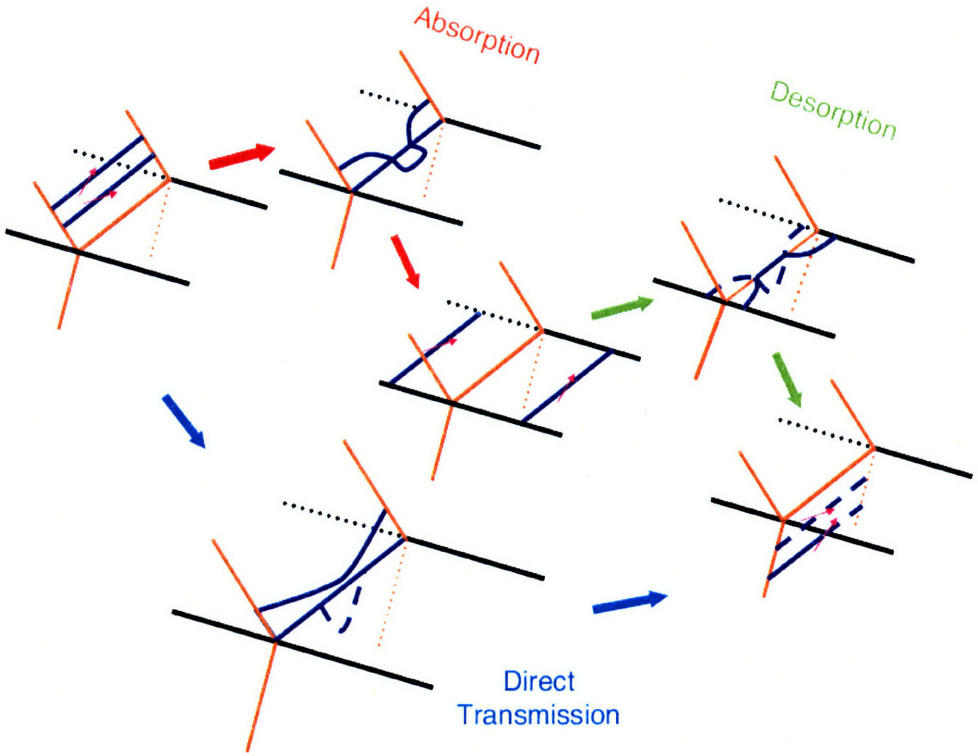

Figure 5-2: Absorption, desorption and direct transmission of a dislocation at twin boundaries as described by Zhu *et al.* [30]

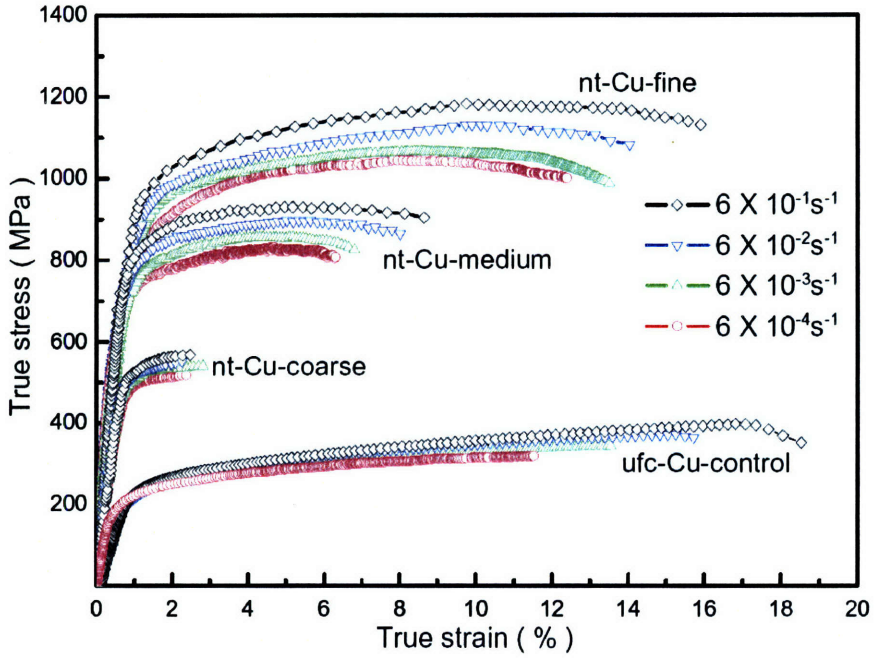

Figure 5-3: Stress-strain curves for different strain rates for ultrafine, coarse nano-twinned, medium nano-twinned and fine nano-twinned polycrystalline Cu from Dao *et al.* [29]

the decrease of twin spacing.

Notwithstanding the success of this two-dimensional model in capturing the basic role of twin boundaries inside ultrafine crystals, it is desirable to incorporate in this modeling approach kinematic mechanisms which have an inherently three-dimensional nature. This requires the consideration of the totality of slip systems pertaining to the crystalline system in question as well as the analysis of microstructures developed in all three space dimensions. This, in turn, requires large-scale simulations on parallel computers in order to compute the individual grain response as well as the grain interactions with sufficient accuracy. To this end, we propose to extend the modeling approach of Dao *et al.* [29] to three dimensions. The model consists of a finite element formulation of the continuum three dimensional problem describing the ultrafine polycrystal grains explicitly without any special modeling of the grain boundary since bulk deformation is the predominant deformation mechanism at such grain size. A crystal plasticity model is adopted for the bulk, in which the dislocation barrier action of the twinned slip systems is accounted for by modifying the critical resolved shear stress, rate dependence and hardening parameters of the slip systems piercing the twin boundaries. A fracture criterion based on maximum slip per unit twin is implemented and calibrated against experiments. The simulation results are then compared with two-dimensional results and experimental observations [29], and used to investigate the three-dimensional aspects of the dependence of the stress-strain response and ductility of ultrafine copper on twin density.

5.1 Constitutive model for single crystals with embedded twins

In this section, we describe the constitutive framework for modeling the response of the grain interiors of nano-twinned ultrafine crystals. The modeling approach is based on a constitutive framework for single crystal plasticity which is modified to account for the presence of the twin boundaries. The constitutive framework of Cuitiño and

Ortiz [78] later modified by Kuchnicki *et al.* [79] is adopted.

The total deformation of a crystal is the result of two main mechanisms: dislocation motion within the active slip systems and lattice distortion. Following Lee [80], this points to a multiplicative decomposition

$$\mathbf{F} = \mathbf{F}^e\mathbf{F}^p \tag{5.1}$$

of the deformation gradient $\mathbf{F}$ into a plastic part $\mathbf{F}^p$, which accounts for the cumulative effect of dislocation motion, and an elastic part $\mathbf{F}^e$, which accounts for the remaining non-plastic deformation. Following Teodosiu [81] and others [82, 83, 84, 85, 86], we shall assume that $\mathbf{F}^p$ leaves the crystal lattice not only essentially undistorted, but also unrotated. Thus, the distortion and rotation of the lattice is contained in $\mathbf{F}^e$. This choice of kinematics uniquely determines the decomposition (5.1). By virtue of (5.1), the deformation power per unit undeformed volume takes the form

$$\mathbf{P} : \dot{\mathbf{F}} = \bar{\mathbf{P}} : \dot{\mathbf{F}}^e + \bar{\mathbf{\Sigma}} : \bar{\mathbf{L}}^p \tag{5.2}$$

where

$$\bar{\mathbf{P}} = \mathbf{P}\mathbf{F}^{pT}, \qquad \bar{\mathbf{\Sigma}} = \mathbf{F}^{eT}\mathbf{P}\mathbf{F}^{pT}, \qquad \bar{\mathbf{L}}^p = \dot{\mathbf{F}}^p\mathbf{F}^{p-1} \tag{5.3}$$

Here, $\bar{\mathbf{P}}$ defines a first Piola–Kirchhoff stress tensor relative to the intermediate configuration $\bar{\mathcal{B}}_t$, and $\bar{\mathbf{\Sigma}}$ a stress measure conjugate to the plastic velocity gradients $\bar{\mathbf{L}}^p$ on $\bar{\mathcal{B}}_t$. The work conjugacy relations expressed in (5.2) suggest plastic flow rules and elastic stress-strain relations of the general form

$$\bar{\mathbf{L}}^p = \bar{\mathbf{L}}^p(\bar{\mathbf{\Sigma}}, \bar{\mathbf{Q}}), \qquad \bar{\mathbf{P}} = \bar{\mathbf{P}}(\mathbf{F}^e, \bar{\mathbf{Q}}) \tag{5.4}$$

Here, $\bar{\mathbf{Q}}$ denotes some suitable set of internal variables defined on the intermediate configuration, for which equations of evolution, or hardening laws, are to be supplied. A standard exercise shows that the most general form of (5.2) consistent with the

principle of material frame indifference is

$$\bar{\mathbf{P}} = \mathbf{F}^e \bar{\mathbf{S}}(\bar{\mathbf{C}}^e), \qquad \bar{\mathbf{C}}^e = \mathbf{F}^{eT}\mathbf{F}^e \tag{5.5}$$

where $\bar{\mathbf{S}} = \bar{\mathbf{C}}^{e-1}\bar{\mathbf{\Sigma}}$ is a symmetric second Piola-Kirchhoff stress tensor relative to the intermediate configuration $\bar{\mathcal{B}}_t$, and $\bar{\mathbf{C}}^e$ is the elastic right Cauchy-Green deformation tensor on $\bar{\mathcal{B}}_t$. For most applications involving metals, a linear—but anisotropic—relation between $\bar{\mathbf{S}}$ and the elastic Lagrangian strain $\bar{\mathbf{E}}^e = (\bar{\mathbf{C}}^e - \mathbf{I})/2$ can be assumed without much loss of generality. Higher-order moduli are given by Teodosiu [87].

From the kinematics of dislocation motion, it has been shown by Taylor (1938) [88] and Rice [86] that (5.4) is of the form

$$\bar{\mathbf{L}}^p = \sum_\alpha \dot{\gamma}^\alpha \bar{\mathbf{s}}^\alpha \otimes \bar{\mathbf{m}}^\alpha \tag{5.6}$$

where $\dot{\gamma}^\alpha$ is the shear rate on slip system α and $\bar{\mathbf{s}}^\alpha$ and $\bar{\mathbf{m}}^\alpha$ are the corresponding slip direction and slip plane normal. At this point, the assumption is commonly made that $\dot{\gamma}^\alpha$ depends on stress only through the corresponding resolved shear stress τ^α, *i.e.*,

$$\dot{\gamma}^\alpha = \dot{\gamma}^\alpha(\tau^\alpha, \bar{\mathbf{Q}}) \tag{5.7}$$

which is an extension of Schmid's rule. If (5.7) is assumed to hold, then it was shown by Rice [86] and by Mandel [85] that the flow rule (5.6) derives from a viscoplastic potential.

In order to complete the constitutive description of the crystal, hardening relations governing the evolution of the internal variables $\bar{\mathbf{Q}}$ need to be provided. In this work, we adopt the forest dislocation hardening model for f.c.c. metals of Cuitiño *et al.* [78]. A synopsis of the main assumptions of the model together with the key constitutive relations is provided below for completeness.

The rate of shear deformation on slip system α is given by a power-law of the form:

$$\dot{\gamma}_\alpha = \begin{cases} \dot{\gamma}_0 \left[\left(\frac{\tau^\alpha}{g^\alpha} \right)^{1/m^\alpha} - 1 \right], & \text{if } \tau^\alpha \geq g^\alpha, \\ 0, & \text{otherwise.} \end{cases} \tag{5.8}$$

In this expression, m^α is the strain-rate sensitivity exponent, $\dot{\gamma}_0$ is a reference shear strain rate and g^α is the current shear flow stress on slip system α. Implicit in the form in which (5.8) is written is the convention of differentiating between the positive and negative slip directions $\pm\mathbf{m}^\alpha$ for each slip system, whereas the slip rates $\dot{\gamma}^\alpha$ are constrained to be nonnegative.

For multiple slip, the evolution of the flow stresses is found from an analysis based on statistical mechanics to be governed by a *diagonal* hardening law:

$$\dot{g}^\alpha = \sum_\alpha h^{\alpha\alpha} \dot{\gamma}^\alpha \tag{5.9}$$

where $h^{\alpha\alpha}$ are the *diagonal* hardening moduli:

$$h^{\alpha\alpha} = \left(\frac{\tau_c^\alpha}{\gamma_c^\alpha} \right) \left(\frac{g^\alpha}{\tau_c^\alpha} \right)^3 \left\{ \cosh \left[\left(\frac{\tau_c^\alpha}{g^\alpha} \right)^2 \right] - 1 \right\} \quad \text{(no sum in } \alpha) \tag{5.10}$$

In this expression,

$$\tau_c^\alpha = r\mu b\sqrt{\pi n^\alpha} \quad \text{and} \quad \gamma_c^\alpha = \frac{b\rho^\alpha}{2\sqrt{n^\alpha}} \quad \text{(no sum in } \alpha) \tag{5.11}$$

are a characteristic shear stress and strain for the slip system α, respectively. The values of τ_c^α and γ_c^α determine the location of the "bend" in the resolved shear stress-slip strain curve associated with the observable yielding during experiments. Thus, τ_c correlates well with the value of the flow stress determined by back extrapolation. In expressions (5.11), μ is the shear modulus, n^α is the density of obstacles in slip system α, ρ^α is the dislocation density in slip system α, b is the Burgers vector and r is a numerical coefficient of the order of 0.3 that modulates the strength of the obstacle in slip plane α given by a pair of forest dislocations separated by a distance

l. This strength is estimated as

$$s^\alpha = r\frac{\mu b}{l}. \tag{5.12}$$

In order to complete the constitutive formulation, evolution equations for the obstacle density n^α and dislocation density ρ^α are provided. Evidently, n^α is a function of the dislocation densities in all remaining systems. The experimental work of Franciosi and co-workers [89, 90, 91, 92, 93] is suggestive of a dependence of the form

$$n^\alpha = \sum_\beta a^{\alpha\beta}\rho^\beta \tag{5.13}$$

Experimentally determined values of the interaction matrix $a^{\alpha\beta}$ have been given by Franciosi and Zaoui [89] for the twelve slip systems belonging to the family of $\{111\}$ planes and $\langle 110\rangle$ directions in f.c.c. crystals. They classify the interactions according to whether the dislocations belong to the same system (interaction coefficient a_0), fail to form junctions (interaction coefficient a_1), form Hirth locks (interaction coefficient a_1), co-planar junctions (interaction coefficient a_1), glissile junctions (interaction coefficient a_2), or sessile Lomer-Cottrell locks (interaction coefficient a_3), with $a_0 \leq a_1 \leq a_2 \leq a_3$. Franciosi [92] has also found the interaction coefficients to be linearly dependent on the stacking fault energy of the crystal, the degree of anisotropy increasing with decreasing stacking fault energy.

Finally, an analytical expression for the evolution of ρ^α with the applied slip strain can be postulated by considering that the *dislocation production* is dominated by multiplication by cross glide and *dislocation annihilation* is proportional to the probability of having two dislocations segments of different sign in a small neighborhood of each other. The resulting expression is given by

$$\rho^\alpha = \rho_{\text{sat}}\left[1 - \left(1 - \frac{\rho_0}{\rho_{\text{sat}}}\right)\mathrm{e}^{-\gamma^\alpha/\gamma_{\text{sat}}}\right] \tag{5.14}$$

where ρ_{sat} and γ_{sat} are the saturation dislocation density and saturation shear slip, which are determined by the multiplication and annihilation rates.

In this model, the only two differences with Dao *et al.*'s constitutive model have

been in the definitions of the diagonal hardening coefficients $h^{\alpha\alpha}$ in Equation (5.10), and of the shear deformation rate law $\dot{\gamma}_\alpha$ in Equation (5.8). In Dao *et al.*'s model, a hardening power law is adopted [29]:

$$h^{\alpha\alpha}(\gamma_a) = \mu\nu_\alpha \left(1 + \frac{\mu}{\tau_0^\alpha}\gamma_a\right)^{\nu_\alpha - 1} \tag{5.15}$$

where ν_α and τ_0^α are respectively the strain hardening exponent and the critical resolved shear stress for slip system α, γ_a is the accumulated sum of slips, and the shear deformation rate on slip system α is given by the following power-law form:

$$\dot{\gamma}_\alpha = \begin{cases} \dot{\gamma}_0 \left(\frac{\tau^\alpha}{g^\alpha}\right)^{1/m^\alpha}, & \text{if } \tau^\alpha \geq 0, \\ 0, & \text{otherwise.} \end{cases} \tag{5.16}$$

The preceding framework for single crystal plasticity is modified for the purpose of describing the influence of twins present in the lattice. The modifications are based on the two-dimensional model of Dao *et al.* [29] who proposed to consider the slip planes parallel to the twin boundaries as soft shear planes without barriers for dislocation motion, whereas the remaining slip planes piercing the twin boundaries have a harder response reflecting the fact that dislocation gliding in those planes will encounter the barriers provided by the twin boundaries, and consequently giving to the material a preferred shearing direction [29]. This model follows a homogenized approach based on twin density, which avoids the consideration of individual twins. The resolved shear stress, the hardening exponent and the rate sensitivity for the hard modes are accordingly modified as a function of twin spacing [29].

In the two-dimensional model, only three systems are considered, see Figure 5-4, in which the planes are perpendicular to the two dimensions considered whereas the slip directions are constrained to be in the plane. In the three-dimensional model proposed here, these restrictions are eliminated and all twelve slip systems in the f.c.c. lattice are considered. Among the four f.c.c. slip planes, each one with three possible slip directions, one of the planes is chosen as the twin plane whose three slip directions are taken as the soft modes and, on the three remaining planes piercing

the twin plane, a hard slip mode is assigned to all three slip directions.

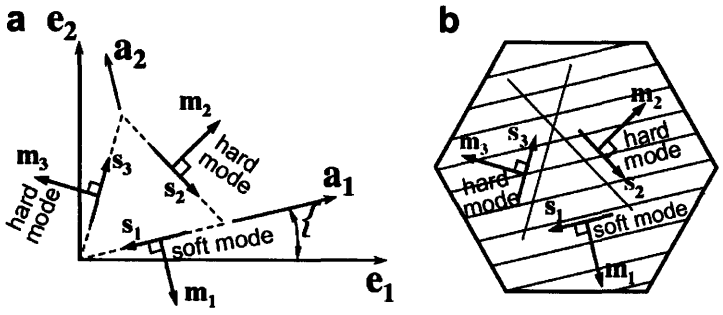

Figure 5-4: Dao *et al.*'s 2D model of twinned polycrystal; the twinned slip system is considered as the soft shear mode and the two others are labeled as hard shear mode [29]

In our calculations of the tensile response of ultrafine crystalline copper with different twin densities, we adopt the soft and hard mode parameter values from the same reference [29]. The critical resolved shear stress for the soft mode is taken as

$$g_0^{\text{soft}} = 67MPa \tag{5.17}$$

which is an estimate for polycrystalline Cu with grain size $d_{\text{grain}} \sim 500nm$ and effective yield stress of 200MPa.

For a given twin spacing d_{twin}, the hard mode critical resolved shear stress is assumed to follow a Hall-Petch relation:

$$g_0^{\text{hard}} = g_{\text{th}} \left(\frac{d_{\text{th}}}{d_{\text{twin}}} \right)^{1/2} \tag{5.18}$$

where d_{th} and g_{th} are the minimum twin spacing under which no pile up occurs and its corresponding shear strength, respectively. The values of both parameters are:

$$\begin{cases} g_{\text{th}} = 1GPa \\ d_{\text{th}} = 13nm \end{cases} \tag{5.19}$$

Hardening is suppressed in the hard modes by setting $h_{\alpha\beta} = 0$ in Equation (5.10)

reflecting the negligible strain hardening of nanocrystalline materials.

Finally, the rate sensitivity **for all modes** is taken as a volume weighted average of the crystal interior sensitivity m_{XTL} and the "twin boundary affected zone" (TBAZ) sensitivity m_{TBAZ}:

$$m_\alpha = (1 - f_{\text{TBAZ}})m_{\text{XTL}} + f_{\text{TBAZ}}m_{\text{TBAZ}}, \ \forall\alpha \tag{5.20}$$

where f_{TBAZ} is the volume fraction of the TBAZ, defined as the region around the twin boundary of thickness equal to 7-10 lattice spacings. Following [29], we take $m_{\text{XTL}} = 0.005$ and $m_{\text{TBAZ}} = 0.085$.

The full set of constants of the model crystal plasticity for copper is given in Table 5.1:

Table 5.1: Model parameters for Cu

$C_{11}\ (GPa)$	168.4		
$C_{12}\ (GPa)$	121.4		
$C_{44}\ (GPa)$	75.4		
$\dot{\gamma}_0\ (s^{-1})$	100		
r	0.3		
b (m)	2.56×10^{-10}		
$\rho_0\ (m^{-2})$	10^{10}		
$\rho_{\text{sat}}\ (m^{-2})$	10^{13}		
$\gamma_{\text{sat}}\ (m^{-2})$	0.001		
a_0	8×10^{-4}		
a_1	40×10^{-4}		
a_2	80×10^{-4}		
a_3	120×10^{-4}		
$g_0^{\text{soft}}\ (MPa)$	67		
$h_{\alpha\beta}^{\text{soft}}$	cf. Equation (5.10)		
$h_{\alpha\beta}^{\text{hard}}$	0		
$\boldsymbol{d_{\text{twin}}\ (nm)}$	**100**	**35**	**15**
$g_0^{\text{hard}}\ (MPa)$	360.56	609.45	930.95
m	0.011	0.022	0.043

5.2 Fracture initiation criterion

Intuitively, most of the shear strain is expected to be concentrated along the twin boundary boundaries systems, indicating that failure mechanisms should *a priori* primarily arise there. Accordingly, the fracture criterion adopted consists of a maximum of slip per unit length $\delta_{\max}$ along the twin systems, see Figure 5-5. For a given twin spacing d_{twin}, the maximum allowed shear strain in the twin systems before the initiation of failure is consequently defined by

$$\gamma_{\max} = n\delta_{\max} \tag{5.21}$$

where $n = 1/d_{\text{twin}}$ is the number of twin boundary per unit length. It should be emphasized that because this criterion is based on a fracture initiation, as opposed to the observed material failure, a delay between the two events can be expected; short for the cases with low ductility and longer for the ones with higher ductility.

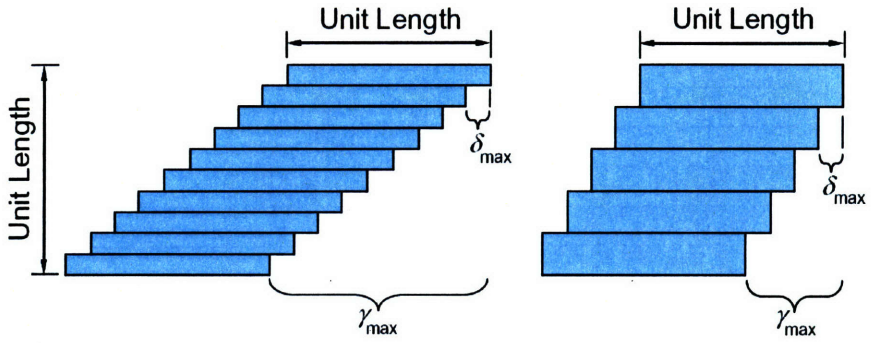

Figure 5-5: Fracture criterion for twinned polycrystal adopted from [29]; each twin boundary allows a maximum of $\delta_{\max}$ of slip, leading to a maximum shear of $\gamma_{\max} = n\delta_{\max}$ where n is the number of twin boundaries per unit length

In [29], the model was calibrated against the experimental results of Lu *et al.* [26], Figure 5-3. The fracture criterion was chosen such that both experimental and simulation fracture strains for $d_{\text{twin}} = 100nm$ would coincide. This was accomplished by taking $\gamma_{\max} = 100\%$ for $d_{\text{twin}} = 15nm$, which corresponds to $\delta_{\max} = 15nm$ [29]. Figure 5-6 shows the stress-strain curves of their two-dimensional simulations for

$d_{\text{twin}} = 100nm$, $35nm$ and $15nm$, and for the different strain rates $6 \times 10^{-3}s^{-1}$, $6 \times 10^{-2}s^{-1}$ and $6 \times 10^{-1}s^{-1}$. The failure initiation according to the calibrated fracture criterion is represented by the symbol "X".

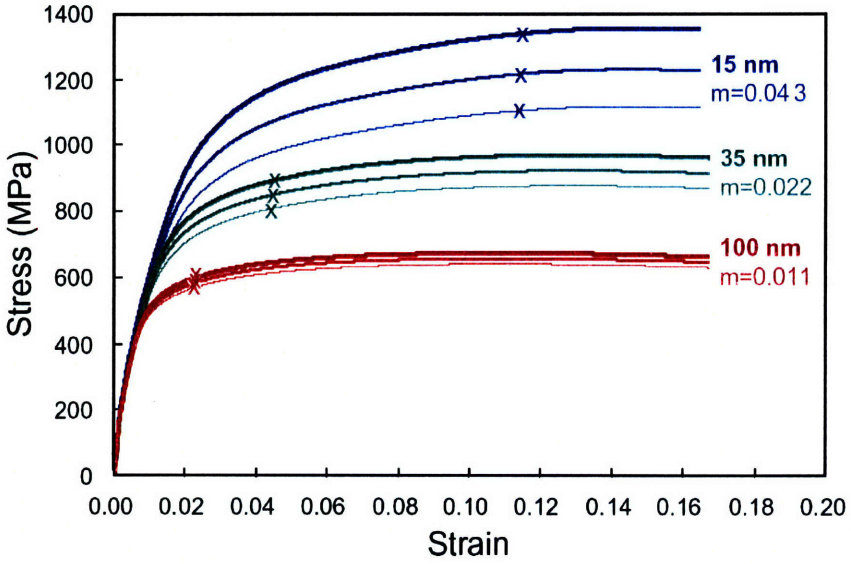

Figure 5-6: Simulated stress-strain curves from [29] for $d_{\text{twin}} = 100nm$, $35nm$ and $15nm$ and strain rates $6 \times 10^{-3}s^{-1}$, $6 \times 10^{-2}s^{-1}$ and $6 \times 10^{-1}s^{-1}$; the symbol "X" indicates the initiation of failure according to the adopted fracture criterion

The comparison between Figure 5-3 and Figure 5-6 confirms that the chosen modeling approach captures adequately the deformation and failure mechanisms in nano-twinned ultrafine crystals.

5.3 Numerical simulations

In this section, the model of ultrafine crystals with embedded nano-twins presented above is used to investigate the three-dimensional aspects of the dependence of the stress-strain response and ductility of ultrafine copper on twin density. In the following, we provide a description of the simulation setup followed by the corresponding results.

5.3.1 Simulation setup

Two different model microstructures are used. The first one is based on an extruded two-dimensional Voronoï diagram representing a columnar polycrystalline sample of 16 grains. This configuration is used for comparison with the two-dimensional model in [29]. The corresponding mesh is composed of 7,451 tetrahedra and 788 interface elements and is used as a three-dimensional counterpart for the two-dimensional simulations in [29], see Figure 5-7(a). The second model is created following the approach already described in Chapters 3 and 4. It consists of a finite element mesh of a 6x6x6 idealized cube-shaped polycrystalline sample. The geometry of each grain corresponds to a tetrakaidecahedron discretized with 192 tetrahedra. The polycrystalline sample is composed of 559 grains for a total of 82,944 tetrahedra and 15,120 interface elements, see Figure 5-7(b). In both cases, the three-dimensional crystallographic nano-twin model previously described is used with a random crystal orientation for each grain and with the (111) plane taken as the twin plane.

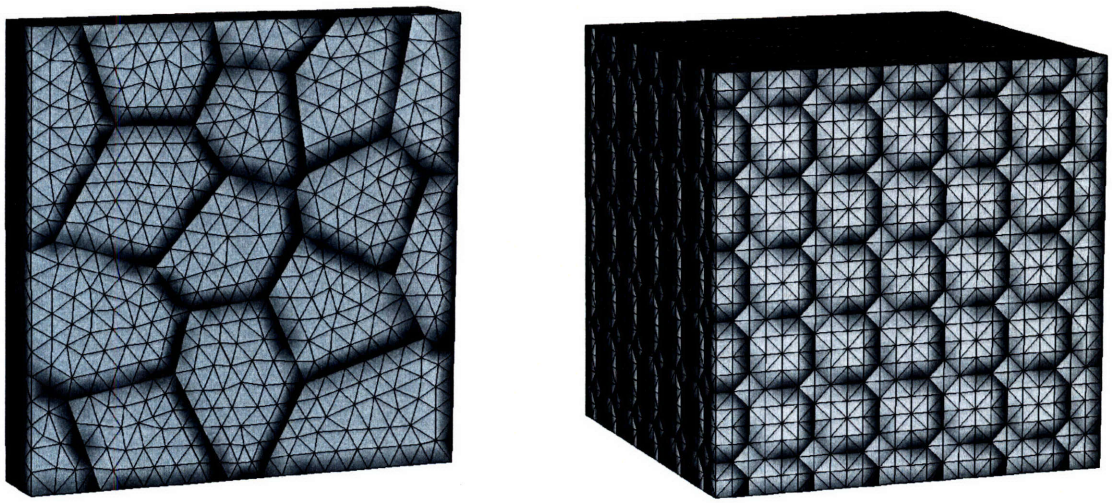

(a) Columnar 3D mesh

(b) Full 3D mesh

Figure 5-7: Model meshes used for the simulations of nano-twinned ultrafine polycrystals; the dark shadows denote the grain boundaries

For both meshes, displacement-controlled tensile test conditions are simulated by constraining the mesh nodes at the bottom face of the specimen, whereas specified displacements are applied to the nodes on the top face. For the columnar mesh, plane

strain conditions are imposed by also constraining the motion on the two lateral faces in the direction perpendicular to the direction of loading. The experimental results corresponding to a deformation rate $\dot{\epsilon} = 6 \times 10^{-4} s^{-1}$ is used for comparison with the numerical results, see Figure 5-3.

The simulations are conducted on a parallel computer on up to 200 processors.

5.3.2 Plane strain simulations

In order to compare with the plane strain model in [29], we have conducted simulations that attempt to approximate these conditions by using a columnar-grain polycrystalline structure, see Figure 5-7(a). Even though the experimental samples obtained by Shen, Lu *et al.* [28] consist of equiaxed grains, the two-dimensional modeling assumption can be justified as a first approximation based on TEM analyses showing that twin boundaries are predominantly aligned with the growth direction, *i.e.*, perpendicular to the thin sheet surface. This simplifying assumption is subsequently eliminated in our full three-dimension simulations.

Tensile load simulations are conducted for three different twin densities corresponding to twin spacings $d_{\text{twin}} = 100nm$, $35nm$ and $15nm$. The model parameters are taken from Table 5.1. In addition, the critical value of $\delta_{\max}$ used as a criterion for fracture initiation is calibrated to the experiments so that the strain-to-fracture in the experiments and simulations coincide. The calibration is done taking as a basis the sample with the largest twin spacing, using $\delta_{\max} = 27.5nm$. Subsequently, this parameter is kept fixed.

Figure 5-8 compares the stress-strain curves obtained in the simulations with the experimental results from [27, 28, 29] for the twin spacings $d_{\text{twin}} = 100nm$, $35nm$ and $15nm$. The simulations were stopped as soon as the fracture criterion was met in one of the twin slip systems.

It can be seen in this comparison that a general good agreement is obtained. In all three cases, the stress level reached by the simulations is comparable with the experimental results. Because of the very low ductility observed in the $d_{\text{twin}} = 100nm$ case, it is reasonable to assume that fracture initiation and failure occur almost simulta-

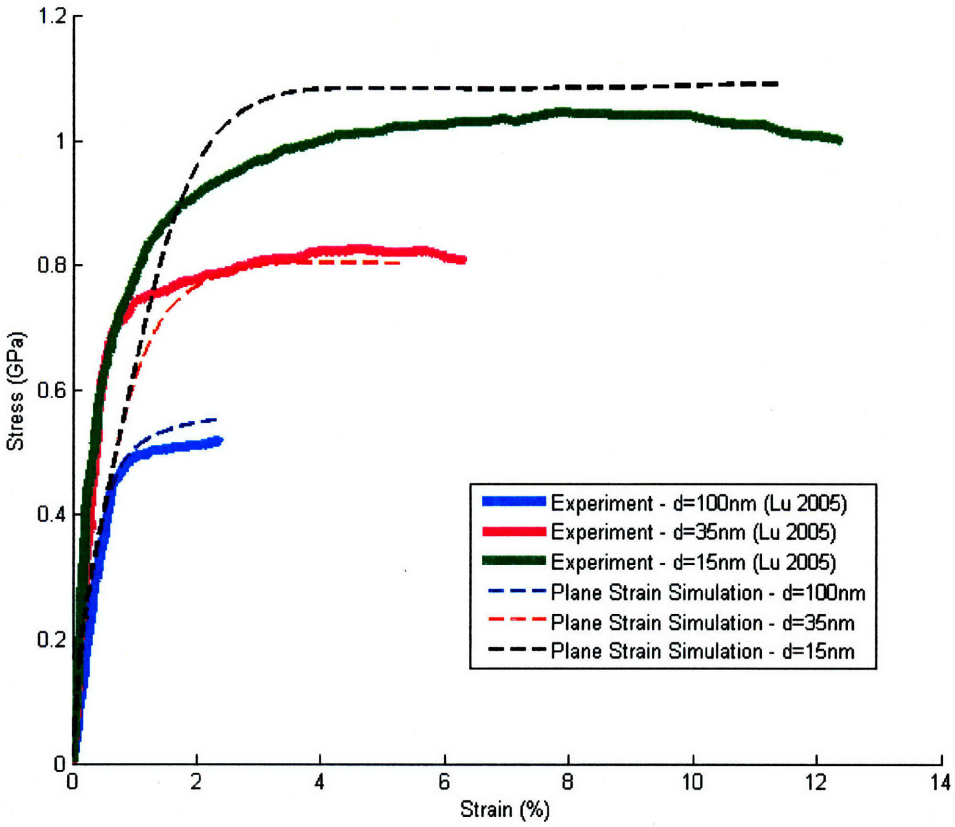

Figure 5-8: Lu *et al.*'s experimental tensile tests for different twin spacings $d_{\text{twin}} = 100nm$, $35nm$ and $15nm$ [27, 28, 29] and the corresponding plane strain simulations. The simulations are stopped when the fracture initiation criterion is met

neously, which justifies fitting the fracture initiation criterion to the experimentally observed strain-to-failure for this case.

In the cases of $d_{\text{twin}} = 35nm$ and $15nm$, the model predicts failure initiation approximately 1% of strain earlier than the experimentally observed failure, which is expected from the increased ductility. Overall, this three-dimensional columnar plane strain model incorporating basic mechanisms of the deformation of nano-twinned ultrafine polycrystals provides a reasonable description of the stress-strain response observed experimentally, including the twin spacing dependence of the yield stress and strain-to-fracture.

5.3.3 Full three-dimensional simulations

Three-dimensional simulations were conducted for the purpose of assessing the influence of the plane strain assumption. In this series of simulations, the 6x6x6 mesh shown in Figure 5-7(b) is used with a fully random twin orientation.

The same three cases were simulated using the calibrated model with the same fracture criterion ($\delta_{\text{max}} = 27.5nm$). The stress-strain curves obtained are shown and compared with the experiments in Figure 5-9.

The stress levels reached in this configuration for each case are very similar to the ones observed in the previous cases on Figure 5-8. The main difference comes from the fracture initiation. In the cases $d_{\text{twin}} = 15nm$ and $35nm$, the failure is initiated respectively roughly 1% and 2% before the experimentally observed failure in [27, 28, 29]. On the other hand, for the case $d_{\text{twin}} = 15nm$, the failure initiation is predicted nearly 4% *after* the actual experimental failure.

5.4 Discussion

This observed discrepancy between the columnar plane strain case (Figure 5-8) and the full three-dimensional case (Figure 5-9) indicates intrinsic differences in the corresponding deformation mechanisms. Whereas, in the first case, the material deformation is constrained to occur in a plane, the extension to three dimensions allows the

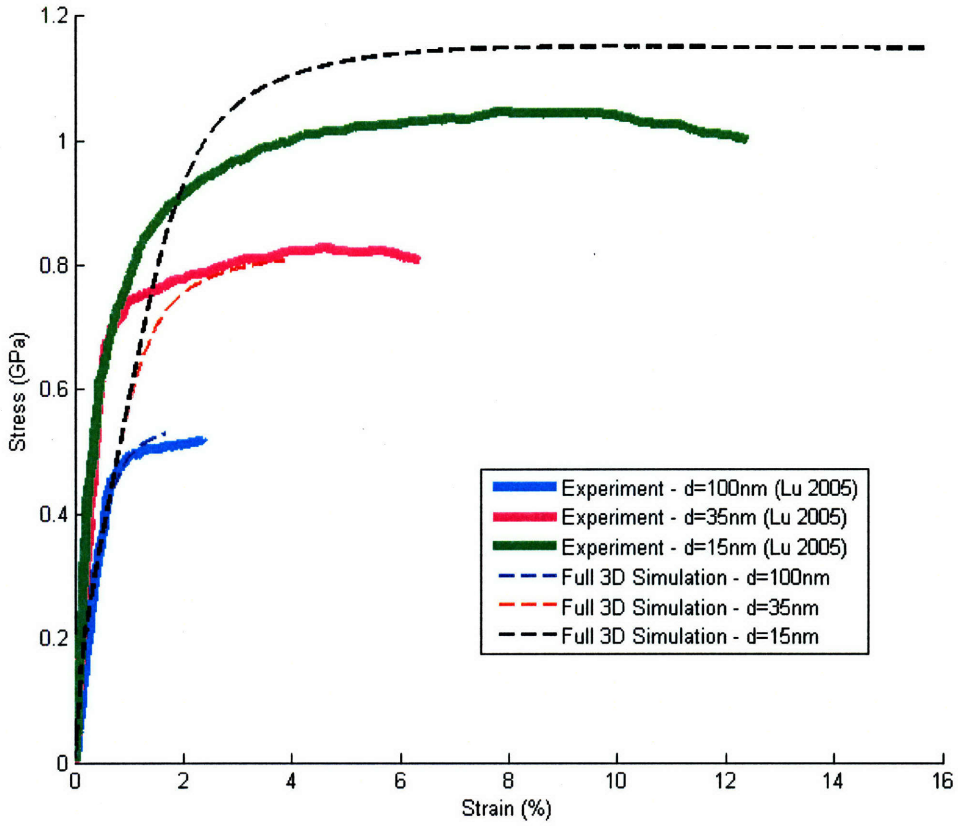

Figure 5-9: Lu *et al.*'s experimental tensile tests for different twin spacings $d_{\text{twin}} = 100nm$, $35nm$ and $15nm$ [27, 28, 29] and the corresponding 3D simulations. The simulations are stopped when the fracture initiation criterion is met

consideration of other mechanisms such as out-of-plane slips, cross slips/hardening and grain rotation.

For $d_{\text{twin}} = 100nm$ and $35nm$, the three-dimensional simulations predict fracture initiation at earlier stages of deformation which could be due to the increased number of nucleation sites and slip directions. In the case of $d_{\text{twin}} = 15nm$, a larger strain is predicted before the fracture initiation criterion is reached. This can be explained by the presence of additional kinematic mechanisms in the three-dimensional model, including grain rotation, and by the increased strength for smaller twin spacing which results in a reduction in the amount of slip for a given strain.

Notwithstanding the relative success of the model in capturing the basic features of the stress-strain response of nano-twinned ultrafine crystals, it is clear from the results presented that additional theoretical as well as experimental studies are required to corroborate and determine the extent of the validity of the proposed deformation and failure mechanisms. For example, an important mechanism that is not considered in the present model is the accommodation of deformation provided by the migration of twin boundaries, which has been shown to play an important role in some cases [76, 77].

A first step in this direction should involve using the computational framework presented in this thesis to conduct a number of polycrystalline configurations with increasing number of grains and different grain configurations and crystallographic orientations to explore the statistical nature of the failure response. This additional work will be reported in a journal paper which is in preparation at the time of the writing of this thesis.

Chapter 6

Conclusion

In this thesis, continuum models of nanoscale deformation and failure mechanisms for nanocrystalline and nano-twinned ultrafine crystalline metals subject to a wide range of loading conditions have been presented.

One of the contributions of this thesis is a three-dimensional continuum model aimed at investigating the effective response of nanocrystalline metals under quasi-static and high strain-rate conditions. The phenomenological model appears to provide an adequate continuum description of experimental observations and atomistic predictions of the yield behavior of nanocrystals. In addition, the results are consistent with the hypothesis that grain boundary kinematic mechanisms of sliding and accommodation are responsible for the softening of nanocrystals with decreasing grain sizes. In particular, the model reproduces the reverse Hall-Petch effect in agreement with atomistic [14] and experimental results [40]. Finally, the fit of both high strain-rate and quasi-static response with a single set of model parameters suggests that the significant discrepancy between the experimentally observed strength of nanocrystalline copper and the corresponding atomistic predictions may be partially due to loading-rate effects.

In addition, the continuum model was extended to investigate the shock response of nanocrystals. The required extension included an EOS to describe the volumetric response of the grain interiors under shock loading, a shock-capturing scheme and a rate dependent plasticity model to describe the deviatoric response. Furthermore,

grain boundary frictional mechanisms limiting sliding under strong state of compression were incorporated into the grain boundary model using a Mohr-Coulomb law. A set of parameters was found fitting the key features of the shock response obtained with atomistic models, *i.e.* shock speed, pressure behind the shock and the overall characteristics of the deviatoric response including the peak and tail of the Von Mises stress profile. The influence of grain boundary frictional mechanisms under shock loading conditions was also studied and compared to atomistic results. It was concluded that more accurate descriptions may require an improved EOS for the grain interior, and that it is necessary to add friction in the model to avoid unphysical oscillations.

A three-dimensional model of ultrafine crystals with embedded growth nano-twins was developed taking as a basis the two-dimensional model proposed by Dao *et al.* [29]. The approach is based on a crystal plasticity model for the grain bulk, modified to account for the presence of twin boundaries acting as dislocation barriers. In addition, a failure initiation criterion consisting of a limiting value of slip on the twin planes was implemented and calibrated against experimental results [29, 27]. The consideration of out-of-plane slip, cross slip/hardening and grain rotation enabled the investigation of three-dimensional aspects of the dependence of the stress-strain response of ultrafine copper with twin density. The results showed an increase of ductility and strength with decreasing twin spacing, in agreement with two-dimensional simulations and experimental results, but exhibited a larger increase of strain-to-fracture initiation for the smallest twin spacings. This suggests that additional mechanisms are available in three dimensions to accommodate the deformation, resulting in a postponed failure. These results suggest that an improved ductility could be obtained if the orientation of the twin boundaries in the grains can be distributed in a fully random three-dimensional manner.

As a conclusion to this thesis, the continuum approach provides a plausible modeling paradigm for describing the unique mechanisms of deformation and failure in nanocrystals as well as in nano-twinned ultrafine crystals.

Future work

The work presented in this thesis has focused on the formulation and development of a computational framework for the continuum description of deformation and failure mechanisms in nanocrystalline metals. The framework was used to describe a number of unique aspects pertaining to the mechanical response of these materials and emphasis was given to the verification and validation of the model results against atomistic descriptions and experimental characterizations. However, it is clear that the models presented are by no means comprehensive and require further investigation. This includes the consideration of aspects of the response that have not been taken into account in this work, as well as extensions to describe additional processes that are emerging as important from experimental observations. Among a possible list of suggestions for future work, the following can be identified.

The model presented in Chapter 2 and used in Chapter 3 for the analysis of the grain size dependence of the strength of nanocrystal is focused exclusively on the aptitude of the model to capture the reverse Hall-Petch effect. By introducing in the grain bulk either conventional crystal plasticity and modifying the critical resolved shear stress as a function of the grain size [31, 32, 36], or using strain-gradient plasticity [94] as a way of capturing the scale effect associated to intragrain plasticity in nanocrystalline metals, the competition between grain bulk plasticity and grain boundary deformation mechanisms could be fully represented. This extension would lead to a full three-dimensional characterization of the transition from direct to inverse Hall-Petch effect within the continuum framework. In addition, consideration of temperature in addition to rate dependence would allow a more complete differentiation of atomistic simulations between Molecular Statics at 0K and Molecular Dynamics at finite temperature.

The extension of this model in Chapter 4 to investigate the shock response of nanocrystals exhibited a discrepancy between the simulated shock speed of propagation in our model and the one predicted by Molecular Dynamics. It was shown that the parameters of the Mie-Grüneisen/Hugoniot EOS could be adjusted to obtain the

shock speed or the pressure, but not both. This suggests that a more accurate description may require the consideration of higher order terms in the expansion of the pressure. The Von Mises stress profile of MD calculations also exhibited a very rapid relaxation behind the front shock thus suggesting an unusually high rate dependence. In the continuum model, it was found that even adopting an extremely high rate dependence by choosing very low values of the rate dependence exponent was not sufficient to obtain such rapid decay in the Von Mises stress. In that respect also, further studies are needed to asses the real origin of this discrepancy, either originating in the rate dependence law adopted in the model or due to some limitation of the interatomic potential used in the MD simulations.

Finally, a limited number of simulations were conducted to analyze the ability of the model to describe the macroscopic response of nano-twinned ultrafine crystals, Chapter 5. The simulations consisted of two different grain topologies with 16 and 559 grains, respectively, and a single initial random texture. Future work should involve using the computational framework presented in this thesis to conduct a number of polycrystalline configurations with increasing number of grains and different grain configurations and crystallographic orientations to explore the statistical nature of the failure response. This additional work will be reported in a journal paper which is in preparation at the time of the writing of this thesis.

Appendix A

Entropy considerations in the propagation of shocks in nanocrystals

In this Appendix, an analysis aiming at evaluating the entropy contribution to the deformation under the shock conditions previously described will be conducted. Due to its empirical nature, the EOS adopted for describing the volumetric response of the nanocrystals in Chapter 4 intrinsically accounts for entropy contributions to the pressure. However, neither the deviatoric plastic response of the grains law nor the grain boundary constitutive law explicitly account for such contribution. It is therefore important to quantify the influence of the entropy on the deformation mechanisms. We prove here that this influence is negligible which justifies its omission in the constitutive law.

A.1 Constitutive law

The shock conditions of interest correspond to a shock pressure of the order of $50GPa$ and a piston velocity of $1000m/s$. In order to evaluate the contribution of entropy to the overall deformation under such conditions, we closely follow the analysis by Clifton [69], see also [95, 96, 97, 98, 99, 100, 101, 70].

To this end, we expand the internal energy per unit mass to third-order terms in the elastic strain tensor $\boldsymbol{\epsilon}^e$ and the specific entropy S:

$$\begin{aligned} U = {} & a_0 + a_1 J_1 + a_2 J_1^2 + a_3 J_2 + a_4 J_1^3 + a_5 J_1 J_2 + a_6 J_3 \\ & + b_1 J_1 S + b_2 J_1^2 S + b_3 J_2 S + b_4 J_1 S^2 \\ & + d_1 S + d_2 S^2 + d_3 S^3 \end{aligned} \tag{A.1}$$

where J_1, J_2 and J_3 are the three strain invariants:

$$\begin{cases} J_1 = \epsilon_1^e + \epsilon_2^e + \epsilon_3^e \\ J_2 = \epsilon_2^e \epsilon_3^e + \epsilon_2^e \epsilon_1^e + \epsilon_1^e \epsilon_2^e \\ J_3 = \epsilon_1^e \epsilon_2^e \epsilon_3^e \end{cases} \tag{A.2}$$

and where a_1, a_2, a_3, a_4, a_5, a_6, b_1, b_2, b_3, d_1, d_2 and d_3 are ten material constants corresponding to the series expansion coefficients, and ϵ_i^e is the elastic strain in the principal direction i. The first component of the First Piola-Kirchhoff stress tensor P_{11} follows from (A.1):

$$\begin{aligned} P_{11} = \rho_0 \lambda_2^p \lambda_3^p \big\{ & a_1 + 2a_2(\epsilon_1^e + \epsilon_2^e + \epsilon_3^e) + a_3(\epsilon_2^e + \epsilon_3^e) + 3a_4(\epsilon_1^e + \epsilon_2^e + \epsilon_3^e)^2 \\ & + a_5[(\epsilon_1^e + \epsilon_2^e + \epsilon_3^e)(\epsilon_2^e + \epsilon_3^e) + (\epsilon_1^e \epsilon_2^e + \epsilon_2^e \epsilon_3^e + \epsilon_3^e \epsilon_1^e)] \\ & + a_6 \epsilon_2^e \epsilon_3^e + b_1 S + 2b_2 S(\epsilon_1^e + \epsilon_2^e + \epsilon_3^e) + b_3 S(\epsilon_2^e + \epsilon_3^e) + b_4 S^2 \big\} \end{aligned} \tag{A.3}$$

where $\lambda_i^p = 1 + \epsilon_i^p$ is the plastic stretch in the principal direction i.

Differentiation of this equation and its reordering in terms of the axial stretch rates $\dot{\lambda}_i$ leads to:

$$\dot{\lambda}_1 = \frac{1}{\rho_0 c_1^2} \dot{P}_{11} + \frac{\kappa}{\rho_0 c_1^2} \dot{\lambda}_1^p - R\dot{S} \tag{A.4}$$

where

$$\begin{cases} c_1^2 = \frac{1}{(\lambda_1^p)^2}\left[2(a_2+b_2S)+6a_4(\epsilon_1^e+2\epsilon_2^e)+4a_5\epsilon_2^e\right] \\ \kappa = \rho_0\left[c_1^2\frac{\lambda_1}{\lambda_1^p}-\frac{2a_2+a_3}{(\lambda_1^p)^{3/2}}\right]-\frac{\rho_0}{(\lambda_1^p)^2}\left[2a_2(\epsilon_1^e+2\epsilon_2^e)+2a_3\epsilon_2^e+b_1S\right] \\ \quad -\frac{\rho_0}{(\lambda_1^p)^{3/2}}\left[6a_4(\epsilon_1^e+2\epsilon_2^e)+a_5(2\epsilon_1^e+5\epsilon_2^e)+a_6\epsilon_2^e+(2b_2+b_3)S\right] \\ R = \frac{1}{c_1^2\lambda_1^p}\left[b_1+2b_2(\epsilon_1^e+2\epsilon_2^e)+2b_3\epsilon_2^e+2b_4S\right] \end{cases} \tag{A.5}$$

At this stage, Clifton considered infinitesimal strain to simplify the weighing of the different terms of this equation [69]. In our analysis, we will not make this assumption as the axial strains for a pressure of $\sim 50GPa$ can be significant.

The estimation of each of the terms of Equations (A.4) and (A.5) is done in two steps. The first step consists of estimating each one of a_1, a_2, a_3, a_4, a_5, a_6, b_1, b_2, b_3, d_1, d_2 and d_3 following the method used by Clifton or by analogy with the corresponding values in aluminum when no specific values could be found for copper. The second step, on the other hand, consists of estimating the remaining unknowns in Equations (A.4) and (A.5) by taking them—or calculate them—directly from the simulations presented in Chapter 4.

A.2 Evaluation of the material constants

These 12 material constants are typically obtained from ultrasonic velocity measurements. Because of the difficulty to find the values of all 12 coefficients for copper in the literature, a comparison with the crystallographic second-order cubic elastic constants C_{11}, C_{12}, C_{44} as well as with Brugger's third-order elastic constants C_{111}, C_{112}, C_{123}, C_{144}, C_{166}, and C_{456} will be done [102], followed by the derivation of the "a_i" from these values. The remaining constants will be then calculated following Clifton's method [69].

Such evaluation assumes a cubic crystallographic orientation whereas the previous equations ((A.1) to (A.5)) did assume an isotropic configuration. Nevertheless, as

the purpose of this part is to evaluate the relative contribution of the entropy in the general constitutive laws and not to calculate precisely the different terms, the following analysis should stay valid under the purpose of this section.

Using the crystallographic elastic constants, we can write the elastic strain energy density Φ as [103, 104]:

$$\begin{aligned}
\Phi =& \frac{C_{11}}{2}\left(\epsilon_{11}^{e\,2}+\epsilon_{22}^{e\,2}+\epsilon_{33}^{e\,2}\right)\\
&+C_{12}\left(\epsilon_{11}^{e}\epsilon_{22}^{e}+\epsilon_{22}^{e}\epsilon_{33}^{e}+\epsilon_{33}^{e}\epsilon_{11}^{e}\right)\\
&+C_{44}\left(\epsilon_{12}^{e\,2}+\epsilon_{21}^{e\,2}+\epsilon_{23}^{e\,2}+\epsilon_{32}^{e\,2}+\epsilon_{31}^{e\,2}+\epsilon_{13}^{e\,2}\right)\\
&+\frac{C_{111}}{6}\left(\epsilon_{11}^{e\,3}+\epsilon_{22}^{e\,3}+\epsilon_{33}^{e\,3}\right)\\
&+\frac{C_{112}}{2}\left(\epsilon_{11}^{e\,2}(\epsilon_{22}^{e}+\epsilon_{33}^{e})+\epsilon_{22}^{e\,2}(\epsilon_{11}^{e}+\epsilon_{33}^{e})+\epsilon_{33}^{e\,2}(\epsilon_{22}^{e}+\epsilon_{11}^{e})\right)\\
&+C_{123}\epsilon_{11}^{e}\epsilon_{22}^{e}\epsilon_{33}^{e}\\
&+C_{456}(\epsilon_{12}^{e}+\epsilon_{21}^{e})(\epsilon_{23}^{e}+\epsilon_{32}^{e})(\epsilon_{13}^{e}+\epsilon_{31}^{e})\\
&+C_{144}\left[\epsilon_{11}^{e}(\epsilon_{23}^{e\,2}+\epsilon_{32}^{e\,2})+\epsilon_{22}^{e}(\epsilon_{31}^{e\,2}+\epsilon_{13}^{e\,2})+\epsilon_{33}^{e}(\epsilon_{12}^{e\,2}+\epsilon_{21}^{e\,2})\right]\\
&+C_{166}\left[(\epsilon_{12}^{e\,2}+\epsilon_{21}^{e\,2})(\epsilon_{11}^{e}+\epsilon_{22}^{e})+(\epsilon_{23}^{e\,2}+\epsilon_{32}^{e\,2})(\epsilon_{22}^{e}+\epsilon_{33}^{e})+(\epsilon_{31}^{e\,2}+\epsilon_{13}^{e\,2})(\epsilon_{33}^{e}+\epsilon_{11}^{e})\right]
\end{aligned} \tag{A.6}$$

Using Equation (A.2) and assuming that "1", "2" and "3" are the principal directions of deformation with "1" as the shock direction, this equation can be rewritten as:

$$\begin{aligned}
\Phi =& \left(\frac{1}{2}C_{11}+\frac{1}{2}C_{44}\right)J_1\\
&+\left(C_{12}-C_{11}-2C_{44}\right)J_1^2\\
&+\left(C_{166}+\frac{1}{6}C_{111}\right)J_2\\
&+\left(-\frac{1}{2}C_{111}+\frac{1}{2}C_{112}+\frac{1}{2}C_{144}-\frac{7}{2}C_{166}\right)J_1J_2\\
&+\left(\frac{1}{2}C_{111}-\frac{3}{2}C_{112}+C_{123}-\frac{9}{2}C_{144}+\frac{9}{2}C_{166}\right)J_3
\end{aligned} \tag{A.7}$$

This expression corresponds to the first line of Equation (A.1) multiplied by the density ρ_0 (U is per unit mass, Φ, per unit volume). Using the values of the copper crystallographic elastic constants from Overton and Gaffney for the second-order [105], and from Hiki and Granato for the third-order [106], we can identify term by term the two expressions and obtain:

$$\begin{cases} a_0 = 0 & \\ a_1 = 0 & \\ a_2 = \frac{\frac{1}{2}C_{11}+C_{44}}{\rho_0} & = 17.81 \times 10^6 Pa \\ a_3 = -\frac{C_{11}+2C_{44}-C_{12}}{\rho_0} & = -30.49 \times 10^6 Pa \\ a_4 = \frac{C_{166}+\frac{1}{6}C_{111}}{\rho_0} & = -110.70 \times 10^6 Pa \\ a_5 = \frac{-C_{111}+C_{112}+C_{144}-7C_{166}}{2\rho_0} & = 330.02 \times 10^6 Pa \\ a_6 = \frac{\frac{1}{2}C_{111}-\frac{3}{2}C_{112}+C_{123}-\frac{9}{2}C_{144}+\frac{9}{2}C_{166}}{\rho_0} & = -330.47 \times 10^6 Pa \end{cases} \tag{A.8}$$

By derivation of the pressure with respect to the temperature under uniform thermal expansion at zero pressure, it can be shown that [69]:

$$b_1 = -\frac{2T_0\alpha}{C_p}(3a_2 + a_3) \tag{A.9}$$

where α and C_p are respectively the coefficient of thermal expansion and the specific heat at constant pressure. For copper, those values at ambient conditions are taken as $\alpha \approx 17 \times 10^{-6} K^{-1}$ and $C_p \approx 380 J.kg^{-1}.K^{-1}$, which leads to:

$$b_1 \approx -611.65K \tag{A.10}$$

In Clifton's work, the values of b_2 and b_3 could only be roughly estimated. As aluminum and copper mechanical and thermal properties are of the same order of magnitude and under the purpose that we are only interested in approximated values, we will assume that these estimations can also be used for copper:

$$\begin{cases} b_2 \approx -130K \\ b_3 \approx 1350K \end{cases} \tag{A.11}$$

Assuming that both α and C_p stay relatively constant with respect to the temperature, the derivation of the pressure under uniform thermal expansion considerations at zero pressure and temperature, as we already did with Equation (A.9), also yields [69]:

$$\begin{aligned} b_4 =& \frac{T_0^2}{2C_p^2}(6a_2 + 2a_3)\frac{\partial \alpha}{\partial T} + \frac{T_0^2}{2C_p^2}(54a_4 + 18a_5 + 2a_6)\alpha^2 \\ &+ b_1\left(\frac{T_0}{2C_p^2}\frac{\partial C_p}{\partial T} - \frac{1}{2C_p}\right) + \frac{\alpha T_0}{2C_p}(12b_2 + 4b_3) \end{aligned} \tag{A.12}$$

Using previously calculated parameters with $\frac{\partial C_p}{\partial T}\Big|_{T_0} \approx 0.08 J.kg^{-1}.K^{-2}$ from Cezairliyan [107] and $\frac{\partial \alpha}{\partial T}\Big|_{T_0} \approx 7 \times 10^{-9} K^{-2}$ from Nix and MacNair [108], we finally obtain:

$$b_4 \approx 0.816 kg^2.K^2.J^{-1} \tag{A.13}$$

Note that we do not actually need to calculate d_1, d_2 and d_3 in order to evaluate the different terms of Equation (A.4).

A.3 Evaluation of the internal variables, stress and strain tensors

As explained previously, we use here the results obtained from the simulations presented in Section 4.4. *For the numerical set up adopted here*, we have:

$$\begin{array}{ll} \sigma_1^{\max} \approx -49GPa, & \sigma_2^{\max} \approx -45GPa \\ |\sigma_{12}|^{\max} \approx 430MPa, & \gamma_p^{\max} \approx 11\% \\ \epsilon_1^{\max} \approx -18\% & |\epsilon_2|^{\max} \approx 0.2\% \\ |\epsilon_1^p|^{\max} \approx 10.4\%, & |\epsilon_2^p|^{\max} \approx 5.7\% \\ |\epsilon_1^e|^{\max} \approx 7.6\%, & |\epsilon_2^e|^{\max} \approx 5.9\% \\ |\lambda_1^p|^{\min} \approx 89.6\% & \end{array} \tag{A.14}$$

Finally, following Clifton [69], the maximum specific entropy $S^{\max}$ can be approx-

imated by $\frac{8}{3}\frac{|\sigma_{12}|^{\max}\gamma_p^{\max}}{\rho_0 T_0}$, which leads to

$$S^{\max} \approx 47 J.K^{-1}.kg^{-1} \tag{A.15}$$

A.4 Evaluation of the entropy terms in the global equation

Using Equations (A.8), (A.9), (A.11), (A.13) and (A.14), we can now estimate each term of Equations (A.4) and (A.5):

$$\begin{cases} \underbrace{c_1^2}_{\sim 100\times10^6} = \frac{1}{(\lambda_1^p)^2}\left[\underbrace{2a_2}_{\sim 10\times10^6} + \underbrace{2b_2 S}_{\sim 10\times10^3} + \underbrace{6a_4(\epsilon_1^e + 2\epsilon_2^e)}_{\sim 100\times10^6} + \underbrace{4a_5\epsilon_2^e}_{-100\times10^6}\right] \\ \underbrace{\kappa}_{\sim 100\times10^9} = \underbrace{\rho_0\left[c_1^2\frac{\lambda_1}{\lambda_1^p} - \frac{2a_2+a_3}{(\lambda_1^p)^{3/2}}\right]}_{\sim 10\times10^6} - \frac{\rho_0}{(\lambda_1^p)^2}\left[\underbrace{2a_2(\epsilon_1^e+2\epsilon_2^e)}_{\sim 10\times10^6} + \underbrace{2a_3\epsilon_2^e}_{\sim 1\times10^6} + \underbrace{b_1 S}_{\sim 10\times10^3}\right] \\ \qquad - \frac{\rho_0}{(\lambda_1^p)^{3/2}}\left[\underbrace{6a_4(\epsilon_1^e+2\epsilon_2^e)}_{\sim 100\times10^6} + \underbrace{a_5(2\epsilon_1^e+5\epsilon_2^e)}_{\sim 100\times10^6} + \underbrace{a_6\epsilon_2^e}_{\sim 10\times10^6} + \underbrace{(2b_2+b_3)S}_{\sim 100\times10^3}\right] \\ \underbrace{R}_{\sim 10\times10^{-6}} = \frac{1}{c_1^2\lambda_1^p}\left[\underbrace{b_1}_{\sim 1\times10^3} + \underbrace{2b_2(\epsilon_1^e+2\epsilon_2^e)}_{\sim 0.1\times10^3} + \underbrace{2b_3\epsilon_2^e}_{\sim 0.1\times10^3} + \underbrace{2b_4 S}_{\sim 0.1\times10^3}\right] \end{cases} \tag{A.16}$$

which, taking a time interval $\Delta t = 10ps$, leads to:

$$\underbrace{\rho_0 c_1^2\dot{\lambda}_1}_{\sim 10\times10^{21}} = \underbrace{\dot{P}_{11}}_{\sim 10\times10^{21}} + \underbrace{\kappa\dot{\lambda_1^p}}_{\sim 1\times10^{21}} - \underbrace{\rho_0 c_1^2 R\dot{S}}_{\sim 10\times10^{18}} \tag{A.17}$$

As can be seen from the previous evaluations, the entropy terms for κ and c_1^2 are in both cases of the order of 0.1% of the highest neighboring terms. Only in R does it reach as much as 10% of the highest term, but then, the global contribution of the entropy term (multiple of R) in Equation (A.17), is of the order of 1% of the corresponding *smallest* other term.

Due to the empirical origin of the Hugoniot relation (adopted here for the description of the pressure), we have seen that the entropy contribution is naturally embedded into the equation of state. Additionally, this analysis shows that the contribution of entropy should not account for a significant portion of the deformation process, which justifies its omission in the deviatoric plastic response.

Bibliography

[1] K.S. Kumar, H. Van Swygenhoven and S. Suresh. Mechanical behavior of nanocrystalline metals and alloys. *Acta Materialia*, 51:5743–5774, 2003.

[2] C.J. Youngdahl, P.G. Sanders, J.A. Eastman and J.R. Weertman. Compressive yield strengths of nanocrystalline Cu and Pd. *Scripta Materialia*, 37:809–813, 1997.

[3] S.R. Agnew, B.R. Elliott, C.J. Youngdahl, K.J. Hemker and J.R. Weertman. Microstructure and mechanical behavior of nanocrystalline metals. *Materials Science and Engineering*, A285:391–396, 2000.

[4] H.V. Swygenhoven and J.R. Weertman. Preface to the viewpoint set on: mechanical properties of fully dense nanocrystalline metals. *Scripta Materialia*, 49:625–627, 2003.

[5] K.W. Jacobsen and J. Schiøtz. Nanoscale plasticity. *Nature Materials*, 1:15–16, 2002.

[6] H.V. Swygenhoven. Grain Boundaries and Dislocations. *Science*, 296(5565):66–67, 2002.

[7] E.O. Hall. The deformation and ageing of mild steel: III discussion of results. *Proceedings of the Physical Society of London*, B64:747–753, 1951.

[8] N.J. Petch. The cleavage strength of polycrystals. *Journal of the Iron and Steel Institute*, 174:25–28, 1953.

[9] A.H. Chokshi, A. Rosen, J. Karch and H. Gleiter. On the validity of the hall-petch relationship in nanocrystalline materials. *Scripta Mettalurgica*, 23:1679–1684, 1989.

[10] H.W. Song, S.R. Guo and Z.Q. Hu. A coherent polycrystal model for the inverse hall-petch relation in nanocrystalline materials. *NanoStructured Materials*, 11(2):203–210, 1999.

[11] M.A. Haque and M.T. A Saif. Mechanical behavior of 30-50 nm thick aluminum films under uniaxial tension. *Scripta Materiala*, 47:863–867, 2002.

[12] C.A. Schuh, T.G. Nieh and H. Iwasaki. The effect of solid solution W additions on the mechanical properties of nanocrystalline Ni. *Acta Materialia*, 51:431–443, 2003.

[13] M.A. Meyers, A. Mishra, and D. J. Benson. Mechanical properties of nanocrystalline materials. *Progress in Materials Science*, 51:427–556, 2006.

[14] J. Schiøtz, F.D. Di Tolla and K.W. Jacobsen. Softening of nanocrystalline metals at very small grain sizes. *Nature*, 391:561–563, 1998.

[15] S. Yip. The strongest size. *Nature*, 391:532–533, 1998.

[16] H. Van Swygenhoven, M. Spaczer, A. Caro, and D. Farkas. Competing plastic deformation mechanisms in nanophase metals. *Physical Review B-Condensed Matter*, 60(1):22–25, 1999.

[17] J. Schiøtz, T. Vegge, F.D. Di Tolla and K.W. Jacobsen. Atomic-scale simulations of the mechanical deformation of nanocrystalline metals. *Physical Review B*, 60(17):11971–11983, 1999.

[18] V. Yamakov, D. Wolf and S.R. Phillpot. Dislocation processes in the deformation of nanocrystalline aluminium by molecular-dynamics simulation. *Nature materials*, 1:1–4, 2002.

[19] D. Wolf, V. Yamakov, S.R. Phillpot, A. Mukherjee and H. Gleiter. Deformation of nanocrystalline materials by molecular-dynamics simulations: Relationship to experiments? *Acta Materialia*, 53:1–40, 2005.

[20] J. Schiøtz and K.W. Jacobsen. A maximum in the strength of nanocrystalline copper. *Science*, 301:1357–1359, 2003.

[21] M.K. Jain. *Processing and Mechanical Behavior of Ultrafine Grain Materials.* PhD thesis, California Institute of Technology, 1995.

[22] A.C. Lund and C.A. Schuh. Stength asymmetry in nanocrystalline metals under multiaxial loading. *Acta Materialia*, 53:3193–3205, 2005.

[23] E.M. Bringa, A. Caro, Y.M. Wang, M. Victoria, J. McNaney, B.A. Remington, R. Smith, B. Torralva and H. Van Swygenhoven. Ultra-high strength in nanocrystalline materials under shock loading. *Science*, 309:1838–1841, 2005.

[24] L. Lu, L.B. Wang, B.Z. Ding and K. Lu. High-tensile ductility in nanocrystalline copper. *Journal of Materials Research*, 15(2):270–273, 2000.

[25] R. Schwaiger, B. Moser, M. Dao, N. Chollacoop and S. Suresh. Some critical experiments on the strain-rate sensitivity of nanocrystalline nickel. *Acta Materialia*, 51:5159–5172, 2003.

[26] L. Lu, Y. Shen, X. Chen, L. Qian and K. Lu. Ultrahigh strength and high electrical conductivity in copper. *Science*, 304:422–426, 2004.

[27] L. Lu, R. Schwaiger, Z.W. Shan, M. Dao, K. Lu and S. Suresh. Nano-sized twins induce high rate sensitivity of flow stress in pure copper. *Acta Materialia*, 53:2169–2179, 2005.

[28] Y.F. Shen, L. Lu, Q.H. Lu, Z.H. Jin and K. Lu. Tensile properties of copper with nano-scale twins. *Scripta Materialia*, 53:2169–2179, 2005.

[29] M. Dao, L. Lu, Y.F. Shen and S. Suresh. Strength, strain-rate sensitivity and ductility of copper with nanoscale twins. *Acta Materialia*, 54:5421–5432, 2006.

[30] T. Zhu, J. Li, A. Samanta, H.G. Kim and S. Suresh. Interfacial plasticity governs strain rate sensitivity and ductility in nanostructured metals. *Proceedings of the National Academy of Sciences*, 104(9):3031–3036, 2007.

[31] Y.J. Wei and L. Anand. Grain-boundary sliding and separation in polycrystalline metals: application to nanocrystalline fcc metals. *Journal of the Mechanics and Physics of Solids*, 52:2587–2616, 2004.

[32] Y.J. Wei, C. Su and L. Anand. A computational study of the mechanical behavior of nanocrystalline fcc metals. *Acta Materialia*, 54:3177–3190, 2006.

[33] H. H. Fu, D. J. Benson, and M. A. Meyers. Analytical and computational description of the effect of grain size on yield stress of metals. *Acta Materialia*, 49:2567–2582, 2001.

[34] H.-H. Fu, D.J. Benson and M.A. Meyers. Computational description of nanocrystalline deformation based on crystal plasticity. *Acta Materialia*, 52:4413–4425, 2004.

[35] D.H. Warner, F. Sansoz and J.F. Molinari. Modeling of deformation in nanocrystalline copper using an atomistic-based continuum approach. *Mat. Res. Soc. Symp. Proc., 2003 MRS Fall Meeting*, 791:157–162, 2004.

[36] D.H. Warner, F. Sansoz and J.F. Molinari. Atomistic based continuum investigation of plastic deformation in nanocrystalline copper. *International Journal of Plasticity*, 22:754–774, 2006.

[37] M. Ortiz and A. Pandolfi. Finite-deformation irreversible cohesive elements for three-dimensional crack-propagation analysis. *International Journal for Numerical Methods in Engineering*, 44:1267–1282, 1999.

[38] R. Radovitzky and M. Ortiz. Error estimation and adaptive meshing in strongly nonlinear dynamic problems. *Computer Methods In Applied Mechanics And Engineering*, 172(1-4):203–240, 1999.

[39] M. Ortiz and L. Stainier. The variational formulation of viscoplastic constitutive updates. *Computer Methods In Applied Mechanics And Engineering*, 171(3-4):419–444, 1999.

[40] P.G. Sanders, J.A. Eastman and J.R. Weertman. Elastic and tensile behavior of nanocrystalline copper and palladium. *Acta Metallurgica*, 45:4019–4025, 1997.

[41] P.G. Sanders, C.J. Youngdhal and J.R. Weertman. The strength of nanocrystalline metals with and without flaws. *Materials Science and Engineering A*, 234-236:77–82, 1997.

[42] H. S. Kim, Y. Estrin, and M. B Bush. Plastic deformation behaviour of fine-grained materials. *Acta Materialia*, 48:493–504, 2000.

[43] B. Jiang and G.J. Weng. A composite model for the grain-size dependence of yield stress of nanograins materials. *Metallurgical and Materials Transactions A*, 34A:765–772, 2003.

[44] A.S. Argon and S. Yip. The strongest size. *Philosophical Magazine Letters*, 86(11):713–720, 2006.

[45] J. E. Marsden and T. J. R. Hughes. *Mathematical foundations of elasticity.* Prentice-Hall, Englewood Cliffs, N.J., 1983.

[46] M. Ortiz and A. Pandolfi. A variational Cam-clay theory of plasticity. *Computer Methods in Applied Mechanics and Engineering*, 193:2645–2666, 2004.

[47] K. Weinberg, A. Mota and M. Ortiz. A variational constitutive model for porous metal plasticity. *Computational Mechanics*, 37:142–152, 2006.

[48] E. Fancello, J.-Ph. Ponthot and L. Stainier. A variational formulation of constitutive models and updates in non-linear finite viscoelasticity. *International Journal for Numerical Methods in Engineering*, 65:1831–1864, 2006.

[49] Q. Yang, L. Stainier, and M. Ortiz. A variational formulation of the coupled thermo-mechanical boundary-value problem for general dissipative solids. *Journal of the Mechanics and Physics of Solids*, 54:401–424, 2006.

[50] J. Lubliner. On the thermodynamic foundations of non-linear solid mechanics. *International Journal of Non-Linear Mechanics*, 7:237–254, 1972.

[51] J. Lubliner. On the structure of the rate equations of materials with internal variables. *Acta Mechanica*, 17:109–119, 1973.

[52] F. Barbe, L. Decker, D. Jeulin and G. Cailletaud. Intergranular and intragranular behavior of polycrystalline aggregates. part 1: F.e. model. *International Journal of Plasticity*, 17:513–536, 2001.

[53] P. Heino and E. Ristolainen. Strength of nanoscale polycristalline copper under shear. *Philosophical Magazine A*, 81(4):957–970, 2001.

[54] S. Takeuchi. The mechanism of the inverse hall-petch relation of nanocrystals. *Scripta Materialia*, 44:1483–1487, 2001.

[55] C.J. Youngdhal, P.G. Sanders, J.A. Eastman and J.R. Weertman. Compressive yield strengths of nanocrystalline cu and pd. *Acta Metallurgica*, 37, 6:809–813, 1997.

[56] G. Lu and N. Kioussis. Interaction of vacancies with a grain boundary in aluminum: a first-principles study. *Physical Review B*, 64(024101):1–7, 2001.

[57] G.J. Fan, H. Choo, P.K. Liaw and E.J. Lavernia. Plastic deformation and fracture of ultrafine-grained al-mg alloys with a bimodal grain size distribution. *Acta Materialia*, 54:1759–1766, 2006.

[58] Y.M. Wang, E.M. Bringa, J.M. McNaney, M. Victoria, A. Caro, A.M. Hodge, R. Smith, B. Torralva, B.A. Remington, C.A. Schuh, H. Jamarkani and M.A. Meyers. Deforming nanocrystalline nickel at ultrahigh strain rates. *Applied Physics Letters*, 88(061917):1–3, 2006.

[59] A.C. Lund, T.G. Nieh and C.A. Schuh. Tension/compression strength asymmetry in a simulated nanocrystalline metal. *Physical Review B*, 69:012101, 2004.

[60] C.A. Schuh and A.C. Lund. Atomistic basis for the plastic yield criterion of metallic glass. *Nature Materials*, 2:449–452, 2003.

[61] A.C. Lund and C.A. Schuh. Yield surface of a simulated metallic glass. *Acta Materialia*, 51:5399–5411, 2003.

[62] A.C. Lund and C.A. Schuh. The mohr-coulomb criterion from unit shear processes in metallic glass. *Intermetallics*, 12:1159–1165, 2004.

[63] Ya. B. Zel'dovich and Yu. P. Raizer. *Physics of shock waves and high-temperature hydrodynamic phenomena*, volume 2. Academic press, New York and London, 1967.

[64] Marc A. Meyers. *Dynamic behavior of materials.* Wiley. Interscience, 1994.

[65] D.S. Drumheller. *Introduction to wave propagation in nonlinear fluids and solids.* Cambridge University Press, 1998.

[66] J.N. Johnson. Single-particle model of a solid: the mie-grüneisein equation. *American Journal of Physics*, 36(10):917–919, 1968.

[67] Z. Zhao, R. Radovitzky, and A. Cuitino. A study of surface roughening in f.c.c. metals using direct numerical simulation. *Acta Materialia*, 52(20):5791–5804, 2004.

[68] E. Yu Tonkov and E.G. Pontyatovsky. *Phase transformations of elements under high pressure.* CRC Press, Advances in metallic alloys, 2005.

[69] R.J. Clifton. On the analysis of elastic/visco-plastic waves of finite uniaxial strain. In John J. Burke and Volker Weiss, editor, *Shock waves and the mechanical properties of solids*, volume Proceedings of the 17th Sagamore Army Material Research Conference, pages 73–119. Syracuse university press, 1971.

[70] A. Molinari and G. Ravichandran. Fundamental structure of steady plastic shock waves in metals. *Journal of Applied Physics*, 95(4):1718–1732, 2004.

[71] J. VonNeumann and R.D. Richtmyer. A method for the numerical calculation of hydrodynamic shocks. *Journal of Applied Physics*, 21:232–237, 1950.

[72] A. Lew, R. Radovitzky and M. Ortiz. An artificial-viscosity method for the lagrangian analysis of shocks in solids with strength on unstructured, arbitrary-order tetrahedral meshes. *Journal of Computer-Aided Materials Design*, 8:213–231, 2001.

[73] Y.F. Shen, L. Lu, M. Dao and S. Suresh. Strain rate sensitivity of Cu with nanoscale twins. *Scripta Materialia*, 55:319–322, 2006.

[74] A. Frøseth, H. Van Swygenhoven and P.M. Derlet. The influence of twins on the mechanical properties of nc-al. *Acta Materialia*, 52:2259–2268, 2004.

[75] A.G. Frøseth, P.M. Derlet and H. Van Swygenhoven. Grown-in twin boundaries affecting deformation mechanisms in nc-metals. *Applied Physics Letters*, 85(24):5863–5865, 2004.

[76] A.G. Frøseth, P.M. Derlet and H. Van Swygenhoven. Twinning in nanocrystalline fcc metals. *Advanced Engineering Materials*, 7(1-2):16–20, 2005.

[77] A.G. Frøseth, P.M. Derlet and H. Van Swygenhoven. Vicinal twin boundaries providing dislocation sources in nanocrystalline al. *Scripta Materialia*, 54:477–481, 2006.

[78] A.M. Cuitiño and M. Ortiz. Computational modeling of single crystals. *Modeling and Simulation in Materials Science and Engineering*, 1:255–263, 1992.

[79] S.N. Kuchnicki, A.M. Cuitiño and R.A. Radovitzky. Efficient and robust constitutive integrators for single-crystal plasticity modeling. *International Journal of Plasticity*, 22:1988–2011, 2006.

[80] E.H. Lee. Elastic-plastic deformation at finite strains. *Journal of Applied Mechanics*, 36:1, 1969.

[81] C. Teodosiu. A dynamic theory of dislocations and its applications to the theory of the elastic-plastic continuum. In J. A. Simmons, editor, *Conf. Fundamental Aspects of Dislocation Theory*, volume 2, page 837, Washington, 1969. Natl. Bureau of Standards Special Publication.

[82] R.J. Asaro and J.R. Rice. Strain localization in ductile single crystals. *Journal of the Mechanics and Physics of Solids*, 25:309, 1977.

[83] K.S. Havner. On the mechanics of crystalline solids. *Journal of the Mechanics and Physics of Solids*, 21:383, 1973.

[84] R. Hill and J.R. Rice. Constitutive analysis of elastic-plastic crystals at arbitary strains. *Journal of the Mechanics and Physics of Solids*, 20:401, 1972.

[85] J. Mandel. Plasticité classique et viscoplasticité. Technical report, Lecture Notes, Int. Centre for Mech. Sci., Udine, Berlin:Springer, 1972.

[86] J.R. Rice. Inelastic constitutive relations for solids: an internal-variable theory and its applications to metal plasticity. *Journal of the Mechanics and Physics of Solids*, 19:433, 1971.

[87] C. Teodosiu. *Elastic Models of Crystal Defects.* Springer-Verlag, New York, 1982.

[88] G.I. Taylor. Plastic strain in metals. *Journal of the Institute of Metals*, 62:307–324, 1938.

[89] P. Franciosi and A. Zaoui. Multislip in fcc crystals: A theoretical approach compared with experimental data. *Acta Metallurgica*, 30:1627–1637, 1982.

[90] P. Franciosi and A. Zaoui. Glide mechanisms in bcc crystals: an investigation of the case of α-iron through multislip and latent hardening tests. *Acta Metallurgica*, 31:1331–1342, 1983.

[91] P. Franciosi. The concepts of latent hardening and strain hardening in metallic single crystals. *Acta Metallurgica*, 33:1601–1612, 1985.

[92] P. Franciosi. Fcc single crystals hardening: anisotropy and stacking fault energy. In *ICSMA Symp.*, page 281, Montreal, Canada, 1985.

[93] P. Franciosi. On flow and work hardening expression correlations in metallic single crystal plasticity. *Revue De Physique Appliquée*, 23:383–394, 1988.

[94] K.S. Cheong, E.P. Busso and A. Arsenlis. A study of microstructural length scale effects on the behaviour of fcc polycrystals using strain gradient concepts. *International Journal of Plasticity*, Article In Press, 2004.

[95] A.S. Abou-Sayed and R.J. Clifton. Pressure shear waves in fused silica. *Journal of Applied Physics*, 47(5):1762–1770, 1976.

[96] D.C. Wallace. Equation of state from weak shocks in solids. *Physical Review B*, 22(4):1495–1502, 1980.

[97] D.C. Wallace. Flow process of weak shocks in solids. *Physical Review B*, 22(4):1487–1494, 1980.

[98] G. Meir and R.J. Clifton. Effects of dislocation generation at surfaces and subgrain boundaries on precursor decay in high-purity LiF. *Journal of Applied Physics*, 59(1):124–148, 1986.

[99] D.L. Tonks. Rate-dependent plasticity of copper and stainless steel under shock compression. *Journal of Applied Physics*, 66(5):1951–1960, 1989.

[100] D.L. Tonks. Model for the relation between shock velocity and particle velocity in weak shock waves in metals. *Journal of Applied Physics*, 70(8):4238–4247, 1991.

[101] J.B. Aidun and F.L. Addessio. An enhanced cell model with nonlinear elasticity. *Journal of Composite Materials*, 30:248–280, 1996.

[102] K. Brugger. Thermodynamic definition of higher order elastic coefficients. *Physical Review A*, 133:1611–1612, 1964.

[103] Z.-P. Chang. Third-order elastic constants of NaCl and KCl single crystals. *Physical Review A*, 140:1788–1799, 1965.

[104] W. B. Gauster and M. A. Breazeale. Ultrasonic measurement of the nonlinearity parameters of copper single crystals. *Physical Review*, 168:655–661, 1968.

[105] W.C. Overton, Jr. and J. Gaffney. Temperature variation of the elastic constants of cubic elements. I. Copper. *Physical Review*, 98:969–977, 1955.

[106] Y. Hiki and A.V. Granato. Anharmonicity in noble metals; higher order elastic constants. *Physical Review*, 144:411–419, 1966.

[107] A. Cezairliyan. *Specific heat of solids.* Hemisphere Publishing Corporation, 1988.

[108] F.C. Nix and D. MacNair. The thermal expansion of pure metals: copper, gold, aluminum, nickel, and iron. *Physical Review*, 60:597–605, 1941.